

Synthesis and Characterization of $\text{Fe}_2\text{O}_3@ \gamma\text{-Al}_2\text{O}_3$ Nanoparticles for Electrochemical Applications



A dissertation submitted to the Department of Chemistry,
Quaid-i-Azam University, Islamabad, in partial fulfillment

of the requirements for the degree of

Master of Philosophy

in

Physical Chemistry

by

Sumiya Arif

Department of Chemistry

Quaid-i-Azam University

Islamabad

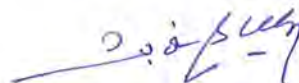
2023

بِسْمِ اللَّهِ الرَّحْمَنِ الرَّحِيمِ

DECLARATION

This is to certify that this dissertation entitled “**Synthesis and Characterization of $\text{Fe}_2\text{O}_3@ \text{r-Al}_2\text{O}_3$ Nanoparticles for Electrochemical Application**” submitted by **Ms. Sumiya Arif**, is accepted in its present form by the Department of Chemistry, Quaid-i-Azam University, Islamabad, as satisfying the dissertation requirements for the degree of **Master of Philosophy in Physical Chemistry**.

External Examiner:



Dr. Mrs. Shabana Waseem (PoP)
Chief Scientist (Retd.) Applied Chemistry
Laboratories (PAEC) P.O. Nilore
Islamabad

Supervisor:



Prof. Dr. Mrs. Naveed Kausar Janjua
Department of Chemistry
Quaid-i-Azam University
Islamabad

Head of Section:



Prof. Dr. Hazrat Hussain
Department of Chemistry
Quaid-i-Azam University
Islamabad

Chairman:



Prof. Dr. Aamer Saeed Bhatti
Department of Chemistry
Quaid-i-Azam University
Islamabad



*Dedicated to My
parents and my
husband*

Acknowledgments

All praises and glory to **Allah Almighty**, the most beneficent and merciful Who bestowed me with enough courage and endurance to accomplish this work. Peace, blessings, and salutations upon His last prophet **Hazrat Muhammad (P.B.U.H)**, who guided us to the perfect code of life.

It gives me pleasure to express deep gratitude to my supervisor **Prof. Dr. Mrs. Naveed Kausar Janjua** – an expert in electroanalytical techniques and methods for her tremendous support during my M.Phil. study and research. I am very grateful to Dr. Naveed for her skillful guidance, important suggestions, sound advice, and valuable discussions throughout my research work. She was always available and willing to help me with all kinds of questions and concerns I had.

I pay my paramount respect and gratitude to the Head of the Physical section, **Prof. Dr. Hazrat Hussain**, and the Chairman Department of Chemistry, **Prof. Dr. Aamer Saeed**, for providing all the necessary facilities for conducting this research. I am also grateful to the staff of XRD and FTIR lab, and **Dr. Yasir (ISTP)** for his kind help in SEM and EDX.

I am highly thankful to my lab mate's fellow and friends for their absolute guidance, great times, and the memories we spent together. Special thanks to **Dr. Tehmeena Maryum Butt** and **Hira Khalid** for their support and affection during the entire work means a lot to me.

I owe my deepest gratitude to my parents (**Malik M. Arif and Tahzeem Akhtar**), brother (**Malik Usman Arif**), and my husband (**Malik M. Mubeen**) for their constant support, prayers, motivation, and unconditional love. They always infused me throughout my academic career and enabled me to complete this tedious task.

Sumiya Arif

List of Contents

	Page No.
List of Figures.....	x
List of Tables.....	xv
List of Symbols and Abbreviations.....	xvi
Abstract.....	xviii
Chapter 1.....	1
Introduction.....	1
1.1 Nanotechnology.....	1
1.1.1 Nanomaterials and their properties.....	1
1.2 Catalysis.....	2
1.2.1 Homogeneous catalysis.....	2
1.2.2 Heterogeneous catalysis.....	3
1.3 Electrocatalysis.....	3
1.4 Choice of Materials in Electrocatalysis.....	4
1.5 Synthesis Methods.....	5
1.5.1 Basics of precipitation method.....	5
<i>i. Choice of base hydroxide.....</i>	<i>5</i>
<i>ii. Choice of metal salts.....</i>	<i>6</i>
<i>iii. Choice of pH.....</i>	<i>6</i>
1.5.2 Basic of impregnation method.....	6
1.6 Use of Support.....	7
1.6.1 Metal oxide as support materials.....	7
1.6.2 Alumina as electrocatalyst support.....	8
<i>a. α - alumina.....</i>	<i>8</i>

b. θ - alumina	8
c. γ - alumina	9
1.7 Transition Metal Oxides as Active Materials	9
1.7.1 Iron oxide as an active component.....	10
1.7.1.1 Phases of iron oxide (Fe_2O_3)	10
1.7.2 Applications of iron oxide.....	10
1.8 World Energy Crises and Renewable Energy Resources	10
1.9 Water: An Ultimate Source of Hydrogen and Oxygen.....	11
1.9.1 Hydrogen evolution reaction (HER)	13
1.9.2 Oxygen evolution reaction (OER).....	13
1.10 Characterization Techniques.....	15
1.10.1 X-ray diffraction (XRD).....	15
1.10.1.1 Basic principle of X-ray diffraction (XRD) technique	15
1.10.1.2 Calculations for crystallite size	17
1.10.1.3 XRD's advantages.....	17
1.10.2 Fourier transform infrared spectroscopy (FT-IR)	17
1.10.2.1 Working principle	18
1.10.2.2 Instrumentation.....	18
1.10.2.3 Advantages of FT-IR	19
1.10.3 Scanning electron microscopy (SEM).....	19
1.10.3.1 Principle of SEM analysis.....	19
1.10.3.2 Applications of scanning electron microscopy (SEM)	20
1.10.4 Energy dispersive X-rays spectroscopy (EDS).....	20
1.10.4.1 Basic principle of EDX	21
1.10.5 Cyclic voltammetry (CV).....	21

1.10.5.1	<i>Categorization of redox processes</i>	22
1.10.6	Linear sweep voltammetry (LSV).....	24
1.10.7	Electrochemical impedance spectroscopy (EIS).....	25
1.10.7.1	<i>Basic principle</i>	25
1.10.7.2	<i>Data representation</i>	26
1.10.7.3	<i>Data analysis</i>	27
1.10.7.4	<i>Equivalent circuit model</i>	27
1.10.8	Chronoamperometry.....	27
1.11	Aims and Objectives	27
1.12	Plan of work.....	28
1.13	Thesis Layout.....	28
Chapter 2	29
Experimental	29
2.1	Chemicals and Reagents	29
2.2	Synthesis of pure aluminum oxide ($\gamma\text{-Al}_2\text{O}_3$)	30
2.3	Synthesis of impregnated catalysts ($\text{Fe}_2\text{O}_3@ \text{Al}_2\text{O}_3$).....	31
2.4	Electrode Modification	33
2.4.1	Procedure for electrode modification.....	33
2.5.1	X-ray diffraction (XRD) measurements.....	34
2.5.2	FT-IR instrumentation.....	35
2.5.3	Scanning electron microscopy (SEM).....	35
2.5.4	Gamry Potentiostat/ Galvanostat.....	35
Chapter 3	37
Results and Discussion	37
3.1	Physical Characterization.....	37

3.1.1	X-ray diffraction analysis (XRD).....	37
3.1.2	FT-IR analysis.....	39
3.1.3	Scanning electron microscopy (SEM).....	40
3.2	Electrochemical Characterization	44
3.2.1	Estimation of active surface for modified electrodes.....	44
3.2.2	Electrochemical impedance spectroscopy (EIS).....	46
3.2.2.1	<i>Simulation of Nyquist plot by fitting to the equivalent circuit model</i>	48
3.3	Catalyst Performance for OER in Alkaline Medium.....	49
3.3.1	Cyclic voltammetry (CV) and linear sweep voltammetry (LSV).....	50
3.3.1.1	<i>Determination of current densities (J)</i>	50
3.3.1.2	<i>Determination of onset potential (E_{onset}) and overpotential (η)</i>	54
3.3.1.3	<i>Determination of diffusion and mass transport coefficients</i>	57
3.3.1.4	<i>Kinetics of OER process and estimation of heterogeneous rate constants</i>	61
3.3.2	Double layer capacitance and ECSA	65
3.3.3	Tafel slopes	69
3.3.4	EIS and charge transfer resistance	71
3.3.5	Chronoamperometry.....	76
	Conclusions.....	79
	References.....	81
	Appendix I.....	88

List of Figures

	Page No.
Figure 1.1. Illustration of an eco-friendly energy landscape through electrocatalysis [11].	4
Figure 1.2. Cubic crystalline form of Al ₂ O ₃ [17].	9
Figure 1.3. Different energy sources for water splitting [20].	12
Figure 1.4. General representation of water splitting.	12
Figure 1.5. Proposed OER mechanism in alkaline medium [28].	14
Figure 1.6. Bragg's diffraction.	16
Figure 1.7. Schematic diagram of the diffractometer configuration [38].	16
Figure 1.8. FTIR spectrometer instrumentation [42].	18
Figure 1.9. Basic components of SEM setup [44].	19
Figure 1.10. Working principle of EDS [44].	21
Figure 1.11. (a) An excitation signal of CV/LSV, (b) A typical cyclic voltammogram representing anodic and cathodic peaks for a single reversible electron transfer process [48].	22
Figure 1.12. Cyclic voltammograms for (a) reversible, (b) quasi-reversible, and (c) irreversible process [49].	24
Figure 1.13. LSV potential sweep with time [50].	25
Figure 1.14. Nyquist and Bode plots for representation of EIS spectra [53].	26
Figure 2.1. Schematic representation of the synthesis of γ -alumina.	31
Figure 2.2. Scheme for the synthesis of Fe ₂ O ₃ @ γ -Al ₂ O ₃ .	32

Figure 2.3. Electrode polishing (a) Drop cast method for preparation of working electrode (b).....	34
Figure 2.4. Electrochemical cell assembly.	36
Figure 3.1. XRD pattern of γ -Al ₂ O ₃ (a), and reference pattern of γ -Al ₂ O ₃ (b).....	37
Figure 3.2. XRD patterns for (a) AlFe-1, (b) AlFe-2, (c) AlFe-3, (d) AlFe-4, (e) AlFe-5, and (f) AlFe-10.	38
Figure 3.3. (a) FT-IR spectra of Al ₂ O ₃ , Al-Fe-1, Al-Fe-2, AlFe-3, AlFe-4, AlFe-5, and AlFe-10, (b) IR region highlighting Fe-O and Al-O absorption peaks.	40
Figure 3.4. SEM micrographs of Al ₂ O ₃ (a) at 1 μ m, (b) at 10 μ m, and (c) EDX spectrum of Al ₂ O ₃	41
Figure 3.5. SEM micrographs at different resolutions for (a) AlFe-1, (b) AlFe-2, (c) AlFe-3, (d) AlFe-4, and (e) AlFe-5.	42
Figure 3.6. EDX spectra for (a) AlFe-1, (b) AlFe-2, (c) AlFe-3, (d) AlFe-4, (e) AlFe-5, and (f) AlFe-10.	43
Figure 3.7. Cyclic voltammetry response of all modified electrodes for Fe ²⁺ /Fe ³⁺ redox system in 5 Mm K ₄ [Fe(CN) ₆] and 1 M KCl, (b) Graphical representation of comparative active surface areas of all modified electrodes.	45
Figure 3.8. (a) EIS spectra of all compositions performed in 5 mM K ₃ [Fe(CN) ₆] and 1 M KCl solution, (b) The model fitted EIS spectra for water oxidation along its equivalent circuit model used for simulation of EIS data.	47
Figure 3.9. Diagram of an equivalent circuit used for fitting impedance spectroscopic data [53]......	48

Figure 3.10. CV responses of Al ₂ O ₃ in (a) 1 M KOH, (b) 1 M KOH + 1 M MeOH at 100 mV s ⁻¹	50
Figure 3.11. Comparative CV responses of OER in 1 M KOH and 1 M KOH + 1 M MeOH at 100 mV s ⁻¹	51
Figure 3.12. CV responses for all modified electrodes in 1 M KOH at 100 mV s ⁻¹	52
Figure 3.13. CV responses for all modified electrodes in 1 M KOH + 1 M MeOH at 100 mV s ⁻¹	52
Figure 3.14. Comparison of current densities of all modified electrodes in 1 M KOH and 1M KOH + 1 M MeOH.	53
Figure 3.15. Diagrammatic representation of methanol and water oxidation processes at the electrode surface.	54
Figure 3.16. LSV curves for the OER response of Al ₂ O ₃ in 1 M KOH and 1 M KOH + 1 M MeOH at 100 mV s ⁻¹	55
Figure 3.17. LSV scans for OER at (a) AlFe-1, (b) AlFe-2, (c) AlFe-3, (d) AlFe-4, (e) AlFe-5, and (f) AlFe-10.	56
Figure 3.18. CV profiles for the OER process were observed at Al ₂ O ₃ /GC at different scan rates.	57
Figure 3.19. Linear functional plot for the determination of diffusion coefficient of OER at Al ₂ O ₃ /GCE.....	58
Figure 3.20. CV scans for OER at different scan rates observed for (a) AlFe-1/GC, (b) AlFe-2/GC, (c) AlFe-3/GC, (d) AlFe-4/GC, (e) AlFe-5/GC, and (f) AlFe-10/GC electrodes.	59

Figure 3.21. Linear functional plots for the determination of diffusion coefficients for OER at (a) AlFe-1/GC, (b) AlFe-2/GC, (c) AlFe-3/GC, (d) AlFe-4/GC, (e) AlFe-5/GC, and (f) AlFe-10/GC electrodes.	60
Figure 3.22. CV profiles for the OER process were observed at Al ₂ O ₃ /GC in different methanol concentrations.	61
Figure 3.23. Linear functional plot for the determination of the heterogeneous rate constant of OER at Al ₂ O ₃ /GCE.....	62
Figure 3.24. CV scans for OER in different methanol concentration for (a) AlFe-1/GC, (b) AlFe-2/GC, (c) AlFe-3/GC, (d) AlFe-4/GC, (e) AlFe-5/GC, and (f) AlFe-10/GC electrodes.	63
Figure 3.25. Linear functional plots for the determination of heterogeneous rate constants for OER at (a) AlFe-1/GC, (b) AlFe-2/GC, (c) AlFe-3/GC, (d) AlFe-4/GC, (e) AlFe-5/GC, and (f) AlFe-10/GC electrodes.....	64
Figure 3.26. Bar chart for the comparison of different kinetic parameters of the OER process at all modified electrodes.	65
Figure 3.27. (a) CV responses of Al ₂ O ₃ /GC in non-Faradic region, (b) Plot of difference of current vs scan rate for the calculation of C _{dl} value for Al ₂ O ₃	66
Figure 3.28. CV responses in non-Faradic region at different scan rates for (a) AlFe-1, (b) AlFe-2, (c) AlFe-3, (d) AlFe-4, (e) AlFe-5, and (f) AlFe-10.....	67
Figure 3.29. Linear functional plots for the calculation of C _{dl} for (a) AlFe-1, (b) AlFe-2, (c) AlFe-3, (d) AlFe-4, (e) AlFe-5, and (f) AlFe-10.....	68
Figure 3.30. Tafel slopes for all compositions in 1 M KOH.	70
Figure 3.31. Tafel slopes for all compositions in 1 M KOH + 1 M methanol.....	70

Figure 3.32. The model fitted EIS spectra of Al ₂ O ₃ /GC for water oxidation in 1 M KOH, along its equivalent circuit model used for simulation of EIS data.	72
Figure 3.33. The model fitted EIS spectra of Al ₂ O ₃ /GC for water oxidation in 1 M KOH + 1 M MeOH, along its equivalent circuit model used for simulation of EIS data.	73
Figure 3.34. Comparison of Nyquist plots in 1 M KOH and 1 M KOH + 1 M methanol for OER at (a) AlFe-1, (b) AlFe-2, (c) AlFe-3, (d) AlFe-4, (e) AlFe-5, and (f) AlFe-10.	74
Figure 3.35. Comparison of R _{ct} values in 1 M KOH and 1 M KOH + 1 M MeOH for all compositions.	75
Fig. 3.36. Chronoamperometric stability test performed for AlFe-4/GC electrode in 1 M KOH and 1 M KOH + 1 M MeOH.	76
Figure 3.37. LSV Curves before and after chronoamperometric test for AlFe-4/GC in (a) 1 M KOH and (b) 1 M KOH + 1 M MeOH.	77
Figure 3.38. Chronoamperometry performed for all compositions in 1 M KOH.	77
Figure 3.39. Chronoamperometry performed for all compositions in 1 M KOH + 1 M MeOH.	78

List of Tables

	Page No.
Table 2.1. Chemicals used in the synthesis of compositions and in electrochemical preparations.....	29
Table 2.2. Sample codes and molecular formulae for the synthesis compositions.....	33
Table 3.1. Average crystallite sizes of synthesized materials.....	39
Table 3.2. Elemental weight% from EDX analysis.	44
Table 3.3. Peak current values and active surface area of modified electrodes.....	46
Table 3.4. Derived data from the equivalent circuit of fitted EIS models in $K_3[Fe(CN)_6]$	49
Table 3.5. Current densities of all modified electrodes from CV data.	53
Table 3.6. Estimated onset and overpotential values for all modified electrodes.....	57
Table 3.7. Estimated kinetics parameters for water oxidation of all synthesized samples.	65
Table 3.8. OER parameters (C_{dl} , ECSA, and RF) for all compositions.....	69
Table 3.9. Estimated Tafel slopes for all catalysts in 1 M KOH and 1 M KOH + 1 M MeOH.	71
Table 3.10. EIS parameters extracted from simulated EIS data.	75

List of Symbols and Abbreviations

Terms	Description
A	Area of electrode
b	Tafel slope
C	Concentration
C_{dl}	Doble layer capacitance
CPE	Constant phase element
CV	Cyclic voltammetry
D₀	Diffusion coefficient
DRS	Diffuse reflectance spectroscopy
E	Applied potential
E_a	Activation energy
EC	Electrochemical
ECSA	Electrochemically active surface area
EDX	Energy dispersive x-ray spectroscopy
EIS	Electrochemically impedance spectroscopy
FC	Fuel cell
GC	Glassy carbon
GCE	Glassy carbon electrode
HER	Hydrogen evolution reaction
I_p	Peak current
J	Current density

J_0	Exchange current density
K_0	Heterogeneous rate constant
MeOH	Methanol
m_f	Mass transport coefficient
η	Overpotential
OER	Oxygen evolution reaction
ORR	Oxygen reduction reaction
SEM	Scanning electron microscopy
R_{ct}	Charge transfer resistance
R_s	Solution resistance
R	Universal gas constant
T	Temperature
TGA	Thermogravimetric analysis
WOR	Water oxidation reaction
XRD	X-ray diffraction
Z_{real}	Real component of impedance
Z_{imag}	Imaginary component of impedance

Abstract

In the present research work, an attempt was made to synthesize electroactive nanocrystalline material for catalyzing oxygen evolution reaction (OER) in alkaline media (1 M KOH). γ -alumina was selected as catalytic support and synthesized using the precipitation method with different wt.% compositions of Fe_2O_3 loading as active component. The loading was done by means of the impregnation method and 1, 2,3,4,5, and 10% of $\text{Fe}_2\text{O}_3@Al_2O_3$ nanocomposites were synthesized. The phase, morphology, and elemental compositions were studied using XRD, FT-IR, SEM, and EDX, while OER studies for all synthesized materials were carried out using different voltametric techniques such as CV; cyclic voltammetry and LSV: linear sweep voltammetry, chronoamperometry and EIS; electrochemical impedance spectroscopy. OER performance of the catalyst in terms of onset potential (E_{onset}), overpotential (η), current density (J), charge transfer resistance (R_{ct}), and Tafel slopes (b), was calculated. All electrochemical measurements were carried out in three-electrode cell configurations, with subsequent addition of methanol in 1 M KOH electrolyte utilizing catalyst-modified glassy carbon as working electrode while Ag/AgCl as reference and platinum wire as a counter electrode. Although all the compositions showed good electrocatalytic activity for OER, however, AlFe-4 (4% $\text{Fe}_2\text{O}_3@Al_2O_3$) displayed the best performance with low onset potential (1.61 V), lowest overpotential (0.54 V), and the high current density of 74.28 mA cm^{-2} at 100 mVs^{-1} among all the compositions. Highest value of diffusion coefficient ($11.4 \times 10^{-8} \text{ cm}^2 \text{ s}^{-1}$) and heterogeneous rate constant ($7.0 \times 10^{-4} \text{ cm s}^{-1}$) were also observed for AlFe-4 (4% $\text{Fe}_2\text{O}_3@Al_2O_3$). This study scheme was proved to be useful for the catalyst synthesis due to minimum use of noble metal active component and replacement with cheaper and effective non noble metal oxide providing better results for activity and stability for water oxidation at ambient conditions.

Chapter 1

Introduction

The rapid expansion of certain industries and the upward trend in the global population in recent times have acted as major drivers behind the ongoing global energy crises and environmental pollution. Hence, in order to safeguard the long-term and sustainable progression of human society, it becomes imperative to foster the creation of such technologies that can effectively harness renewable energy resources and facilitate environmental remediation [1]. Scientists are actively pursuing technological solutions to address these challenges, with nanotechnology standing out as notable advancement. Shifting from bulk materials to nanoscale substances triggers transformative changes in the properties of these materials (nanomaterials). In the domain of renewable energy resources, hydrogen holds a pivotal role attributed to its high reactivity, potent chemical energy, renewability, and their environmental friendliness [2].

1.1 Nanotechnology

Nanotechnology represents a broad realm in modern science and engineering, with the potential to yield boundless opportunities. Nanotechnology was primarily commenced by Norio Taniguchi, in 1974 as follows: “Nanotechnology involves the process of partition, solidification, and distortion of materials at the atomic or molecular scale”.

Exploring new nanostructured materials lies at the core of nanotechnology and nano science, often referred to as “revolutionary nano”. These materials show some extraordinary properties as compared to their bulk counterpart. “*Chemistry is an ultimate nanotechnology*” and chemist are focused on the development of new nanomaterials by using nanotechnology. Some examples of chemical industry developments are such as the formation of Buckyballs and bucky tubes, quantum dots, phase-separated polymers, self-assembled monolayers, Nano biomedicines, etc [3]. Nanotechnology is focused on the production, characterizations, and applications of nanomaterials.

1.1.1 Nanomaterials and their properties

Nanomaterials encompass substances with at least one dimension measuring less than about 100 nanometers. Nano is the Greek word meaning (dwarf). Nanotechnology enables

us to manufacture, see measure and manipulate these small-sized particles [4]. Nanomaterials exhibit distinctive electrical, magnetic, optical, and catalytic characteristics because of their extensive surface area, robust mechanical properties, efficient heat conduction, remarkable stability, and hardness [5]. Introducing specific types of impurities can alter the energy band gap and density of charge carriers in nanoparticles, resulting in changes to their optical and electronic properties. Additionally, adjustments in synthesis temperature can introduce structural defects [6].

1.2 Catalysis

Catalysts are compounds capable of accelerating the pace of a chemical reaction, often without undergoing depletion in the process. The phenomenon where a catalyst is employed to amplify the speed of a chemical reaction is referred to as catalysis. Catalysis has played a vital role in physical and biological sciences. Nowadays it is increasingly used as an environmental catalyst to suppress atmospheric pollution. More than 90% of chemical manufacturing in the whole world used catalysts in one or another form. There are a variety of products like polymers, fibers, medicines, paints, fuels, and many others that cannot be synthesized without using a catalyst. Thus, catalysis makes possible the formation of such products which are essential for human life. Nano-catalysts, tailored on the nanoscale, possess unique properties, including high surface area, enhanced reactivity, size and shape control, improved dispersion, tunable surface chemistry, reduce mass transport limitations, stability, and environmental friendliness which make them suitable for chemical reaction [7]. Some catalysts are specific for a chemical reaction like enzyme catalysis.

According to the characteristics and physical state of the substance used in the chemical reaction, the process of catalysis is classified into two distinct types:

1.2.1 Homogeneous catalysis

Homo means identical; in this type of catalysis, both reactant and catalyst are in the same physical state either gas or liquid phase. There are many advantages related to this process such as better yield, high selectivity, and availability of all active sites due to solubility in the reaction medium. As compared to heterogeneous catalysis; the homogeneous catalyst is simple and doesn't involve a lack of mechanistic understanding of multiphase processes. However, the major challenge for manufacturers by using this catalysis is to detach the

catalyst from the final product because separation of catalyst is very necessary in many areas, especially in the pharmaceutical industry. Various techniques like chromatography extraction and distillation can be used but still, there is an issue with the removal of trace impurities. To solve this problem, scientists are working on the development of heterogeneous catalysis [8].

1.2.2 Heterogeneous catalysis

This type of catalysis, is immobilized on a porous support, allowing for convenient separation from the product [9]. However, these solid catalysts have many disadvantages only surface-active sites are accessible for catalysis, which can hamper the overall effectiveness of catalyst and extracting the catalyst from the solid support can pose challenges in some instances.

Depending upon the nature of chemical reaction, catalysis encompasses various types like acid-base catalysis, electrocatalysis, photocatalysis, and enzyme catalysis etc. Electrocatalysis is briefly discussed in the coming paragraph.

1.3 Electrocatalysis

Electrocatalysis is a special branch of heterogeneous catalysis in which electrochemical reactions involve a direct transfer process between the reacting species, known as a redox reaction. This redox (reduction and oxidation) processes occur at separate electrodes, namely the cathode and anode, connected externally by a circuit and internally via an electrolyte or salt bridge. When a redox process occurs spontaneously, the chemical energy is converted to electrical energy, generating electricity. Conversely, in nonspontaneous electrochemical processes, electrical energy is converted into chemical energy which is known as electrolytic cells [10]. Electrocatalysis holds significant importance in advancing the production of environmentally friendly and sustainable energy solutions. Through various electrochemical processes, it enables the development of renewable energy resources by facilitating the electrochemical transformation of CO_2 and water, resulting in the production of hydrogen, hydrocarbon, and oxygen. Figure 1.1 represents the possible strategies for the electrochemical transformation of CO_2 , H_2O , and N into valuable products (hydrogen, hydrocarbon, oxygen, and ammonia), as earth is an ultimate source of these compounds.

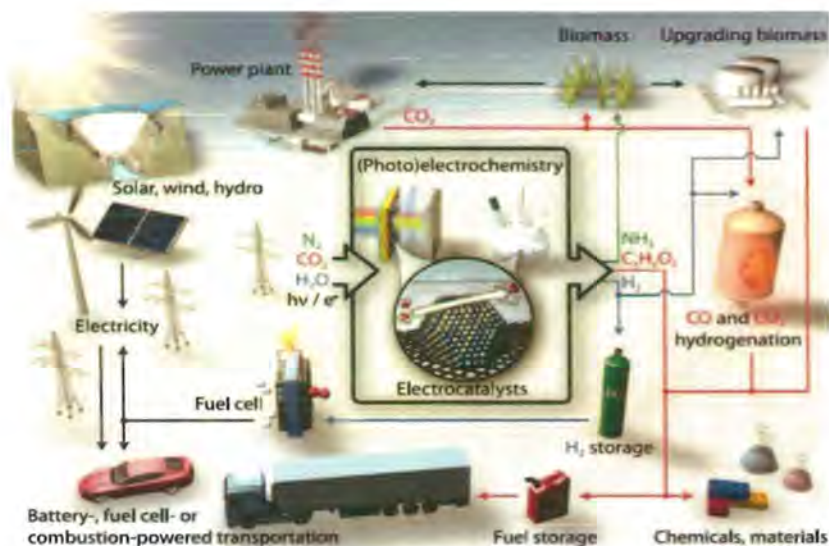


Figure 1.1. Illustration of an eco-friendly energy landscape through electrocatalysis [11].

Numerous electrochemical reactions are directly related to energy production and energy storage (battery and fuel cell). These reactions also involve oxygen evolution reaction (HER), hydrogen evolution reaction (HER), oxygen reduction reaction (ORR), and CO₂ reduction reaction (CO₂-RR). These reactions have potential importance however certain half reactions suffer from sluggish kinetics, necessitating large overpotential for efficient operation. So, there is a pressing need to develop an efficient and selective catalyst that effectively reduces this overpotential energy barrier. An electrocatalyst with enhanced catalytic properties can be used to lower the overpotential barrier to produce hydrogen and oxygen via electrochemical water splitting.

1.4 Choice of Materials in Electrocatalysis

Electrocatalysis demands catalyst materials that endure harsh conditions and maintain effectiveness over a prolonged duration. Catalyst degradation and deactivation are frequently notable in electrocatalysts due to existence of liquid medium, ions, and electric powered fields, leading to catalyst loss, deactivation, and poisoning. Consequently, the options are restricted to unique metal oxides, supported metal/alloys and inorganic substance like chalcogenides or carbides.

1.5 Synthesis Methods

Different methods have been employed to synthesize the nanoparticles some are given below.

- i. Sol-gel method
- ii. Chemical vapor deposition
- iii. Hydrothermal method
- iv. Combustion method Flame
- v. Laser ablation
- vi. Microemulsion method
- vii. Flame pyrolysis
- viii. Co-precipitation method
- ix. Sono-chemical method
- x. Precipitation method

1.5.1 Basics of precipitation method

This represents one of the simplest and most traditional chemical methods for synthesizing metal oxides, initially pioneered by Marcilly [12]. The process involves the dissolving a metal precursor, subsequently modulating the pH (typically within the range of 5 to 10) to facilitate the complete precipitation of metal hydroxide. The resulting hydroxide is then subjected to calcination to attain the desired metal oxide phase. Various factors play a critical role in the preparation of metal hydroxide using this method:

i. Choice of base hydroxide

The solution chemistry of the cation under consideration is essential to consider. For instance, aqueous ammonia is often the chosen precipitant due to its subsequent decomposition during drying and calcination, leading to the NH_3 and surface hydroxyl groups.

ii. Choice of metal salts

It is important to choose metal salts carefully when preparing a catalyst because the anion found in the metal salt solution have the potential to function as inhibitors of the catalyst. Metal nitrate salts were selected as precursors because to their advantageous breakdown kinetics [13]. Typically, nitrates anion that become adsorbed on the surface of the precipitates can easily undergo decomposition during the calcination step of the preparation. Consequently, nitrates do not impart any residual traces on the support surface.

iii. Choice of pH

Various cations undergo precipitation at distinct pH range. Accordingly, it becomes pivotal to determine an appropriate pH level for each cation type. This objective can be achieved by applying the solubility product principle to metal hydroxide precipitates. The formation of precipitates occurs solely when the concentrations of both the metal and hydroxide exceed the solubility product threshold. The concentration of metal ions remains relatively stable within the solution, it is the concentration of hydroxyl ions that predominantly govern the regulation of precipitate formation. Consequently, the process of precipitates formation is confined to a certain pH range.

1.5.2 Basic of impregnation method

Favored precipitation techniques like impregnation and drying are selected because they are straightforward and produce less waste streams. A metal precursor solution and a porous support interact to start the process. Precursors include inorganic metal salts such as metal sulfates, carbonates, chlorides, nitrates, or acetates as well as organic metal complexes like metal acetylacetonates. Due to the greater solubility of many precursors, water is the most widely used solvent for inorganic salts, but most precursors for organometallic compounds are dissolved in organic solvent. It is essential to keep concentrations below the saturation point to avoid early deposition of the metal precursor in bulk solution.

Wet impregnation (WI) and pore volume impregnation (PVI), sometimes known as incipient wetness impregnation (IWI), are two basic impregnation techniques. The latter term represents the impregnated material's continued macroscopic dryness [14].

After impregnation step, the material is subjected to drying, usually carried out at temperatures ranging from 80 °C and 200 °C. The objective is to remove the solvent introduced during impregnation. Various factors, such as the heating rate, final temperature, treatment duration, and atmospheric conditions, can affect the process and should be adjusted based on the specific system requirements [15].

In the final stage, there is a calcination phase, which an activation step; that includes heating them in an oxidizing atmosphere, typically at a temperature as high as or slightly higher than that of reaction. The goal of calcination is to breakdown the metal precursor, resulting in the production of metal oxide and the removal of both supplied cations and anions as well as gaseous byproducts (usually water and CO₂). Nanoparticles are produced as a result of this activation process [16].

1.6 Use of Support

Supported metal catalysis presents more advantageous stability and better activity in comparison to unsupported bulk metal catalysis and performs an important position in both its overall performance and sturdiness. The catalyst support must possess key properties including long surface area, exceptional electrical conductivity, robust corrosion resistance, uniform particle size distribution, and a cohesive force to retain catalyst particles. Moreover, it should allow the uniform dispersal of catalyst material on its surface and facilitate the catalyst' recovery [11]. Thus, the selection of support is important and significantly influences the catalyst's behavior, durability, performance, and cost-effectiveness. Supported catalysts have a pivotal role in wide range of electroanalytical field, including fuel cell technology, biosensing application, photo electrochemistry, the food industry, control drug delivery, and battery materials [17]. In electrocatalysis, various conductive metal oxides serve as catalyst support, providing better stability as compared to carbon in an oxidizing environment. These metal oxides also have an essential function in different fields, encompassing physics, chemistry, and material science.

1.6.1 Metal oxide as support materials

In recent times, metal oxides have garnered significant attention as stabilizing matrices within the realm of nanomaterial development. These materials have emerged as arising candidates for serving as catalyst support in various electroanalytical applications. The

following discourse highlights the metal oxides utilized as supporting material for electrocatalysis.

1.6.2 Alumina as electrocatalyst support

Interest in the Al-O system is concentrated on the Al_2O_3 composition because of its vital role as a catalyst element, adsorbent, and fundamental substance in different industrial applications. Furthermore, the advent of novel nanostructured, Alumina has enabled its utilization as a supporting medium for active phases in the field of catalysis. Alumina has many attractive properties that render it highly interesting for diverse applications. Notably, it exhibits exceptional hardness, stability, electrical insulation, and transparency. Among the seven polymorphs, the α , θ , γ , and δ phases are the most encountered and relevant in industrial processes [18].

1.6.3 Crystalline forms of Alumina

a. α - alumina

α -alumina, also referred to as corundum, is a stable crystalline form of alumina widely utilized in high-temperature environments. It can be obtained by heating γ -alumina or any hazardous oxide above 1000 °C. In the α -alumina structure, every aluminum atom is encircled by 6 oxygen atoms arranged in an octahedral pattern, while every oxygen atom is encompassed by four aluminum atoms, giving a close-packed lattice of oxygen ions in which aluminum ions are positioned tetrahedrally. α -alumina exhibits excellent chemical inertness, high hardness, and transparency, rendering it well-suited for diverse industrial processes. While resistant to acids, α -alumina shows reactivity toward water. Due to its unique properties, it plays a crucial role in high-temperature applications.

b. θ - alumina

The θ phase of alumina is a metastable phase that transforms to the α phase at approximately 1050 °C. It exhibits a lower density than α -alumina, with approximately 3600 Kg/m^3 compared to 4000 Kg/m^3 for α -alumina. It is highly ionic in nature. This form adopts a monoclinic geometry, where aluminum atoms occupy both octahedral and tetrahedral positions within close pack oxygen sublattice.

c. γ -alumina

γ -alumina is broadly applied as catalyst substrate because of its large surface area and considerable surface energy. γ -phase's low surface energy provides stability when the surface area is high relative to the bulk volume. However, a challenge that arises at high temperatures is that it transformed into the α phase at 700-800 °C. Despite this limitation, γ -alumina remains a critically important nano-sized material, finding its applications in automobile and petroleum industries, as well as in spacecraft structural composites [19]. Recent research has revealed that when a critical surface state is attained, γ -alumina exhibit greater thermodynamically stability compared to α -alumina [20]. The traditional structured of γ -alumina considered a cubic defect spinel-type arrangement involves oxygen atoms organized in cubic close-packed manner, while aluminum atoms occupy positions in both octahedral and tetrahedral sites [21].

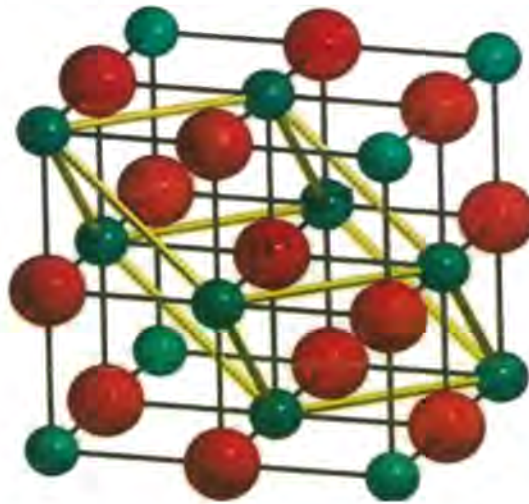


Figure 1.2. Cubic crystalline form of Al_2O_3 [22].

1.7 Transition Metal Oxides as Active Materials

Transition metals play a vital role in a wide range of industries due to their versatile applications. Particularly, they play a significant role in the chemical sector, serving as essential components in catalysts used for converting hydrocarbons into other valuable compounds.

Moreover, they find application as electrode materials in variety of electrochemical procedures. In their bulk form, transition metal oxides have low reactivity and possess wide

band gaps. However, when reduce to the Nano dimension, their bandgap magnitude changes, leading to a broad range of electronic configurations. Nanocrystalline transition metal oxides have center of considerable interest in both fundamental scientific investigation and commercial applications due to their exceptional and unparalleled chemical and physical attributes, which are unattainable in materials with bulk dimensions [23].

1.7.1 Iron oxide as an active component

1.7.1.1 Phases of iron oxide (Fe_2O_3)

Iron oxide (Fe_2O_3) exists in four distinct phases with varying magnetic properties:

- Alpha phase, or hematite (α - Fe_2O_3) shows antiferromagnetic properties.
- Beta phase, or (β - Fe_2O_3) displays paramagnetic behavior.
- Gamma phase, also referred to as maghemite (γ - Fe_2O_3), showcases ferromagnetic behavior.
- Epsilon phase, denoted as (ϵ - Fe_2O_3), possesses inherent ferromagnetic characteristics.

The way to produce epsilon Fe_2O_3 is gamma > epsilon > alpha > beta.

1.7.2 Applications of iron oxide

Iron oxides hold significant importance as essential transition metal oxides. These oxides have a wide range of uses as adsorbents, catalysts, sorbents, pigments, coating, flocculants, ion exchangers, gas sensor, and lubricants. Additionally, iron oxide nanocomposites show greater potential in areas like magnetic resonance imaging, magnetic recording, storage devices, toners, bioseparation, wastewater treatment, medicines, etc.

1.8 World Energy Crises and Renewable Energy Resources

The escalating world energy crises, driven by rapid industrialization and the alarming increase in pollution levels, have created a substantial gap between energy demand and availability. The increasing emissions of carbon dioxide and nitrogenous compounds into the atmosphere, possess critical challenges to environmental sustainability.

As reported by the International Energy Agency, in 2022, the global energy demand reached 18 TW, with approximately 85% derived from fossil fuels like coal, oil, and gas. According to new policies, substantial rise in energy demand from 18 TW in 2022 to 24 TW or 26 TW in 2040, along with a corresponding rise in CO₂ emissions from 32 Gt year⁻¹ in 2022 to 37 or 44 Gt year⁻¹ in 2040 [24]. Urgent action is required to develop technologies that enable the generation and storage of energy from renewable sources to meet the ever-increasing energy demands. Currently, renewable energy sources contribute only about 15% of total energy production. However, significant advancements in science and technology will make it possible to make these renewable sources viable alternatives to conventional non-renewable energy sources like oil, coal, gas, etc.

Some of the renewable energy sources are listed below:

- Hydropower
- Geothermal
- Fuel Cell
- Biomass
- Solar Energy

Renewable energy sources gained significant attention due to their remarkable attributes, including clean and eco-friendly energy production and long-term sustainability. Notably, hydrogen and oxygen can be produced through water splitting using electro/photochemical methods. The process of producing hydrogen and oxygen from water is discussed briefly in the coming context.

1.9 Water: An Ultimate Source of Hydrogen and Oxygen

(Electrochemical Water Splitting)

Water splitting is a thermodynamically non-spontaneous process that demands sufficient energy to take place. This energy can be provided from different renewable and non-renewable energy sources. Figure 1.3 represents the different methods of splitting water

using energy, including heat, electricity, bio-based processes, and light energy, either individually or in combination.

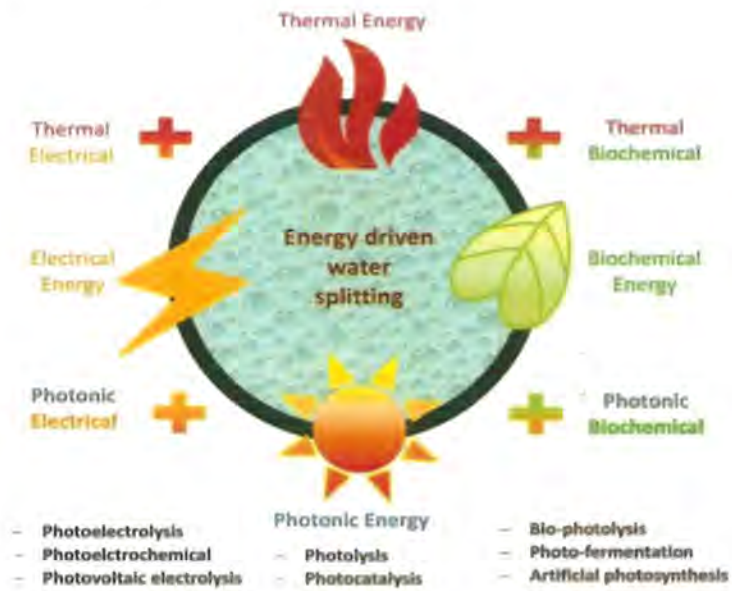


Figure 1.3. Different energy sources for water splitting [25].

Water electrolysis represents a highly promising and efficient technology for hydrogen production. This process has gained significant attention due to its negligible pollution, remarkable energy conversion efficiency, and wide-ranging applications. Electrochemical water splitting involves two half-reactions that occur at distinct electrodes: the anodic site facilitates the oxygen evolution reaction (OER), while the cathodic site facilitates the hydrogen evolution reaction (HER). Both reactions exhibit slow kinetics and a large overpotential barrier.

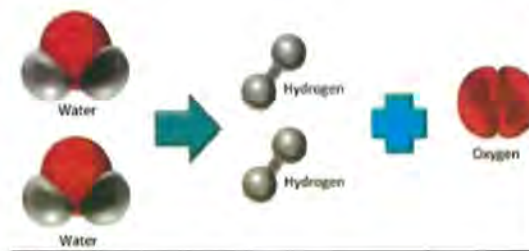


Figure 1.4. General representation of water splitting.

HER and OER processes with their potential is briefly discussed below:

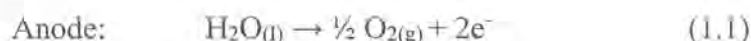
1.9.1 Hydrogen evolution reaction (HER)

HER is one of the half-reactions of water splitting, where protons are reduced to hydrogen (in an alkaline medium). It is a simple reaction requiring only two electrons per hydrogen molecule; however, multiple reactions can lead to an energy barrier and sluggish kinetics. In response to these challenges, scientists have developed various catalyst that shows enhanced catalytic performance for HER in both acidic and alkaline medium. The HER process involves three steps: adsorption of proton (H) on the catalyst surface (Volmer step), the pairing of two adsorbed hydrogen atoms (Tafel reaction), and the reaction between an adsorbed H atom and H⁺ (or H₂O) in the electrolyte (Heyrovsky reaction), resulting the formation of an H₂ molecule [26].

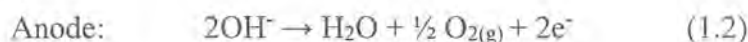
1.9.2 Oxygen evolution reaction (OER)

OER is anodic half-reactions of water splitting. It displays sluggish kinetics and requires significant overpotential. The water reduction/HER process is easy and demands lower onset potentials, however, the process of water oxidation is complex and hindered by slow kinetics, caused by substantial losses in the overpotential barrier for the transfer of four electron/protons [27, 28]. Consequently, the water oxidation reaction (WOR) demands an efficient electrocatalyst to overcome the challenges of generating oxygen in the electrochemical water splitting process [29, 30]. OER is a pH-dependent process. In a basic medium, hydroxyl (OH⁻) groups are oxidized, producing water and O₂ with a loss of electrons [31]. While in an acidic or neutral medium [32], water is oxidized to yield oxygen via the production of proton-electron couple. The anodic reactions involved in the splitting of water in acidic and alkaline media are presented below:

Acidic media:



Alkaline media:



Alkaline media is preferred for water oxidation because we can use low-cost materials (nickel and cobalt *etc.*) as electrocatalysts in a basic medium. These materials become corroded in an acidic medium. The OER consists of four steps and requires four

electrons for its completion. Figure 1.5 represents the four-step mechanism of OER in an alkaline medium.

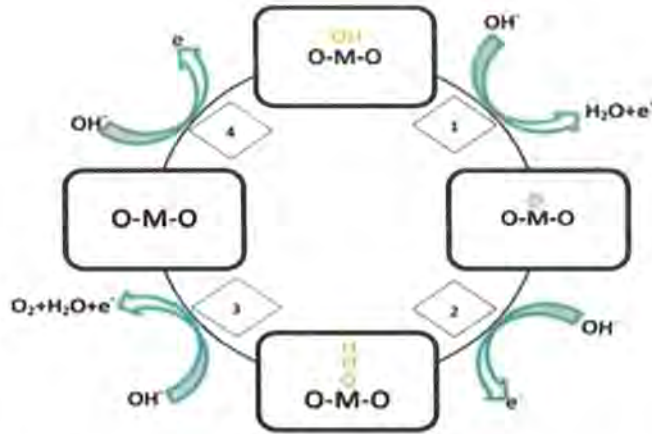


Figure 1.5. Proposed OER mechanism in alkaline medium [33].

The kinetics of the OER reaction changes by changing the pH of the medium (~59 mV potential changes per unit pH). Overall water splitting with their corresponding potential in both (acidic and basic) media are summarized below [34, 35]:

In an acidic medium:



In alkaline medium:



Thermodynamically, the potential required for water electrolysis is 1.23 V, which corresponds to the standard Gibbs free energy value of 237.1 kJ/mol. The OER process requires a large overpotential value to reach the appreciated J values (current density).

That's why in actual applications the input potential is greater than the theoretical one. So, it is an urgent need to develop such a type of catalyst that reduces this large overpotential barrier and increases the output current. Initially, noble metals including platinum (Pt), ruthenium (Ru), and iridium (Ir) are proposed, which have high efficiency in HER/OER reactions but due to their limited availability and elevated costs, scientists focus on the development of cost-effective and highly efficient electrocatalyst [36]. In this manner, various metal alloys [37], nitrides [38], carbides [39], and borides [40] have been observed to be electrocatalysts in acidic mediums, however, metal oxides [30] and metal hydroxides [41] are effective catalysts in basic mediums.

1.10 Characterization Techniques

The synthesized materials can be quantitatively and qualitatively analyzed using a variety of characterization techniques. These cutting-edge methods include X-ray diffraction analysis (XRD), Fourier transformer infrared spectroscopy (FTIR), scanning electron microscopy (SEM), energy dispersive X-ray (EDS), cyclic voltammetry (CV), electrochemical impedance spectroscopy (EIS), and chronoamperometry. The following is a succinct introduction to these methods:

1.10.1 X-ray diffraction (XRD)

X-ray diffraction analysis is a powerful non-destructive and useful analytical method used for studying crystalline materials. It offers valuable information regarding the structure, preferred crystal orientation (texture), phases, and various structural aspects like crystallinity, crystal defects, average grain size, and strain. The (0.5 and 2.5 Å) wavelength of X-rays is selected as they have the same order as (d) spacing of crystal plans at the atomic level of materials and thin sheets. XRD is also employed for the recognition of material because each crystalline substance possesses a distinct diffraction pattern which serves as a fingerprint for their characterization and phase determination [42].

1.10.1.1 *Basic principle of X-ray diffraction (XRD) technique*

The XRD technique is based on the famous Bragg's diffraction law, which establishes a quantifiable link between the wavelength of incident radiation, diffraction angle, and lattice spacing within a crystalline material. The Figure 1.6 depicts a clear explanation of Bragg's law.

$$n\lambda = 2d\sin\theta \quad (1.9)$$

n = An integer

λ = Wavelength of the X-ray

d = Path difference (spacing between crystal layers)

θ = Angle of incidence

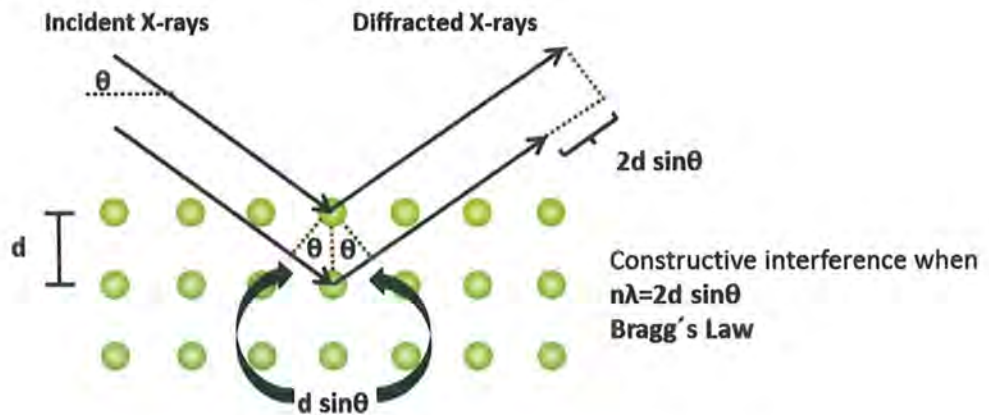


Figure 1.6. Bragg's diffraction.

This technique involves the interference of monochromatic X-ray (either constructive or destructive) and as-synthesized crystalline material. Monochromatic radiations are produced through cathode ray tube. A collimator concentrates monochromatic radiation and then directs it toward the sample [42].

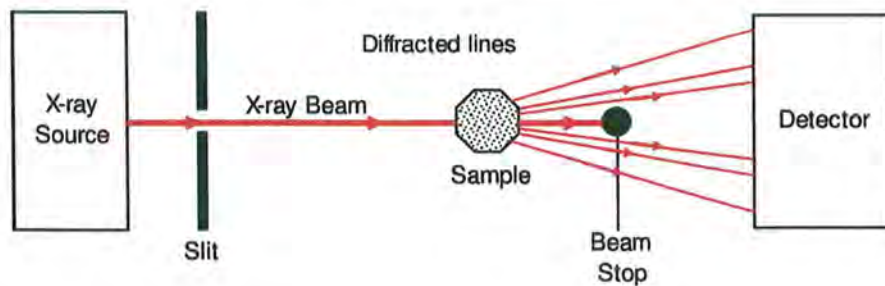


Figure 1.7. Schematic diagram of the diffractometer configuration [43].

In this method, the intensity of scattered X-rays is plotted with respect to diffraction angle, wavelength, and polarization. The XRD pattern of synthesized material is matched

with the standard then its crystalline phase can be determined. The pattern is obtained or plotted using the X-rays powder diffractometer software [44].

X-ray is scattered from some specific angle of lattice planes, giving the diffraction pattern in the form of peaks. Therefore, the XRD pattern gives us an atomic arrangement of materials and quick identification of phases for the enormous number of crystalline materials.

1.10.1.2 Calculations for crystallite size

The average crystallized size or sub-microparticle can be determined by using Debye-Scherrer's formula [45]. This equation is written as,

$$D_{av} = \frac{k\lambda}{\beta \cos\theta} \quad (1.10)$$

where,

k = Shape factor (its value is equal to 0.89)

λ = Wavelength of the incident X-rays beam

β = Full width at half maximum height

θ = Diffraction angle

1.10.1.3 XRD's advantages

This technique offers several advantages, including determining crystal structure in unknown materials and calculating grain or single crystal orientation. It precisely measures interlayer spacing between atoms and require minimal sample preparation. Additionally, it accurately finds the thickness of multi-layer structures and thin films and distinguishes between crystalline and amorphous materials, while its data interpretation is straightforward and simple.

1.10.2 Fourier transform infrared spectroscopy (FT-IR)

FT-IR is a quite sensitive method that is applied to identify the chemical bonds within the molecule and the functional groups present in a particular compound. This method is particularly utilized for the identifying organic compounds across a wide array of applications, and can also characterize certain inorganic compounds [46]. It also confirms

the structure of a molecule, as each functional group exhibit unique peaks within the IR region, covering the range from 400-4000 cm^{-1} .

1.10.2.1 Working principle

FT-IR works on the principle that the molecules show absorption of electromagnetic radiation in the IR region. This absorption corresponds mainly to the vibration of the bond present in the molecule.

In this technique, the sample is subjected to IR radiation. The sample absorbs a portion of IR radiation and allows some to pass through (transmitted) it. The outcome pattern illustrates the molecular absorption and emission generating a molecular fingerprint of the material that matches the frequencies of vibrations among the bonds of the atoms composing the material. Given that each material possesses a unique structure and atomic arrangement, it follows that no two compounds exhibit an identical IR pattern.

Consequently, infrared spectroscopy can lead to the identification (qualitative analysis) of various material. Moreover, the magnitude of a peak in the spectrum directly corresponds to the quantity of material present. Figure 1.8 represents the instrumentation of an FTIR spectrophotometer.

1.10.2.2 Instrumentation

The normal IR spectrophotometer setup has following parts: light Source, interferometer, sample, detector, and computer.

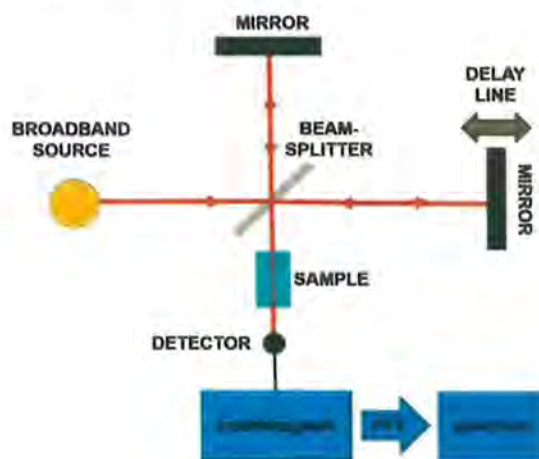


Figure 1.8. FTIR spectrometer instrumentation [47].

1.10.2.3 Advantages of FT-IR

This technique is a non-destructive, internally calibrated, and highly sensitive. It can enhance the velocity by capturing a scan every second, all while maintaining mechanical simplicity with just one moving part.

1.10.3 Scanning electron microscopy (SEM)

SEM stands as a remarkably versatile and robust method employed for examining the surface morphology of catalyst. The first micrograph using SEM was used by Zworykin et al. (1942) for surface characterization of a solid specimen [48]. The new advancement in science and technology added features in SEM to study the composition, morphology, and topography of SEM as presented in Figure 1.9.

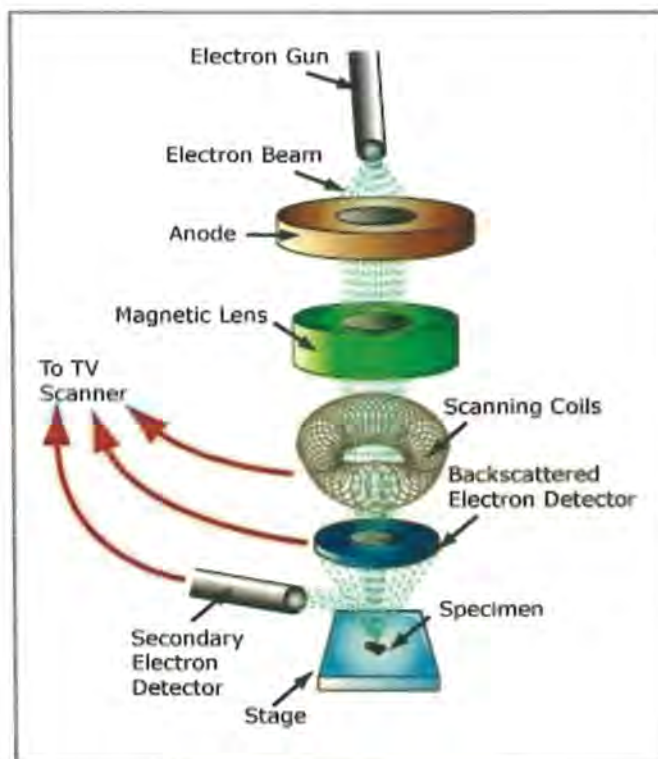


Figure 1.9. Basic components of SEM setup [49].

1.10.3.1 Principle of SEM analysis

The fundamental concept behind SEM involves the generation of an electron beam, its interaction with the catalyst surface, and output signals recorded by the detector. A typical SEM instrument consists of an electron column, scanning system, vacuum system,

detector(s), display, and electronic control. A brief description of the component role is given:

- An electron gun is used to generate an electron beam.
- Condenser lens used to determine the size of electron beam.
- The objective lens focused this beam on the surface of the specimen.
- A detector used to detect the signal.

The interaction of primary electrons with the specimen produces a signal in the form of electromagnetic radiation. Secondary electrons are generated by the interaction with the nuclei of the atoms in the sample, which are detected by a suitable detector. X-rays are generated by the relaxation of excited electrons and collected selectively to form an image [50].

Electrons with energy 3-5 eV provide the surface and topography information whereas the electrons with energy greater than 50 eV give information about relatively deep regions and are sensitive to the composition of the sample [51]. SEM analysis provides the 3D image of the sample. It is a non-destructive technique so the sample can be used for repeated analysis.

1.10.3.2 Applications of scanning electron microscopy (SEM)

This technique is valuable for characterizing nanostructured materials, assessing their size, shape, particle agglomeration, and porosity. It also excels in characterizing thin films, determining their thickness, uniformity, porosity, and composition. Additionally, it aids in investigating membrane morphology, including aspects like swelling, mechanical strength, pore size and catalyst dispersion.

1.10.4 Energy dispersive X-rays spectroscopy (EDS)

EDS is a microanalytical method that can be employed for elemental analysis of synthesized materials. X-ray microanalysis coupled with an electron beam instrument, usually, an SEM, can quantitatively and qualitatively analyze synthesized material. In a Multi-technique line, EDX has become a powerful technique, especially in contamination

analysis and forensic science investigations. The technique is non-destructive, and samples are examined with little or no sample preparation.

1.10.4.1 Basic principle of EDX

In EDX, an energy source (electron beam of electron microscopy) used for the excitation of sample and caused to emit some of the absorbed energy by expelling an inner-shell electron. The difference in energy is subsequently released as an x-ray with a distinctive spectrum dictated by the atom of origin when an outer-shell electron with a greater energy fills the empty space left behind. The composition and analysis of a specific sample volume that has been electrified by the energy source are made possible as result. In qualitative analysis, the element identification relies on peak positions in the spectrum, whereas quantitative analysis associates the element's concentration with the signal' intensity [52]. Figure 1.10 represents the working principle of EDS:

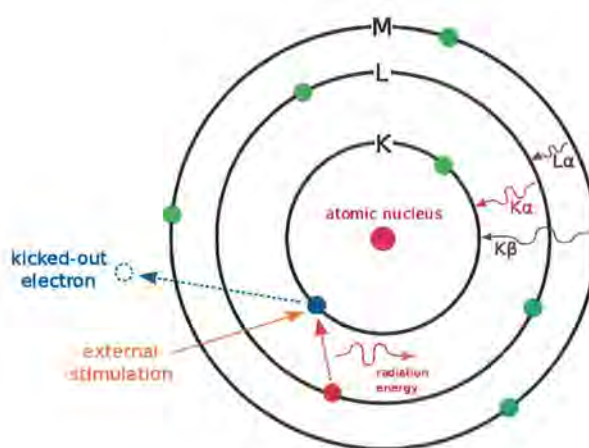


Figure 1.10. Working principle of EDS [49].

1.10.5 Cyclic voltammetry (CV)

Cyclic voltammetry is used to study the electrochemistry of any analyte. CV is an effective and sensitive technique that provides information about different processes occurring at the electrode surface, it also gives a lot of information about the kinetics and thermodynamics of heterogeneous electron transfer process and various coupled chemical reactions. To study the electrochemical behavior of the desired material, three-electrode system is used. The over-all assembly of three electrodes is known as an electrochemical cell, it has a

analysis and forensic science investigations. The technique is non-destructive, and samples are examined with little or no sample preparation.

1.10.4.1 Basic principle of EDX

In EDX, an energy source (electron beam of electron microscopy) used for the excitation of sample and caused to emit some of the absorbed energy by expelling an inner-shell electron. The difference in energy is subsequently released as an x-ray with a distinctive spectrum dictated by the atom of origin when an outer-shell electron with a greater energy fills the empty space left behind. The composition and analysis of a specific sample volume that has been electrified by the energy source are made possible as result. In qualitative analysis, the element identification relies on peak positions in the spectrum, whereas quantitative analysis associates the element's concentration with the signal' intensity [52].

Figure 1.10 represents the working principle of EDS:

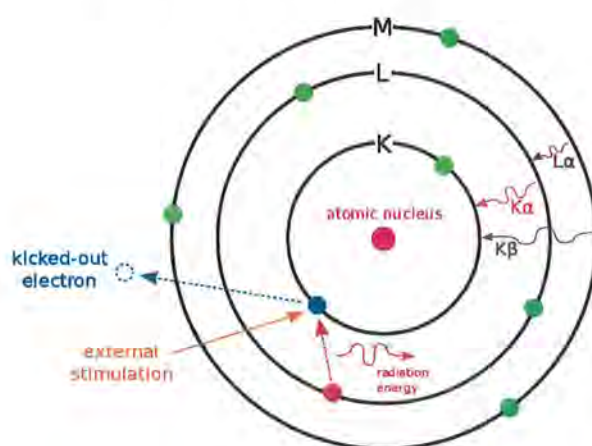


Figure 1.10. Working principle of EDS [49].

1.10.5 Cyclic voltammetry (CV)

Cyclic voltammetry is used to study the electrochemistry of any analyte. CV is an effective and sensitive technique that provides information about different processes occurring at the electrode surface, it also gives a lot of information about the kinetics and thermodynamics of heterogeneous electron transfer process and various coupled chemical reactions. To study the electrochemical behavior of the desired material, three-electrode system is used. The over-all assembly of three electrodes is known as an electrochemical cell, it has a

working, counter, and a reference electrode. A voltammogram is obtained as a result of cyclic voltammetry which is a plot between current and voltage.

In CV experimentation, the potential of the working electrode is linearly swept and plotted against time, Figure 1.11 (a). In detail, a known potential is introduced between the working and the reference electrode, and the output current response is assessed between the working and counter electrode. Initially, the potential provided to the working electrode is swept in the forward direction and then in reverse direction after the adjusted potential value and the cycles are repeated to get the cyclic form of voltammogram.

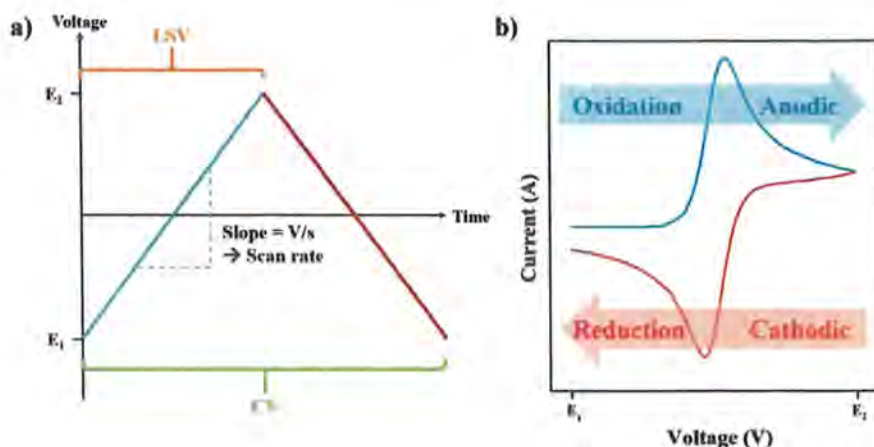


Figure 1.11. (a) An excitation signal of CV/LSV, (b) A typical cyclic voltammogram representing anodic and cathodic peaks for a single reversible electron transfer process [53].

1.10.5.1 Categorization of redox processes

By employing cyclic voltammetry, diverse parameters like anodic current; I_{pa} , cathodic current; I_{pc} , and their corresponding potentials, peak width, formal potential, and many other related parameters can be investigated. These parameters lead to the classification of redox process into three primarily types:

- Reversible process
- Irreversible process
- Quasi-reversible process

1.10.5.1.1 Reversible process

Two conditions are met by reversible processes: (i) I_{pa}/I_{pc} , where the ratio of anodic and cathodic peak currents is unity, and (ii) the peak potential is being independent of scan rate. The peak current for a reversible process is determined using the Randles-Sevcik equation.

$$I_p = 2.69 \times 10^5 n^{3/2} A C D^{1/2} v^{1/2} \quad (1.11)$$

Here I_p represents peak current (ampere), n shows the number of electrons, A is the surface area of electrode (cm^2), C is the concentration of analyte (mol.cm^{-3}), D is the diffusion coefficient ($\text{cm}^2.\text{s}^{-1}$), and the v is the scan rate (Vs^{-1}).

Reversible processes are quite fast, and the total number of electrons involved in the process can be determined using the following equation.

$$\Delta E_p = E_{pa} - E_{pc} = (0.059/n) V \quad (1.12)$$

Anodic and cathodic peak potentials are unaffected by variations in scan rate when $E_{p/2}$ is taken not account rather than E_p . This corresponds to the potential at $I_p = 0.5I_p$, and half-wave potential can be expressed as follows:

$$E_{p/2} = E_{1/2} \pm 28/n \text{ (mV) at } 298 \text{ K} \quad (1.13)$$

The + and - signs of potentials show the oxidation and reduction processes, respectively.

1.10.5.1.2 Irreversible process

In an irreversible process, peak separation arises due to slow kinetics, leading to peak separation greater than $59/n$ mV. The peak potential varies based on the scan rate, and the peak current can be calculated using the equation:

$$I_{pa} = 2.99 \times 10^5 n^{3/2} \alpha^{1/2} A C D^{1/2} v^{1/2} \quad (1.14)$$

Here α represents the transfer coefficient, reflecting the symmetry of the energy barrier in terms of transfer coefficient. Its value lies within the range of 0-1. The peak separation is related to the number of electrons involved by the following relation:

$$n = 4 I_p RT / FQ v \quad (1.15)$$

1.10.5.1.3 Quasi-reversible process

This process shows intermediate behavior between reversible and irreversible processes. In these processes, the peak height observed in the forward scan rate with a high magnitude but is less pronounced in the backward scan. The peak potential depends upon the scan rate and peak separation is higher than 60 mV at a high scan rate. Heterogeneous rate constants for these processes typically range from 2×10^{-2} to 3×10^{-4} cm^{-1} . The Figure 1.12 represents the cyclic voltammogram for reversible, irreversible, and quasi-reversible electrochemical processes.

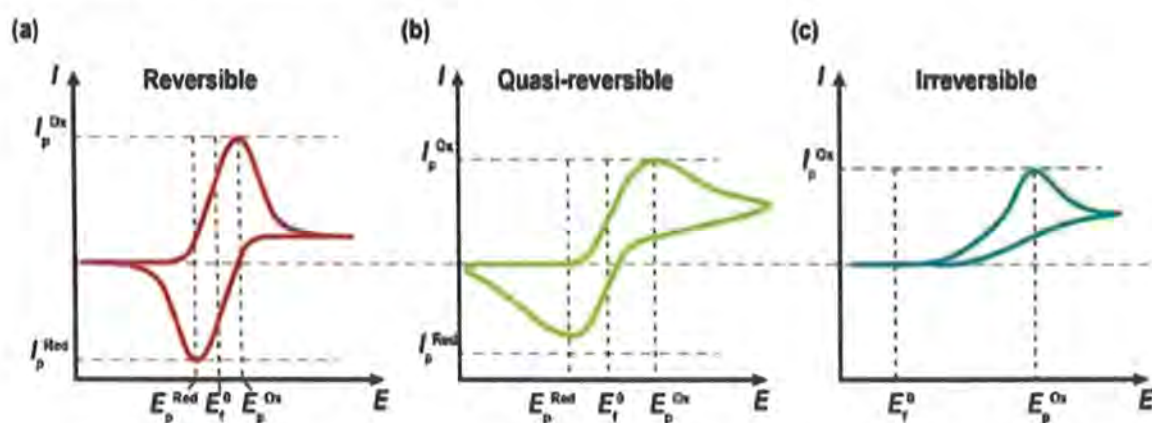


Figure 1.12. Cyclic voltammograms for (a) reversible, (b) quasi-reversible, and (c) irreversible process [54].

1.10.6 Linear sweep voltammetry (LSV)

LSV technique quite like cyclic voltammetry, is simple but efficient method. However, in LSV scan, voltage is swept linearly from one to another potential limit. This technique reveals the kinetics of irreversible systems, where a unidirectional scan provides valuable insights, while the reverse scan offers limited information. Like cyclic voltammetry, linear sweep voltammetry makes use of a three-electrode setup to determine peak current, peak potential, and various electrochemical parameters. Thus, it emerges as a viable alternative to cyclic voltammetry.

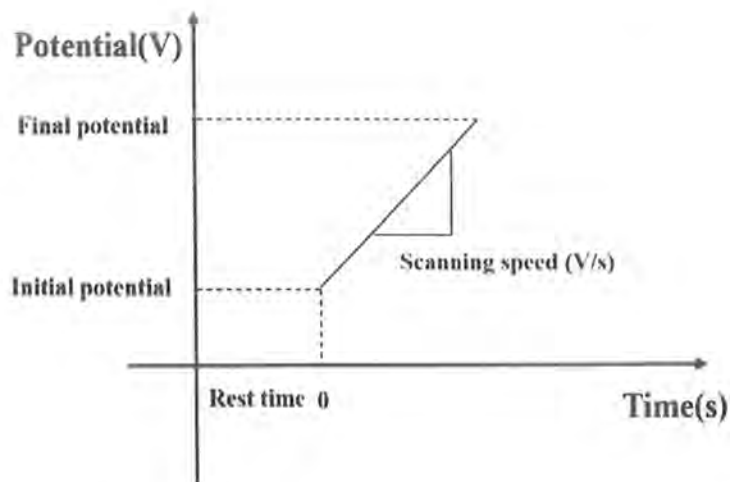


Figure 1.13. LSV potential sweep with time [55].

1.10.7 Electrochemical impedance spectroscopy (EIS)

EIS is applied to understand the nature and mechanism of redox processes deeply. The technique involves measuring a process's response toward applied potential. It's also quite valuable in distinguishing different processes occurring in EC cells due to the distinct relaxation times of each process. In EIS, the sample is subjected to an AC voltage excitation signal at different frequency ranges and the current responses are usually studied and displayed in the form of the Nyquist and the Bode plots.

In recent years, EIS has found extensive application in electrochemical characterizations which may include fuel cells, coatings, batteries, and corrosion processes. It has also been identified as a significant tool for examining a range of mechanisms in electrochemistry-related subjects such as electro dissolution, electrodeposition, passivity, and corrosion study. This technique getting famous for its effectiveness in probing semiconductor surfaces and the diffusion of ion across the membranes [56].

1.10.7.1 Basic principle

Using conventional electrochemical methods cannot allowed for a complete understanding of the electrochemical reaction occurring at the electrode-electrolyte interface. However, a detailed investigation needs keen understanding of the process taking place. A complete description requires the particulars of different components present in the system via

variation in their impedance over a broad frequency range and different potential values [57].

Applying AC perturbation as $V(\omega)$ of various frequencies to an EC system under investigation and measure the output current response $I(\omega)$ constitute the basic strategy of the EIS method. The system's impedance $Z(\omega)$ can then be calculated using Ohm's law as follows:

$$Z(\omega) = V(\omega) / I(\omega) \quad (1.16)$$

This ratio between dependent voltage and current is known as the impedance, $Z(\omega)$, of the system. Impedance is a resistance, and it is a complex entity with a variable magnitude. It is also dependent on frequency therefore, varying the frequency of the applied signal can affect the impedance of the system.

1.10.7.2 Data representation

In electrochemical impedance spectroscopy, the data is described in two simple ways, namely the Nyquist plot and the Bode plot presented in Figure 1.14. The plot of the real part against the imaginary part of impedance gives a Nyquist plot, which is the most popular format. The Bode plot includes the factor of frequency (f) and phase angles (ϕ). The advantage of Nyquist over Bode representation gives a qualitative interpretation of data with a quick overview. However, the drawback of Nyquist representation is that this format lacks the frequency dimension of the data.

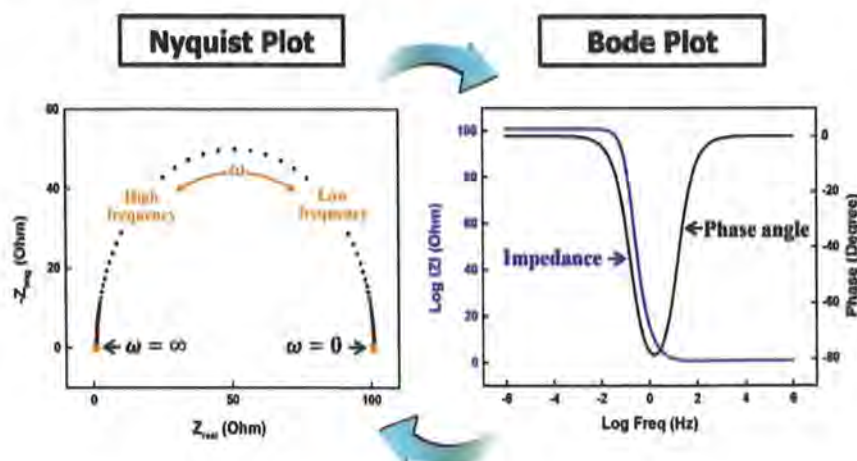


Figure 1.14. Nyquist and Bode plots for representation of EIS spectra [58].

1.10.7.3 Data analysis

When employing electrochemical impedance spectroscopy to analyze electrochemical systems, it is necessary to interpret the results with the use of appropriate models. These models can be classified into two types: equivalent circuit models and process models. The models have successfully analyzed the experimental data and can predict the system's behavior under various conditions. This modeling is achieved using various software tools.

1.10.7.4 Equivalent circuit model

The equivalent circuit model is commonly employed used to interpret impedance data and is constructed through well-known various elements. These components consist of capacitors, inductors, resistors, and distributed elements such as CPE, constant phase element, and diffusion resistance or Warburg impedance. For the complete description of an electrochemical cell, these circuit elements can be combined in both series and parallel arrangements, forming a complex equivalent circuit.

1.10.8 Chronoamperometry

Chronoamperometry is used to study the kinetics and different reaction processes of electrochemical systems. In this electrochemical method, the potential applied to the working electrode is stepped, while monitoring the resulting current from faradic processes occur at the electrode over time. Chronoamperometry is usually performed for stability tests and to study the variation in current by changing the experimental conditions [59].

1.11 Aims and Objectives

The main objectives of the current research work are:

- a) To synthesize the pure Al_2O_3 nanoparticles and (1, 2, 3, 4, 5, and 10%) compositions of $\text{Fe}_2\text{O}_3@/\text{Al}_2\text{O}_3$ via precipitation and impregnation methods, respectively.
- b) To evaluate the synthesized materials with the help of different physical and electrochemical characterization techniques.
- c) To analyze the diverse role and application of $\text{Fe}_2\text{O}_3@/\text{Al}_2\text{O}_3$ as electrocatalytic material towards water oxidation.

- d) Study the role of methanol as facilitating agent on OER activity of synthesized materials.
- e) To evaluate various kinetics parameters from cyclic voltametric study at different scan rates.

1.12 Plan of work

This research will be focused on the preparation of such materials which can be used as potential alternatives to existing materials like noble metal oxides for electrochemical applications. Synthesis of pure aluminum oxide and different compositions of $\text{Fe}_2\text{O}_3@Al_2O_3$ will be carried out by using precipitation and impregnation methods, respectively. Structural and morphological properties of the synthesized material will be studied by using different characterization techniques like XRD, FTIR and SEM/EDX, while electrocatalytic activity will be investigated for OER studies in an alkaline environment.

1.13 Thesis layout

The present thesis deal with the synthesis, characterization, and electrochemical applications of all synthesized $\text{Fe}_2\text{O}_3@Al_2O_3$ materials. This dissertation is comprised of three chapters, the first chapter includes the introduction of nanotechnology, catalysis, metal oxides materials, water oxidation and introduces characterization techniques used in current work. The second chapter includes the detailed experimental scheme followed for the synthesis of Al_2O_3 and impregnated compositions $\text{Fe}_2\text{O}_3@Al_2O_3$. The third chapter includes the comprehension of results from various morphological and electrochemical studies of prepared materials for OER process. Conclusions are added at the end of the thesis.

Chapter 2

Experimental

This chapter includes the scheme for the preparation of alumina and the coating of iron oxide nanoparticles on alumina for the formation of an electroactive catalyst. Different physical and chemical synthesis methods have been adopted for their synthesis. Iron oxide coated alumina was synthesized in a two-step process: precipitation method was used to synthesize catalyst support (Al_2O_3) and then active component (Fe_2O_3) was loaded from iron nitrate solution on this catalytic support *via* impregnation technique according to weight percentages. To electrochemically study of synthesized material; the glassy carbon electrode (GCE) was modified by a simple drop-cast method.

2.1 Chemicals and Reagents

Table 2.1 contains the names and chemical formulae of all the chemicals used in the synthesis of metal oxide and metal oxide hybrid catalysts and electrochemical investigations of materials. All chemicals were analytical grade, and all acquired from Sigma Aldrich in their pure form (99.9%); therefore, no additional treatment was required.

Table 2.1. Chemicals used in the synthesis of compositions and in electrochemical preparations.

Sr. No.	Name of Chemical	Chemical Formulae
1	Aluminum(III) nitrate nonahydrate	$\text{Al}(\text{NO}_3)_3 \cdot 9\text{H}_2\text{O}$
2	Iron(III) nitrate nonahydrate	$\text{Fe}(\text{NO}_3)_3 \cdot 9\text{H}_2\text{O}$
3	Ammonium hydroxide	NH_4OH
4	Potassium ferricyanide trihydrate	$\text{K}_3[\text{Fe}(\text{CN})_6] \cdot 3\text{H}_2\text{O}$
5	Potassium chloride	KCl
6	Nafion (5 wt./V% solution)	$\text{C}_7\text{HF}_{13}\text{O}_5\text{C}_2\text{F}_4$
7	Methanol	MeOH
8	Ethanol	$\text{C}_2\text{H}_5\text{OH}$

2.2 Synthesis of pure aluminum oxide (γ - Al_2O_3)

The precipitation method was employed to synthesize aluminum oxide (Al_2O_3), intended for use as a catalyst. An aqueous solution containing 1M aluminum nitrate nona hydrate ($\text{Al}(\text{NO}_3)_3 \cdot 9\text{H}_2\text{O}$) was prepared. The initial pH of the experiment was recorded at 2.0. To adjust the pH to 9 [60], a 3 M ammonia solution was gradually added dropwise to the precursor salt solution at a rate of 1 mL min^{-1} . The solution's temperature was maintained at $60 \text{ }^\circ\text{C}$, and consistent stirring at 400 RPM to complete and homogeneous precipitation of aluminum hydroxide ($\text{Al}(\text{OH})_3$). Subsequently, white gelatinous ppts of $\text{Al}(\text{OH})_3$ were produced. These precipitates were allowed to remain under reaction conditions for an hour. This was succeeded by a 24-hour aging process, during which the precipitates were left in contact with the supernatant liquid at room temperature. Following this aging step, the precipitates underwent several rounds of filtration and subsequent washing with deionized water. The washed precipitates were then dried in an oven at $80 \text{ }^\circ\text{C}$ and then finely crushed. Ultimately, the powder was subjected to calcination at $800 \text{ }^\circ\text{C}$ to achieve the gamma alumina phase (γ - Al_2O_3) [61].

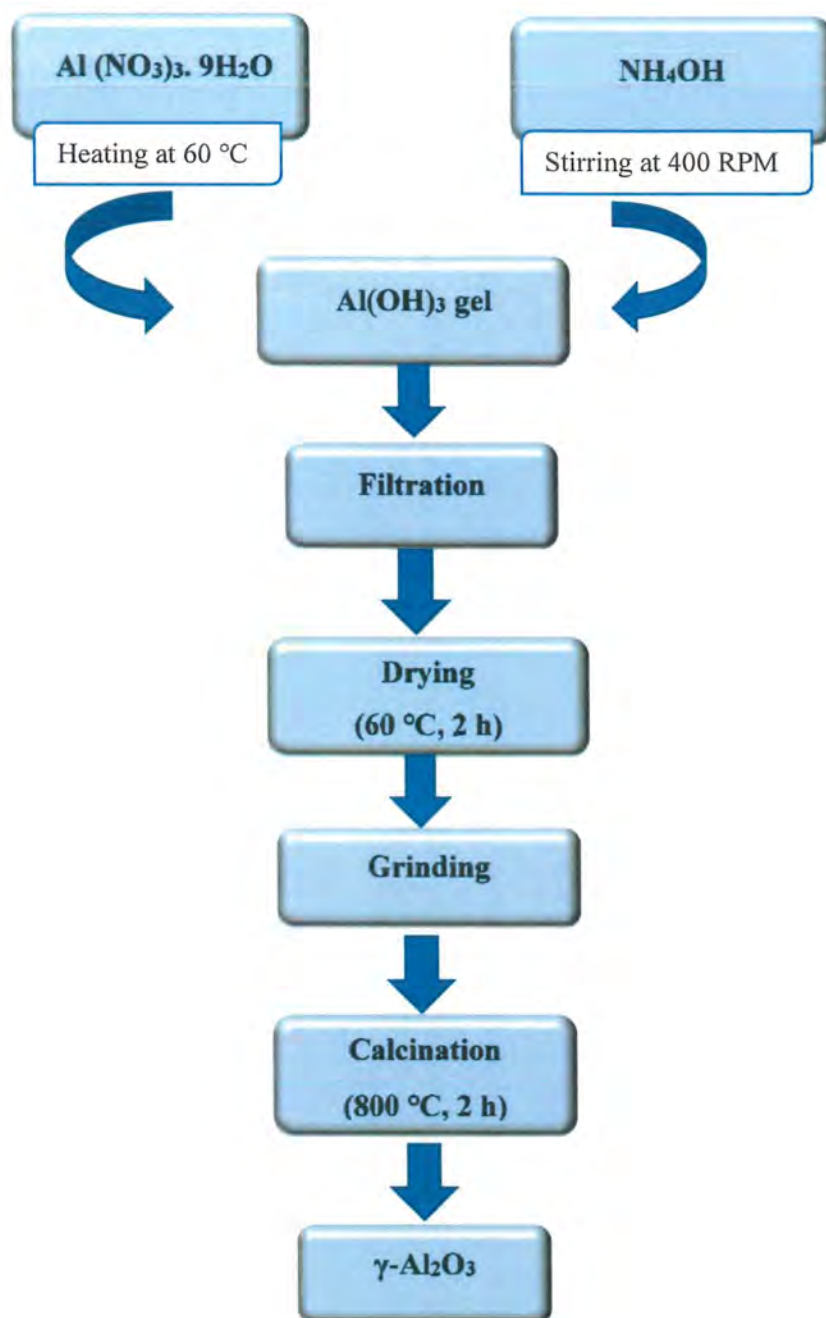


Figure 2.1. Schematic representation of the synthesis of γ -alumina.

2.3 Synthesis of impregnated catalysts ($\text{Fe}_2\text{O}_3@Al_2\text{O}_3$)

The impregnation of Fe_2O_3 onto all substrates followed the wt./wt.% method, employing a consistent procedure. For this purpose, predetermined quantity of pre-dried support was wetted with the appropriate volume of 1 M iron nitrate nonahydrate ($\text{Fe}(\text{NO}_3)_3 \cdot 9\text{H}_2\text{O}$)

solution, resulting in impregnated Fe_2O_3 compositions of 1-5 and 10 wt.%. After soaking overnight, samples were dried, ground, and calcined at $500\text{ }^\circ\text{C}$ for 2 hours. The final catalyst samples were finely powdered using acetone, and then dried. Figure 2.2 represents the general scheme for the synthesis of impregnated compositions. Sample codes, compositions, and molecular formulae for all the synthesized materials are given in Table 2.5.

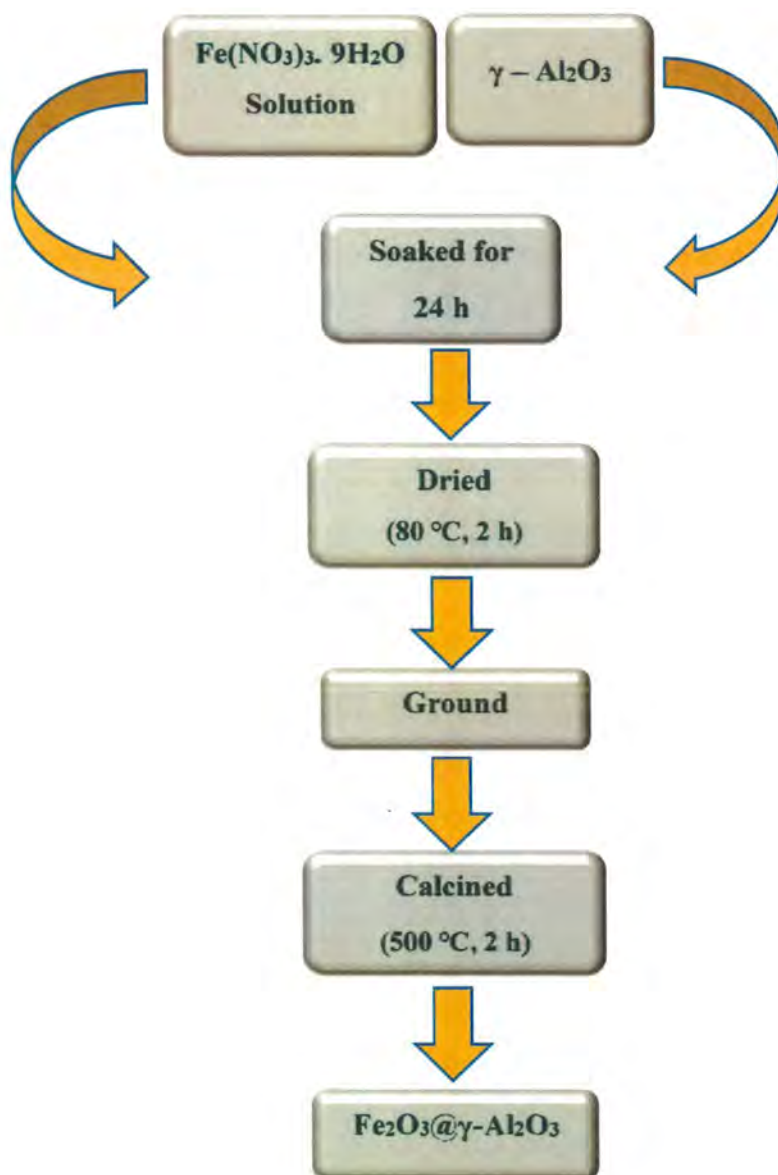


Figure 2.2. Scheme for the synthesis of $\text{Fe}_2\text{O}_3@ \gamma\text{-Al}_2\text{O}_3$.

Table 2.2. Sample codes and molecular formulae for the synthesis compositions.

Molecular formulae	Sample codes
$Al_{2.00}O_{3\pm\delta}$	Al_2O_3
$Al_{1.98}Fe_{0.02}O_{3\pm\delta}$	AlFe-1
$Al_{1.96}Fe_{0.04}O_{3\pm\delta}$	AlFe-2
$Al_{1.94}Fe_{0.06}O_{3\pm\delta}$	AlFe-3
$Al_{1.92}Fe_{0.08}O_{3\pm\delta}$	AlFe-4
$Al_{1.90}Fe_{0.10}O_{3\pm\delta}$	AlFe-5
$Al_{1.80}Fe_{0.20}O_{3\pm\delta}$	AlFe-10

2.4 Electrode Modification

Electrode modification has been a vibrant realm of interest in the field of electrochemistry since 1979 [62]. The modified electrode has a monolayer or a few micrometers thick layer of chemical compounds. An electrode is modified by coating the thin film of the desired material on the surface of the electrode. In terms of physical, chemical, electrochemical, optical, electrical, transport, and other beneficial qualities, modified electrodes differ from unmodified ones. Electron transport is a process that takes place on the surface of the electrode. For a modified electrode, electro-catalysis induced by an oxidation-reduction substance, facilitating the transfer of electrons from the electrodes to reactants.

2.4.1 Procedure for electrode modification

Glassy carbon (GC) electrode was chosen as a working electrode simply due to its low background current, good surface chemistry, low economic cost, and wide potential window [63]. Prior to modification, GC was polished on a felt pad using 0.3 μ m alumina powder to eliminate any impurities from electrode surface. Notably, electrode polishing is done by making digit eight in alumina water slurry instead of circular motion which damages the surface of the electrode [64]. After polishing, it was rinsed with deionized water and subjected to ultrasonication in deionized water for 1 min. to ensure the removal

of any loosely attached alumina particles. Subsequently, the electrode was left to air-dry at room temperature. The drop cast method was employed to modify the electrode [65].

To modify the electrode, first, it was wetted with 2 μL of pure ethanol followed by 0.1 mg of finely grounded powdered catalyst sample, and then 2 μL of 0.5% Nafion solution was drop casted. Nafion is a multifunctional copolymer binder, employed as a binding and dispersing agent in electrochemical research due to its electrochemical and mechanical robustness [66]. The prepared electrode is dried in the oven for 30 minutes. Now, the prepared modified GC/ Fe_2O_3 @ Al_2O_3 /Nafion electrode was utilized to gather the electrochemical data. Prior to each electrochemical measurement, preconditioning procedure were carried out in the appropriate potential windows for each type of modified electrode. As a result, the background current was minimized, and the voltammogram was stable.

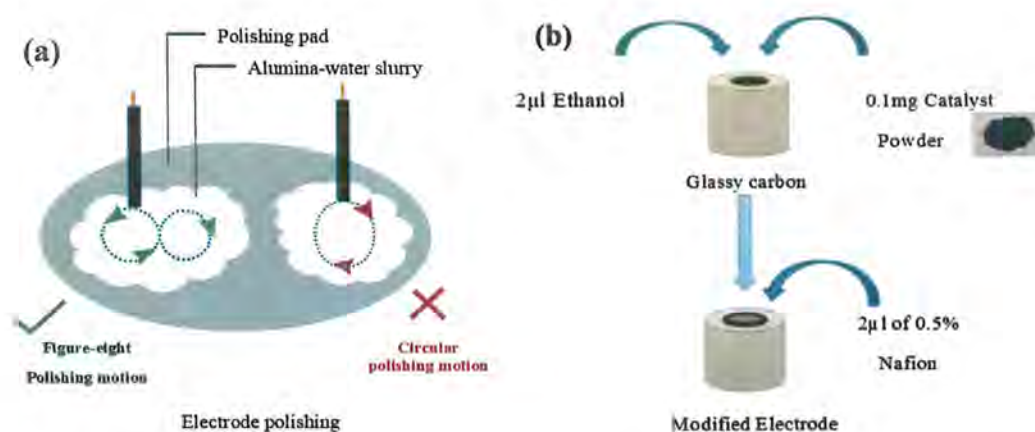


Figure 2.3. Electrode polishing (a) Drop cast method for preparation of working electrode (b).

2.5 Instrumentation

Using various analytical techniques, synthetic materials were analyzed for their physical, chemical, and electrochemical properties. The particulars of instrumentation and applied conditions are as follows.

2.5.1 X-ray diffraction (XRD) measurements

The analysis of crystal structure of the synthesized materials was carried out using powder XRD (PANalytical X'PERT high score's diffractometer) using $\text{Cu K}\alpha$ of 0.154 nm

radiation. All the XRD data was performed in the scan range of 20-80° with a scan rate of 0.625 s.

2.5.2 FT-IR instrumentation

FT-IR analysis was conducted using a spectrometer provided by Thermo Scientific (NICOLET 6700).

2.5.3 Scanning electron microscopy (SEM)

Scanning electron microscopy (SEM) was performed to examine the morphological characterization of all synthesized compositions using TESCAN scanning electron microscopy obtained from Germany.

2.5.4 Gamry Potentiostat/ Galvanostat

All the electrochemical investigations were carried out at room temperature using a potentiostat interface with an accuracy of ± 5 pA in current and ± 1 mV in potential readings. Gamry interface 1000 was also used for electrochemical impedance spectroscopy (EIS) measurements with an ac amplitude signal of 5 mV over the frequency range of 0.1 - 100 kHz and varying dc voltages.

Cell assembly

All electrochemical experiments were carried out using a conventional three-electrode cell configuration. With a diameter of 3 mm and a surface area of 0.07 cm², modified glassy carbon was utilized as the working electrode, a platinum wire was employed as the counter electrode due to its inertness and high surface, and an Ag/AgCl was used as the reference electrode. All the acquired data was referenced against Ag/AgCl (3M KCl) electrode. Using the Nernst equation, the current densities were normalized to the geometric area of the electrode and potentials were transformed to a reversible hydrogen electrode (RHE) scale for straightforward comparison with the data presented in the literature [67].

$$E_{(RHE)} = E_{(Ag/AgCl)} + E^{\circ}_{(Ag/AgCl)} + 0.059pH \quad (2.1)$$

Here $E_{(RHE)}$ is the potential of the RHE scale, $E_{(Ag/AgCl)}$ is the potential with reference to Ag/AgCl reference electrode, $E^{\circ}_{(Ag/AgCl)}$ is the standard potential of Ag/AgCl (3 M KCl) *i.e.*, 0.197 V, and pH factor is incorporated in the equation as OER, in the alkaline environment, is a pH-dependent process. All electrodes were equidistantly placed in an

electrochemical cell, represented in Figure 2.4. All the solutions were prepared in finely deionized water and 10 mL of supporting electrolyte was used each time to collect cyclic voltammetric data.

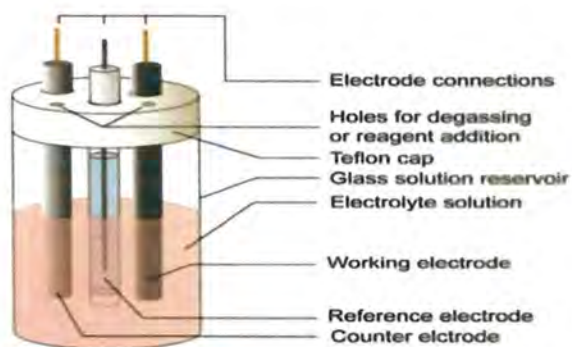


Figure 2.4. Electrochemical cell assembly.

Chapter 3

Results and Discussion

A series of iron oxide impregnated γ - Al_2O_3 hybrid catalysts with varying compositions (1%, 2%, 3%, 4%, 5%, and 10% Fe_2O_3 coated onto γ - Al_2O_3) were synthesized and subjected to both physical and electrochemical characterization. The evaluation of redox properties and catalytic performance was investigated using advanced techniques, namely electrochemical impedance spectroscopy and catalytic voltammetry.

3.1 Physical Characterization

3.1.1 X-ray diffraction analysis (XRD)

The XRD pattern of the calcined γ - Al_2O_3 is presented in Figure 3.1 (a). Gamma alumina phase observed for sample calcined at 800 °C. The diffraction peaks of γ - Al_2O_3 were obtained at $2\theta = 36.90^\circ$, 45.38° , and 66.68° , having (311), (400), and (440) crystal planes, compared with the standard reference pattern of γ - Al_2O_3 JCPDS No. 00-001-1308, Figure 3.1 (b). All peaks agreed well to the reference pattern.

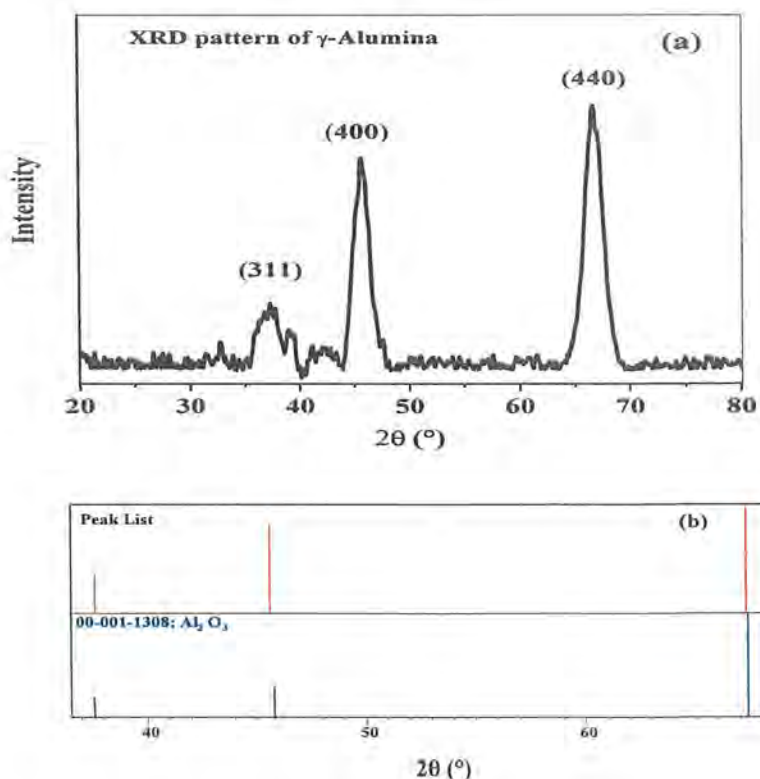


Figure 3.1. XRD pattern of γ - Al_2O_3 (a), and reference pattern of γ - Al_2O_3 (b).

XRD patterns for all loaded compositions are presented in Figure 3.2. Figure 3.2 (i), is dominated by diffraction lines of γ - Al_2O_3 without any lines for Fe_2O_3 , describing that Fe_2O_3 is highly dispersed on alumina substrate. Upon increasing the Fe_2O_3 loading to 2% (Figure 3.2 (ii)), indicating the phase formation of small Fe_2O_3 crystallites. The two main peaks at 45.38° and 66.68° , assigned at gamma alumina, were still prominent at the higher loadings. The intensity of the peaks increases, with the increase in Fe_2O_3 content. Hence, these results confirmed the phase purity of the sample.

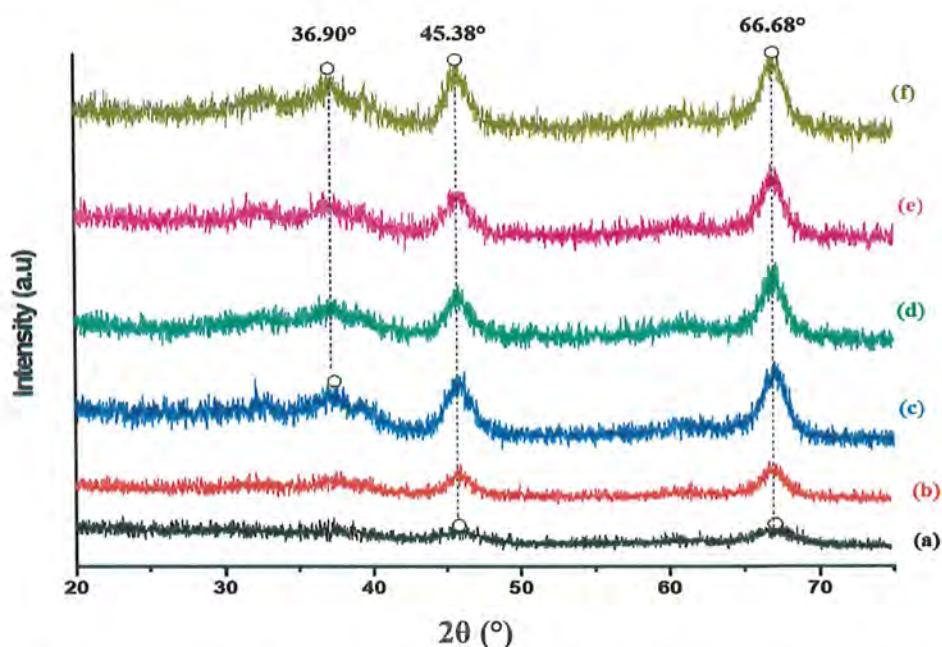


Figure 3.2. XRD patterns for (a) AlFe-1, (b) AlFe-2, (c) AlFe-3, (d) AlFe-4, (e) AlFe-5, and (f) AlFe-10.

The average crystallite size of γ - Al_2O_3 and loaded composition were obtained using the Debye-Scherrer formula [68], presented in Table 3.1.

Table 3.1. Average crystallite sizes of synthesized materials.

Sample	D _{av} (nm)
Al ₂ O ₃	11
AlFe-1	13
AlFe-2	16
AlFe-3	17
AlFe-4	12
AlFe-5	15
AlFe-10	32

The small crystallite sizes within the nanometer range are illustrated of the good electrocatalytic potential of the synthesized materials as this could be ascribed to the greater surface area of enhanced electrocatalysis.

3.1.2 FT-IR analysis

FT-IR of alumina-based catalyst shows poorly resolved bands due to low crystallinity. Strong broadband appeared around 400-1000 cm⁻¹, which represents Al-O vibrations [69]. Broad and smooth absorption bands in 400-900 and 3200-3700 cm⁻¹ ranges are clear. They are related to the Al-O (AlO₆ and AlO₄), *i.e.*, hexa-coordinated and tetra-coordinated aluminum, and O-H stretching vibration, respectively. IR spectra of all the Fe₂O₃@Al₂O₃ catalysts showed absorption bands at around 527 cm⁻¹, 463 cm⁻¹, and 420 cm⁻¹ showing stretching and bending vibration modes of Fe-O bonds. This implies that Fe₂O₃ has been successfully incorporated into the Al₂O₃ matrix and the samples are mixed composites of Fe₂O₃@Al₂O₃.

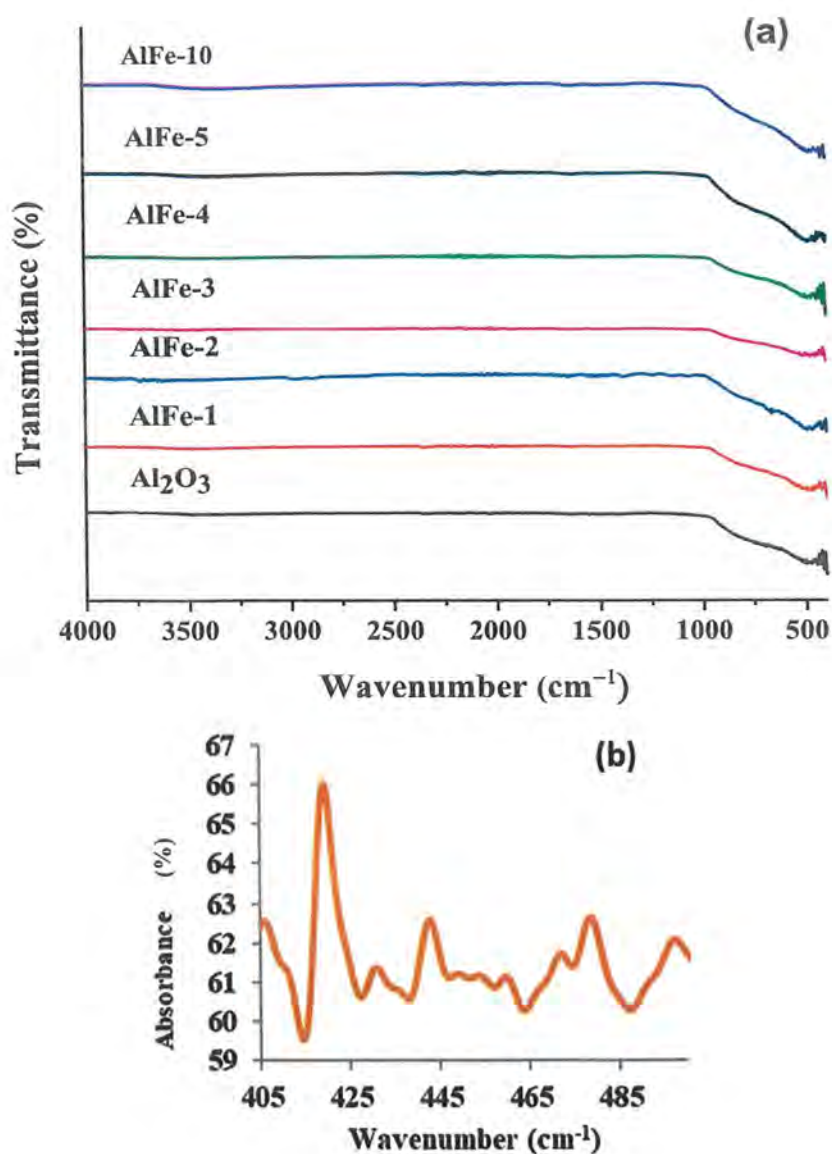


Figure 3.3. (a) FT-IR spectra of Al_2O_3 , Al-Fe-1, Al-Fe-2, AlFe-3, AlFe-4, AlFe-5, and AlFe-10, (b) IR region highlighting Fe-O and Al-O absorption peaks.

3.1.3 Scanning electron microscopy (SEM)

All samples were subjected to scanning electron microscopy and energy-dispersive X-ray spectroscopy for the evaluation of surface morphology and phase purity of the synthesized nanoparticles. For electrocatalytic applications, materials must offer a large surface area to the reacting species. SEM micrographs of Al_2O_3 are presented in Figure 3.4 (a and b) and EDX spectrum with elemental compositions are presented in Figure 3.4 (c).

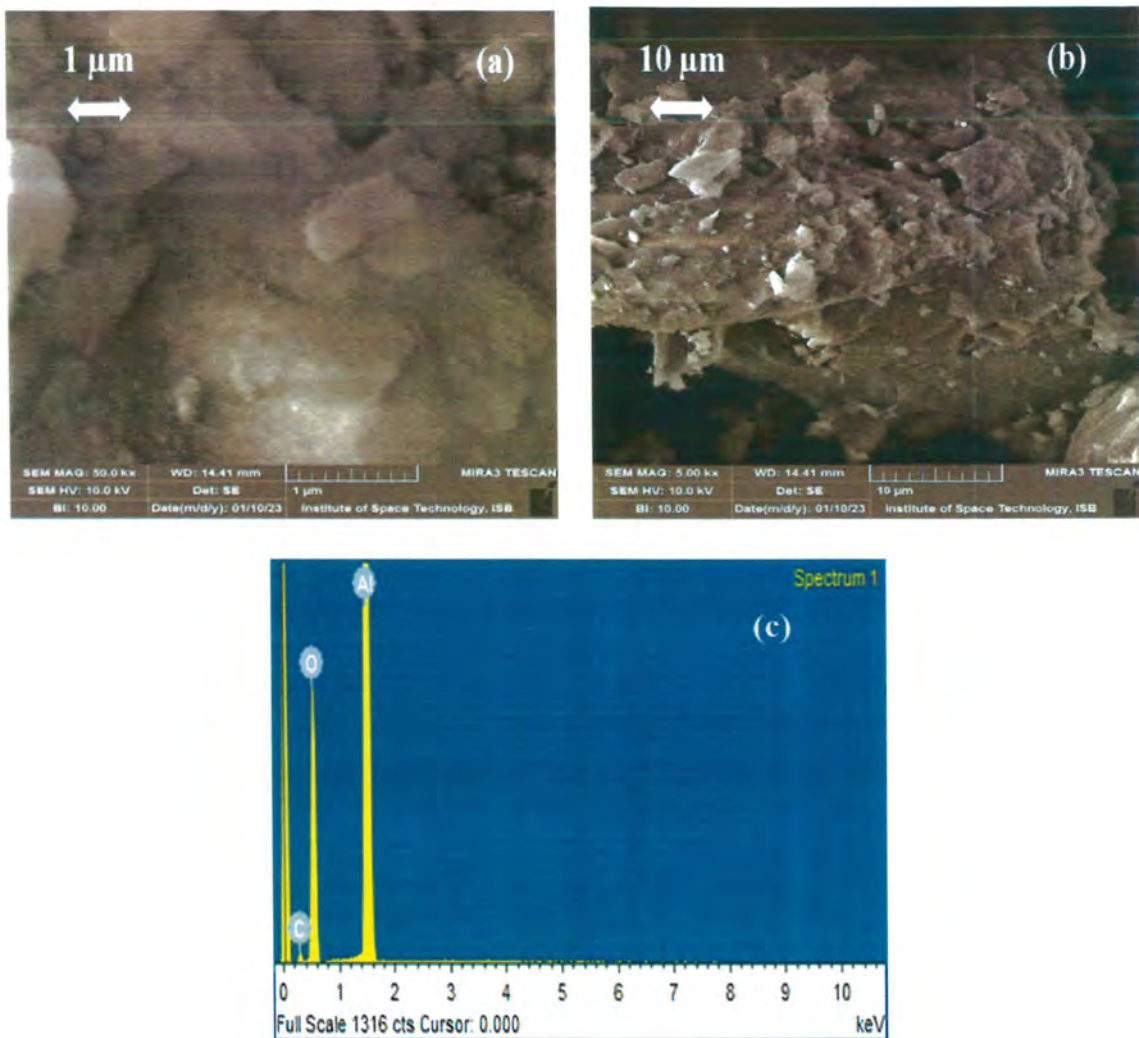


Figure 3.4. SEM micrographs of Al_2O_3 (a) at 1 μm , (b) at 10 μm , and (c) EDX spectrum of Al_2O_3 .

The micrographs at 1 μm revealed agglomerated structure, while at 10 μm , irregular-shaped particles of Al_2O_3 were observed with irregular sizes and shape distribution. SEM and EDX were also carried out for impregnated compositions, results are presented in Figure 3.5 and Figure 3.6, respectively.

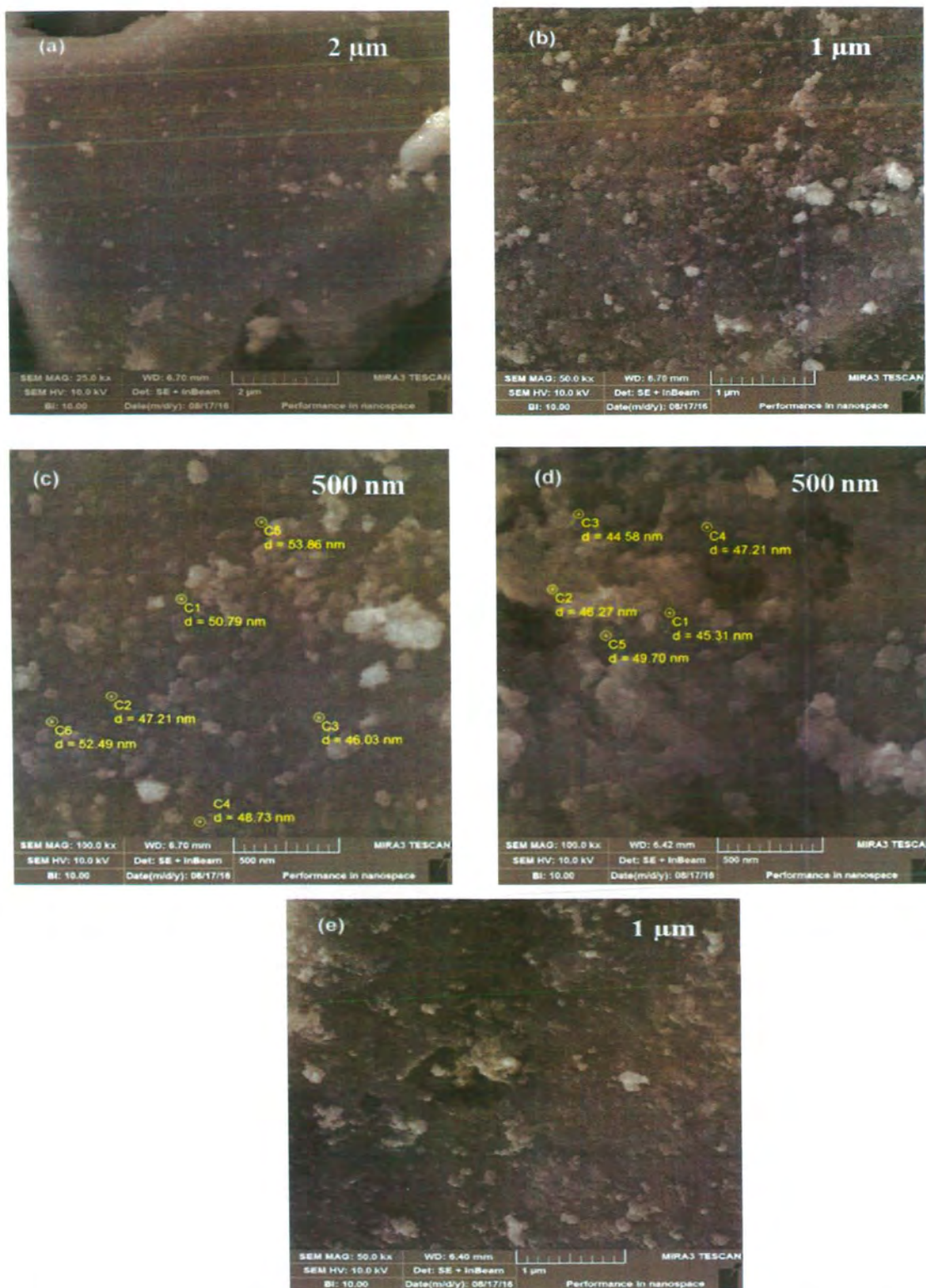


Figure 3.5. SEM micrographs at different resolutions for (a) AlFe-1, (b) AlFe-2, (c) AlFe-3, (d) AlFe-4, and (e) AlFe-5.

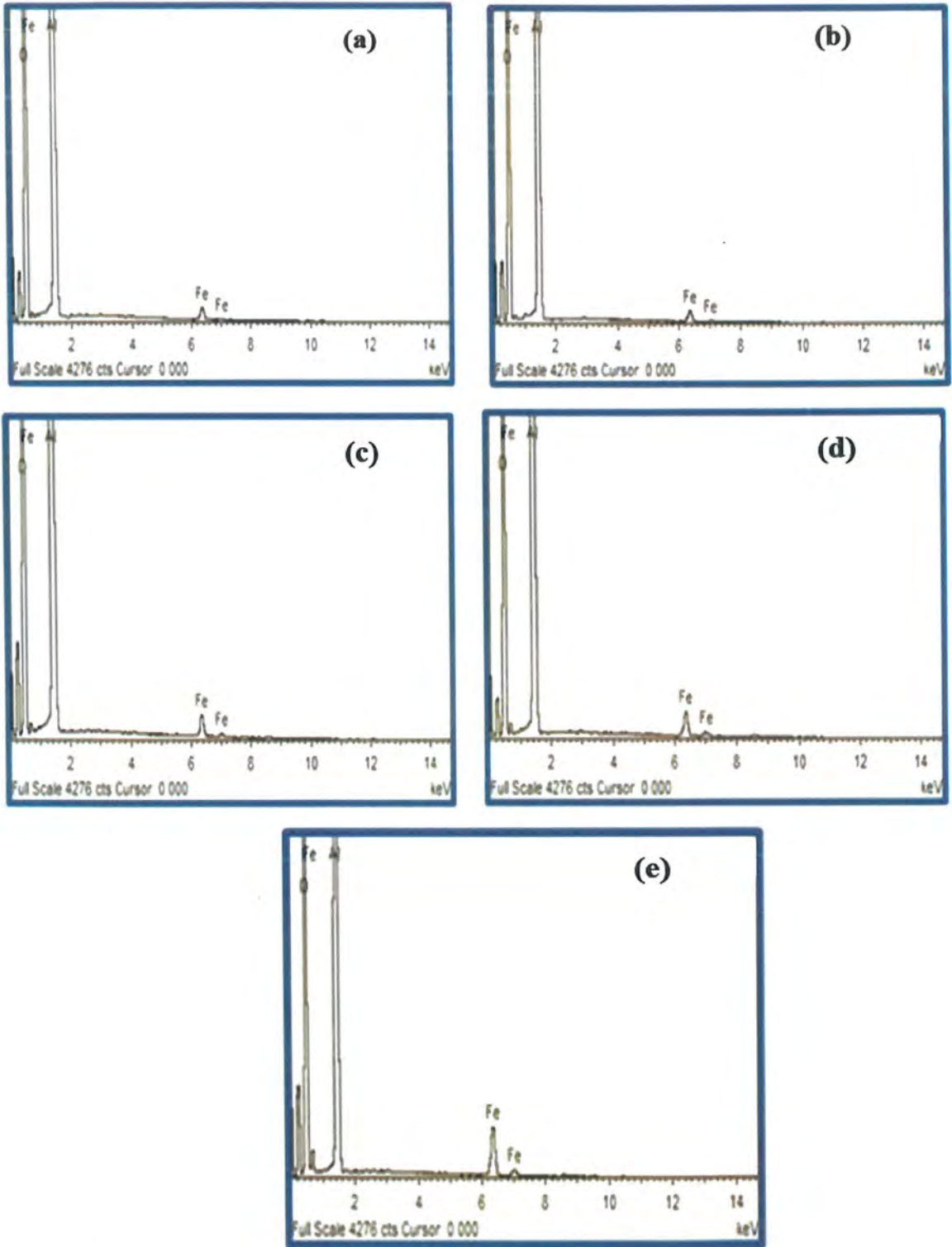


Figure 3.6. EDX spectra for (a) AlFe-1, (b) AlFe-2, (c) AlFe-3, (d) AlFe-4, (e) AlFe-5, and (f) AlFe-10.

SEM micrographs of $\text{Fe}_2\text{O}_3@\text{Al}_2\text{O}_3$ revealed the spherical particles, and that the iron oxide was homogeneously dispersed onto gamma-alumina support. The elemental composition of all synthesized materials was determined using EDX analysis. Phase homogeneity is deduced from the EDX analysis, revealing the presence of peaks corresponding to elements Al, Fe, and O. The data obtained from EDX analysis was in accordance with the expected concentrations, which confirm to the right synthesis route for synthesized nano powders. The elemental weight% for all synthesized materials are presented in Table 3.2.

Table 3.2. Elemental weight% from EDX analysis.

Electrocatalysts	Fe wt%	O wt%	Al wt%
Al_2O_3	-	52.57	45.00
AlFe-1	1.25	54.50	44.25
AlFe-2	2.41	53.85	43.74
AlFe-3	2.86	53.60	43.54
AlFe-4	4.05	52.99	42.96
AlFe-5	4.93	52.75	42.32
AlFe-10	10.05	51.84	38.12

3.2 Electrochemical Characterization

The electrochemical properties of all the modified glassy carbon electrodes were analyzed through cyclic voltammetry. To prepare electrodes, the synthesized materials underwent modification using the drop cast technique. Subsequently, the prepared electrodes were subjected to electrochemical characterization to determine their redox potential and investigate the active surface area.

3.2.2 Estimation of active surface for modified electrodes

The conductive behavior of all the synthesized materials were analyzed by employing cyclic voltammetry and impedance measurements in a solution containing potassium ferricyanide and KCl. The active surface area of the modified electrode was calculated through the utilization of cyclic voltammetry within an electrochemical cell containing a 5

mM potassium ferricyanide solution and 1 M KCl solution at 0.1 Vs⁻¹. CV profiles for all the catalyst-modified electrodes are presented in Figure 3.7 (a). Ferricyanide solution was used because it is considered the standard due to its favorable adsorption and desorption characteristics on the electrode surface, establishing it as a reliable reference for this analysis. Distinct current responses observed for all the electrodes indicated different properties exhibited towards the ferricyanide system.

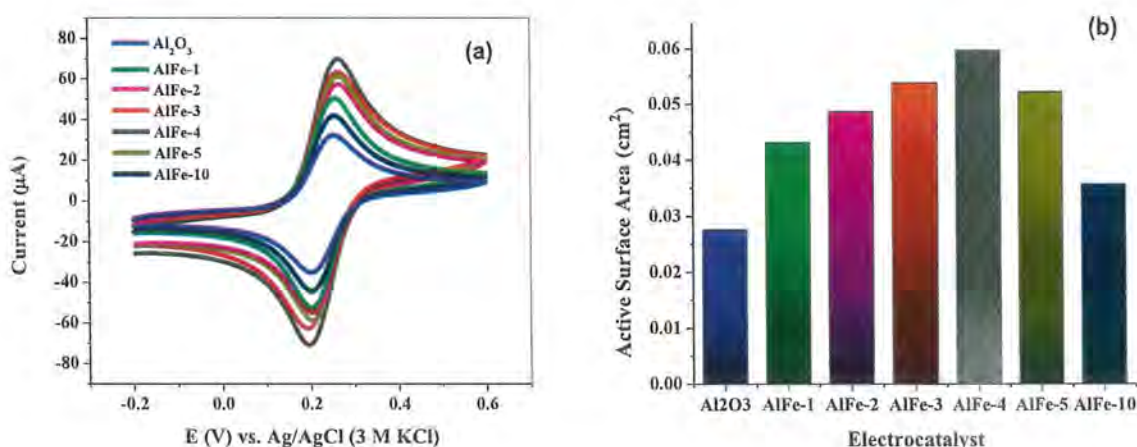


Figure 3.7. Cyclic voltammetry response of all modified electrodes for Fe²⁺/Fe³⁺ redox system in 5 Mm K₄[Fe(CN)₆] and 1 M KCl, (b) Graphical representation of comparative active surface areas of all modified electrodes.

The Randles-Sevcik [70] equation holds a prominent position as a benchmark tool in evaluating the reversibility of redox system and is commonly used for estimating the active surface area of a working electrode. The Randles-Sevcik equation for reversible redox process is given as,

$$I_{pa} = 2.69 \times 10^5 \times AC (n^3 D_0 \nu)^{1/2} \quad (1.14)$$

D₀ is the diffusion coefficient having value of 0.76 × 10⁻⁵ cm²s⁻² at 25 °C. From this investigation using Randles-Sevcik equation has been found range of active surface area from 0.027 to 0.060 cm². The peak currents and their respective active surface areas for all the modified electrodes are presented in Table 3.3.

Table 3.3. Peak current values and active surface area of modified electrodes.

Electrocatalysts	I_{pa} (μA)	Active Surface Area (cm^2)
Al_2O_3	32.36	0.027
AlFe-1	50.54	0.043
AlFe-2	57.02	0.049
AlFe-3	63.09	0.054
AlFe-4	70.05	0.060
AlFe-5	61.16	0.052
AlFe-10	41.78	0.036

The active surface area of all the modified electrodes followed an increasing order: $1\%Fe_2O_3@Al_2O_3 < 2\%Fe_2O_3@Al_2O_3 < 3\%Fe_2O_3@Al_2O_3 < 4\%Fe_2O_3@Al_2O_3$. However, the calculated values for $5\%Fe_2O_3@Al_2O_3$ and $10\%Fe_2O_3@Al_2O_3$ showed a decrease in active surface area, which can be attributed to particle agglomeration resulting from higher Fe_2O_3 loading.

3.2.2 Electrochemical impedance spectroscopy (EIS)

Electrochemical impedance spectroscopy (EIS) was utilized to investigate the electron transfer process across various electrodes, utilizing the Fe^{3+}/Fe^{2+} redox couple of the ferrocyanide system as a reference. The Figure 3.8 illustrates the Nyquist plots obtained from all modified electrodes, revealing two distinct regions in the impedance spectra, (i) A semicircle observed in the high- frequency range, which corresponds to a process where electron-transfer is limited. The diameter of this semicircle is equivalent to the electron transfer resistance (R_{ct}), a pivotal parameter that relates to the kinetics of the redox probe at the electrode interface; (ii) An inclined section observed at lower frequencies that corresponds to the diffusion process. This part is called the Warburg resistance (R_w) [71], which is associated with the semi-infinite diffusion of redox species towards the modified electrode.

For $K_4[Fe(CN)_6]$ solution, R_{ct} values reduced from $1\%Fe_2O_3@Al_2O_3$ to $4\%Fe_2O_3@Al_2O_3$ until the optimal loading was achieved. A lower R_{ct} value suggests the

transportation of electron transport at the electrode surface, attributed to higher conductivity.

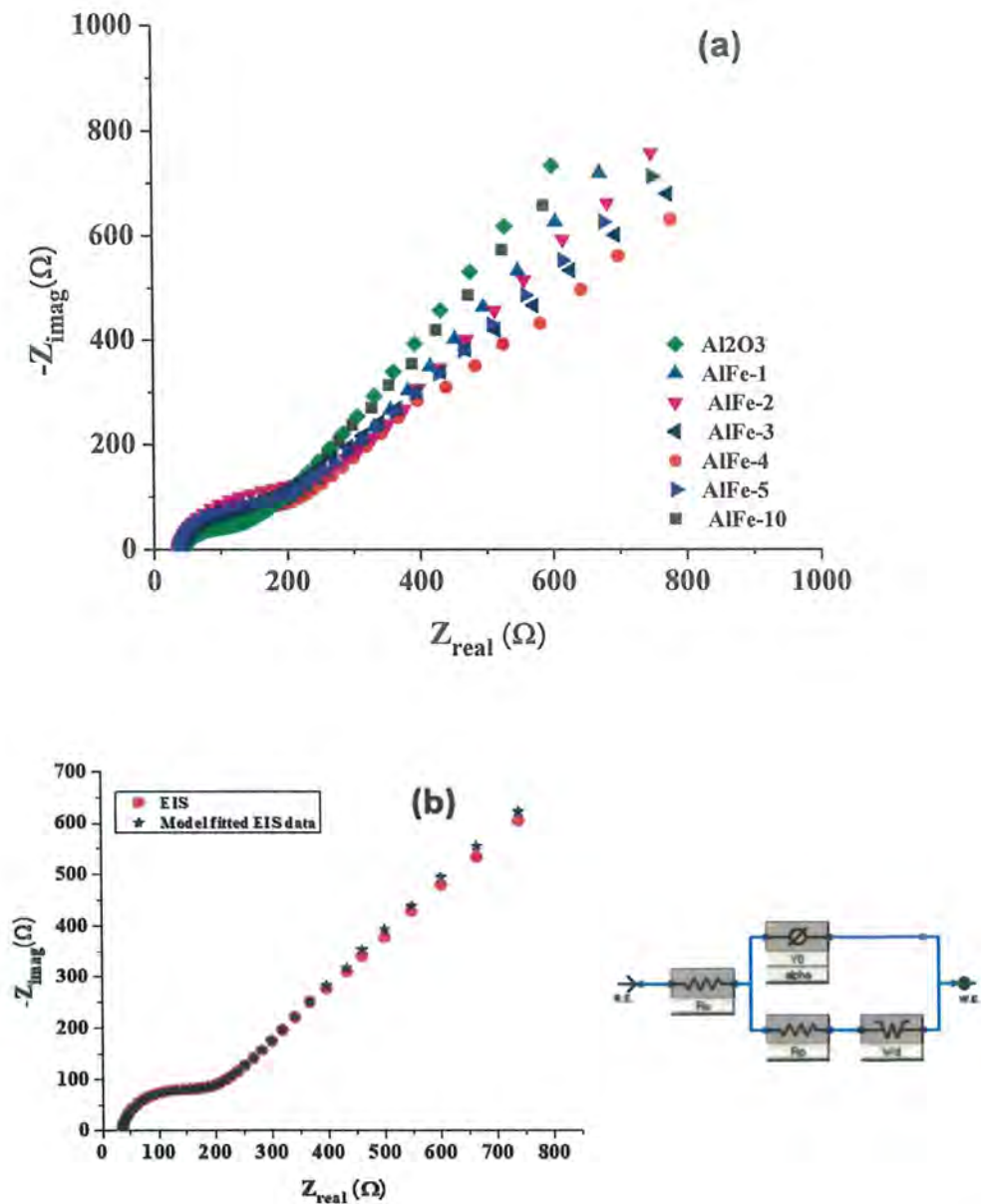


Figure 3.8. (a) EIS spectra of all compositions performed in 5 mM $K_3[Fe(CN)_6]$ and 1 M KCl solution, (b) The model fitted EIS spectra for water oxidation along its equivalent circuit model used for simulation of EIS data.

The 4% $Fe_2O_3@Al_2O_3$ modified electrode demonstrated an optimal loading of active metal oxide onto $\gamma-Al_2O_3$ due to its lowest R_{ct} value. This significant disparity in the

electrochemical behavior of the modified electrodes could be attributed to the favorable kinetics of electron transfer facilitated by well-dispersed iron oxide nanoparticles in the 4%Fe₂O₃@Al₂O₃ system compared to others. However, the R_{ct} value increased for the highest loadings of 5% and 10%Fe₂O₃@Al₂O₃, potentially due to surface deactivation caused by particle clustering.

3.2.2.1 Simulation of Nyquist plot by fitting to the equivalent circuit model

The results obtained from fitting of experimental data to the equivalent circuit model are presented in Table 3.4. The ideal relationship between the variables R_s (solution resistance) and R_w is that they relate to, respectively, the characteristics of the electrolyte solution and the diffusion of the redox probe. Therefore, no matter what changes are made to the electrode surface, these parameters are unaltered [72]. The electrode/electrolyte interface and insulating characteristics are intimately related to the constant phase element (CPE) and R_{ct} parameters. Therefore, any modification to the electrode surface will influence these variables. The CPE should be discussed instead of double layer capacitance (C_{dl}) when researching real systems because the former is more pertinent and significance in non-ideal systems.

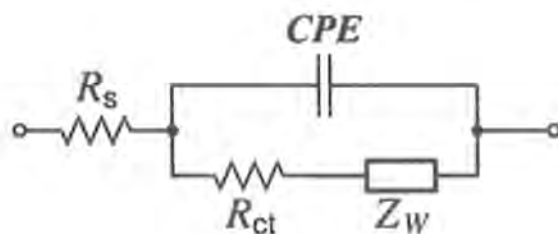


Figure 3.9. Diagram of an equivalent circuit used for fitting impedance spectroscopic data [53].

The constant phase element (CPE) comprises two constituent components, namely Q (capacitance) and surface roughness denoted by α . The α value ranges between zero, indicating resistance-dominated Q , and one, denoting an ideal capacitor with a smooth surface [73]. Consequently, it can be inferred that a smaller α value indicates a less uniform electrode surface. Thus, an increase in surface roughness and dispersion leads to a reduction in α , making the concept of double layer capacitance less applicable to an ideally smooth and uniform electrode/ solution interface. In the recent study, the α values ranged

from 0.87-0.95, suggesting that the Fe₂O₃@Al₂O₃ catalyst exhibited moderate surface roughness, which is consistent with the findings of the scanning electron microscopy (SEM) analysis. The equation used to calculate the apparent electron transfer rate constant [73], k_{app} , is as follows:

$$k_{app} = RT/F^2R_{ct}C \quad (3.1)$$

In this equation, R represents the universal gas constant (8.314 J mol⁻¹ K⁻¹), T is the absolute temperature of the system (298 K), F represents the Faraday constant (96485 C mol⁻¹), and C denotes the concentration of the molecule (in mol cm⁻³). The notably high k_{app} values and low R_{ct} values observed for the 4%Fe₂O₃@Al₂O₃ modified electrode imply a faster electron transfer process compared to the other modified electrodes.

Table 3.4. Derived data from the equivalent circuit of fitted EIS models in K₃[Fe (CN)₆].

EC Parameters	Al ₂ O ₃	AlFe-1	AlFe-2	AlFe-3	AlFe-4	AlFe-5	AlFe-10
R _s (Ω)	35	36	35	27	28	45	41
R _{ct} (Ω)	1054	117	109	97	56	92	103
CPE (μF)	10.72	2.96	4.82	1.74	1.55	3.78	4.24
α	0.973	0.959	0.974	0.895	0.928	0.943	0.943
R _w (μΩ)	382	803	517	211	115	655	377
k _{app} (10 ⁻⁴ cms ⁻¹)	0.50	4.54	4.85	5.50	9.47	5.78	5.14

3.3 Catalyst Performance for OER in Alkaline Medium

The two main purposes of this study were to explore the OER performance of catalysts and to examine the potential role of methanol as a facilitating agent in the water oxidation process. For this purpose, all the modified electrodes were tested for electrocatalytic potential toward water oxidation in an alkaline medium using 1 M KOH as an electrolyte, via various electroanalytical techniques. Various kinetic and OER parameters were studied to evaluate and compare the performance of pure and impregnated catalysts.

3.3.1 Cyclic voltammetry (CV) and linear sweep voltammetry (LSV)

Voltammetric experiments were used to analyze the performance of all synthesized materials toward water oxidation reaction in alkaline medium (1 M KOH). Within the specified potential range, an anodic peak was observed, attributed to the electrochemical oxidation of water.

3.3.1.1 Determination of current densities (*J*)

The cyclic voltammetry profile for Al₂O₃/GC in 1 M KOH at 100 mV s⁻¹ is presented in Figure 3.10 (a). A small hump was observed at 1.3 V that ascribed to the anodic peak of water oxidation (OER peak). In Figure 3.10 (b), the CV response of Al₂O₃/GC towards water oxidation in 1 M KOH + 1 M methanol is presented with an explicit OER peak at 1.33 V (vs. Ag/AgCl).

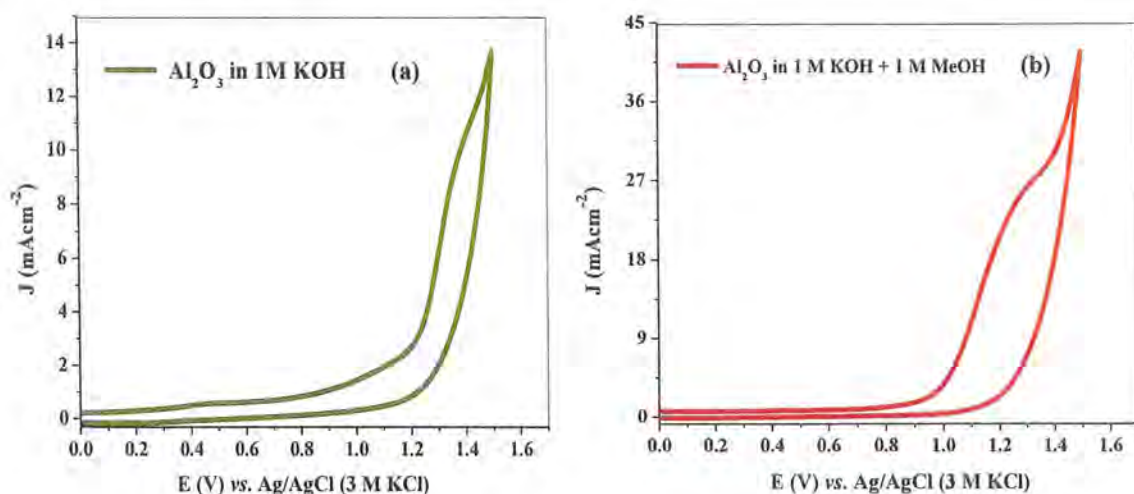


Figure 3.10. CV responses of Al₂O₃ in (a) 1 M KOH, (b) 1 M KOH + 1 M MeOH at 100 mV s⁻¹.

To differentiate the Al₂O₃/GC response in both systems, a comparison of both voltammograms is given in Figure 3.11. In the presence of methanol, significant enhancement was observed upon the addition of subsequent amounts of methanol in 1 M KOH.

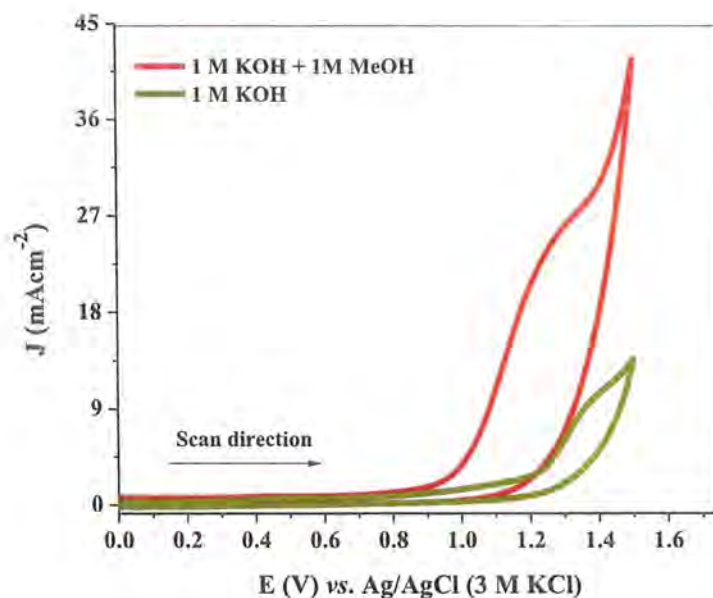


Figure 3.11. Comparative CV responses of OER in 1 M KOH and 1 M KOH + 1 M MeOH at 100 mV s^{-1} .

Current density serves as a key parameter for evaluating the performance of any catalyst. The more efficient the catalyst is, the current density will be higher. With the addition of methanol, there was a substantial rise in peak current density.

CV profiles for all the modified electrodes in 1 M KOH and 1 M KOH + 1 M MeOH are presented in Figures 3.12 and 3.13, respectively. The different peak current densities were observed for each electrode. Moreover, all prepared materials were responsive toward water electrocatalysis and exhibited promising OER performances. While, AlFe-4 modified electrode showed the highest current density, thus exhibiting a better electrocatalyst among all the compositions.

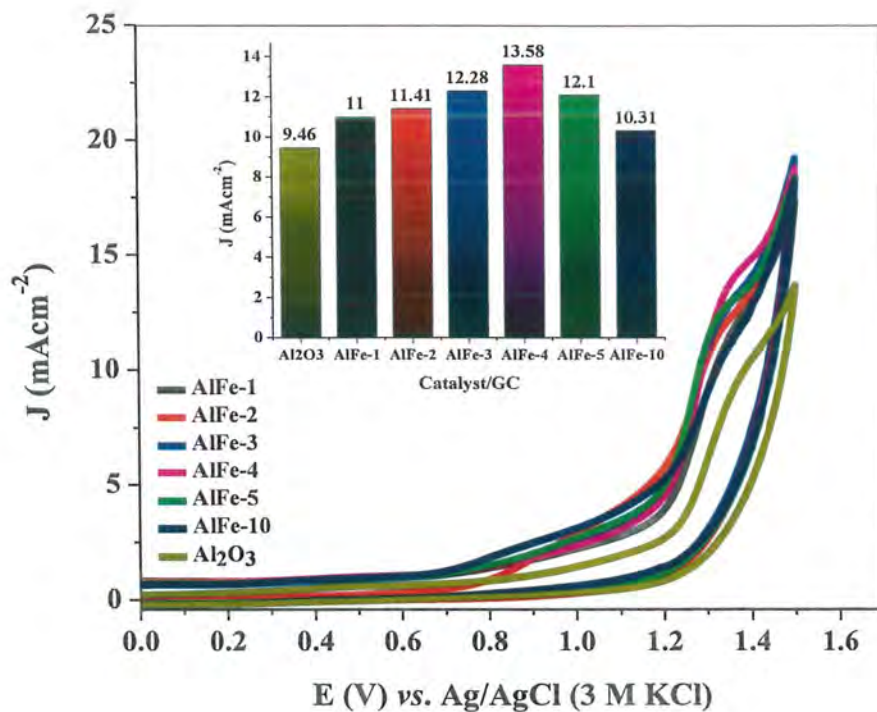


Figure 3.12. CV responses for all modified electrodes in 1 M KOH at 100 mV s⁻¹.

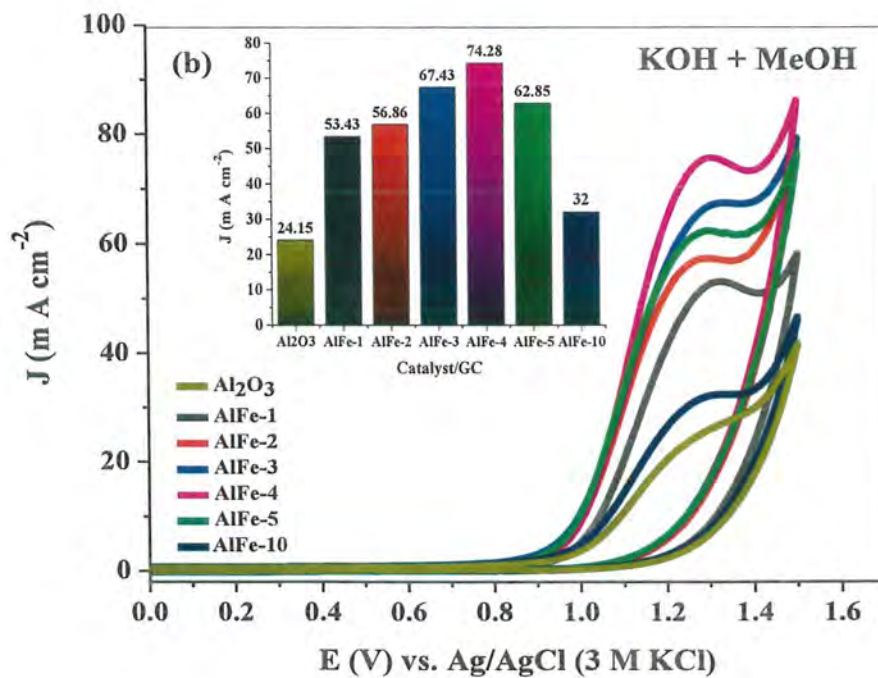


Figure 3.13. CV responses for all modified electrodes in 1 M KOH + 1 M MeOH at 100 mV s⁻¹.

The peak current densities for both systems are presented in Table 3.5 and in the form of a bar graph in Figure 3.8.

Table 3.5. Current densities of all modified electrodes from CV data.

Electrocatalysts	J (mAcm ⁻²)		ΔJ (mAcm ⁻²)
	1 M KOH	1 M KOH + 1 M Methanol	
Al ₂ O ₃	9.46	24.15	14.69
AlFe-1	11.00	53.43	42.43
AlFe-2	11.41	56.86	45.45
AlFe-3	12.28	67.43	55.15
AlFe-4	13.58	74.28	60.70
AlFe-5	12.10	62.85	50.75
AlFe-10	10.31	32.00	21.69

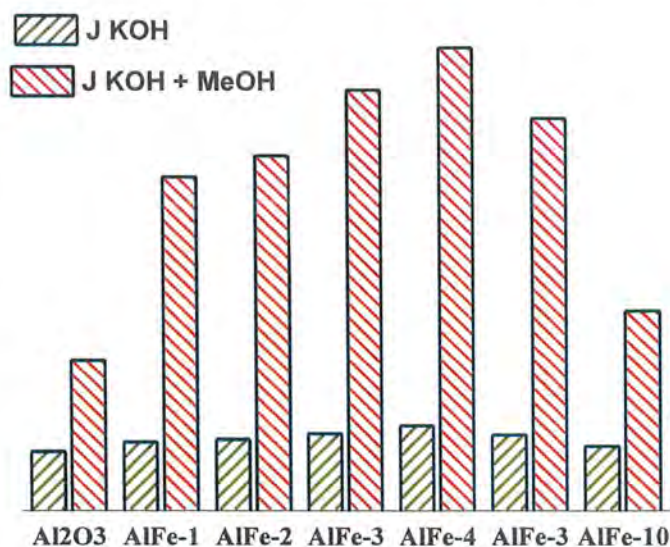


Figure 3.14. Comparison of current densities of all modified electrodes in 1 M KOH and 1M KOH + 1 M MeOH.

The substantial increase of peak current densities by a factor of 4 to 5 in the presence of methanol, as compared to KOH, can be attributed to an escalated oxidation rate

of OH^- ions to produce oxygen in OER. This interaction between OH^- and methanol, leads to the formation of salt-like MeO^-K^+ species, which facilitates the movement of OH^- ions towards the electrode surface.



Thus, more OH^- ions move towards the electrode surface, to get oxidized and an escalated production of oxygen. This increases the charge transfer kinetics of the OER process at the electrode surface, leading to an increase in current density.

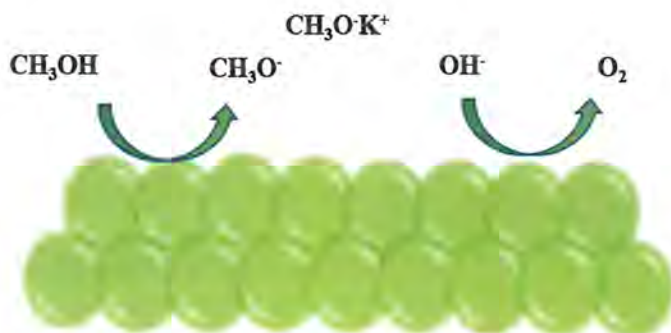


Figure 3.15. Diagrammatic representation of methanol and water oxidation processes at the electrode surface.

3.3.1.2 Determination of onset potential (E_{onset}) and overpotential (η)

The onset potential (E_{onset}) and overpotential are fundamental parameters to evaluate the catalyst behavior of all prepared materials [74]. Onset potential (E_{onset}) is the potential where the substantial process takes place and peak current begins to rise, depicted in the LSV curve of $\text{Al}_2\text{O}_3/\text{GC}$ in Figure 3.16, recorded in 1 M KOH and 1 M KOH + 1 M methanol at 100 mV s^{-1} .

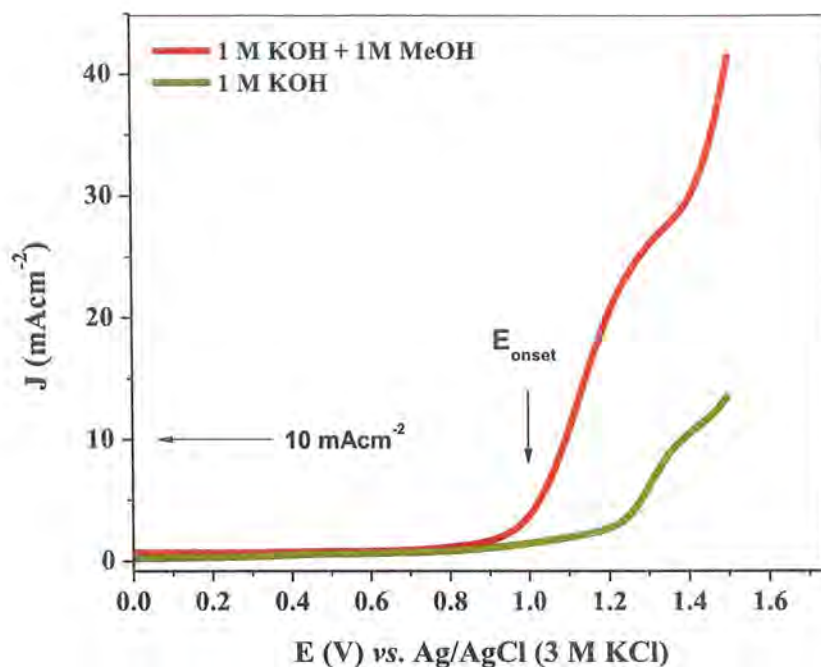


Figure 3.16. LSV curves for the OER response of Al_2O_3 in 1 M KOH and 1 M KOH + 1 M MeOH at 100 mV s^{-1} .

Overpotential refers to the variation between the applied potential and the thermodynamic potential of an electrochemical reaction ($\eta \text{ (mV)} = E - E_{\text{eq}}$). Typically, determining the exact potential value for the water oxidation process is complex. Thus, potentials corresponding to a specific current density value designated as η_{10} , are considered reliable parameters [75]. These parameters were extracted from electrochemical data and compared for water oxidation responses across all catalyst-modified GC electrodes.

Linear sweep voltammograms (LSV) for water oxidation on all electrodes were observed in 1 M KOH and compared with the voltammograms in 1 M KOH: 1 M methanol mixed solvent media, as presented in Figure 3.17. This showed a consistent trend of enhancement in current densities upon the introduction of methanol. The onset potential and overpotential values at 10 mA cm^{-2} are compiled in Table 3.6.

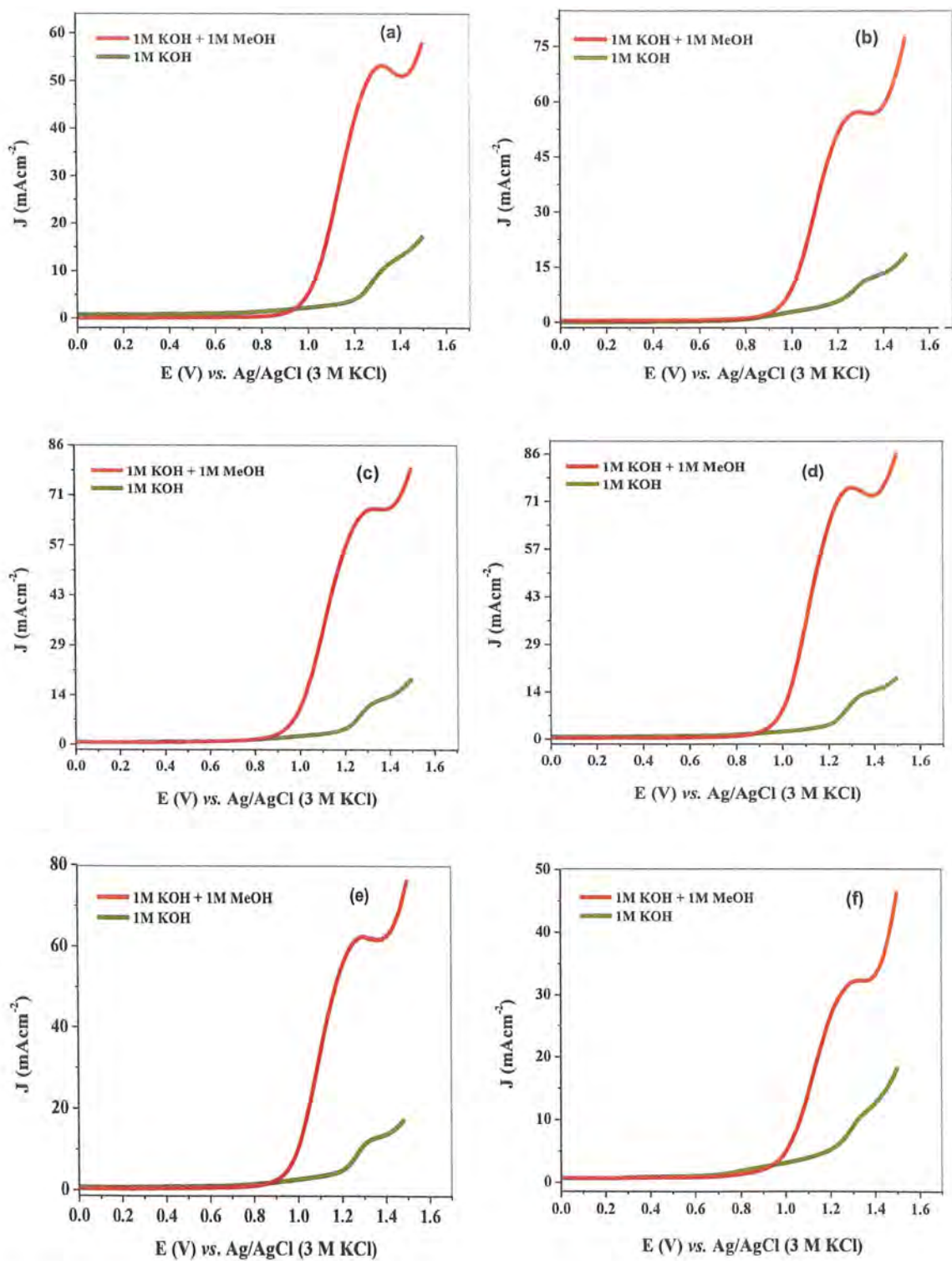


Figure 3.17. LSV scans for OER at (a) AlFe-1, (b) AlFe-2, (c) AlFe-3, (d) AlFe-4, (e) AlFe-5, and (f) AlFe-10.

Table 3.6. Estimated onset and overpotential values for all modified electrodes.

Electrocatalyst	E_{onset} (V) vs. Ag/AgCl	η_{10} (V) vs. Ag/AgCl	E_{onset} (V) vs. RHE	η_{10} (V) vs. RHE
Al ₂ O ₃	0.90	1.09	1.68	0.64
AlFe-1	0.86	1.04	1.64	0.59
AlFe-2	0.85	1.01	1.63	0.56
AlFe-3	0.83	1.01	1.61	0.56
AlFe-4	0.83	0.99	1.61	0.54
AlFe-5	0.86	1.01	1.64	0.56
AlFe-10	0.88	1.07	1.66	0.62

It is noted that OER is facilitated on all synthesized materials with the lower onset and overpotential values, thus pointing to these electro-catalysts being efficient for the water oxidation process.

3.3.1.3 Determination of diffusion and mass transport coefficients

The electroactivity of Al₂O₃ for water oxidation reaction was examined in the presence of 1 M KOH followed by subsequent addition of methanol. The response of water oxidation at Al₂O₃/GC at different sweep rates (20-100 mVs⁻¹) is presented in Figure 3.18.

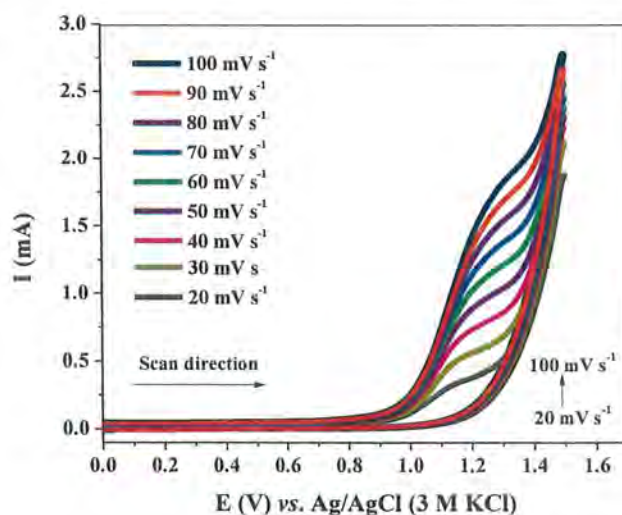


Figure 3.18. CV profiles for the OER process were observed at Al₂O₃/GC at different scan rates.

For irreversible water oxidation process, Randles-Sevcik equation was used to calculate the diffusion coefficient [76]:

$$I_p = 2.99 \times 10^5 n (\alpha n_a)^{1/2} A D_0^{1/2} C v^{1/2} \quad (1.14)$$

The transfer coefficient is determined by using following equation [76]:

$$E_{pa} - E_{pa/2} = 0.048 V / (\alpha n) \quad (3.3)$$

Where E_p represents the peak potential, $E_{p/2}$ is the peak potential corresponding to 0.5 I_p in cyclic voltammogram, α represents the transfer coefficient and n represents the number of electrons. The diffusion coefficient can be obtained from the functional relationship between peak current and square root of the scan rate. A linear functional plot for the calculation of diffusion coefficient at Al_2O_3/GC was plotted between anodic peak current I_p and $v^{1/2}$ is given in Figure 3.19.

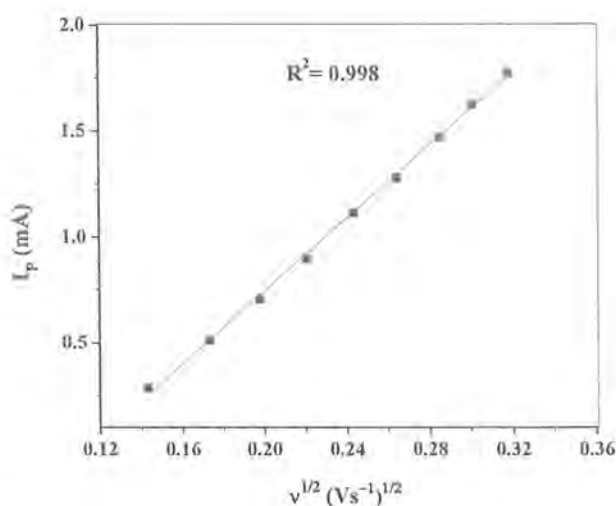


Figure 3.19. Linear functional plot for the determination of diffusion coefficient of OER at Al_2O_3/GCE .

Cyclic voltammograms for all impregnated compositions are presented in Figure 3.20, and their corresponding plots are given in Figure 3.21. All electrodes showed a similar trend of increase in peak current with the increase in scan rate thus corresponding to the facilitation of the oxidation process at the electrode-electrolyte interface.

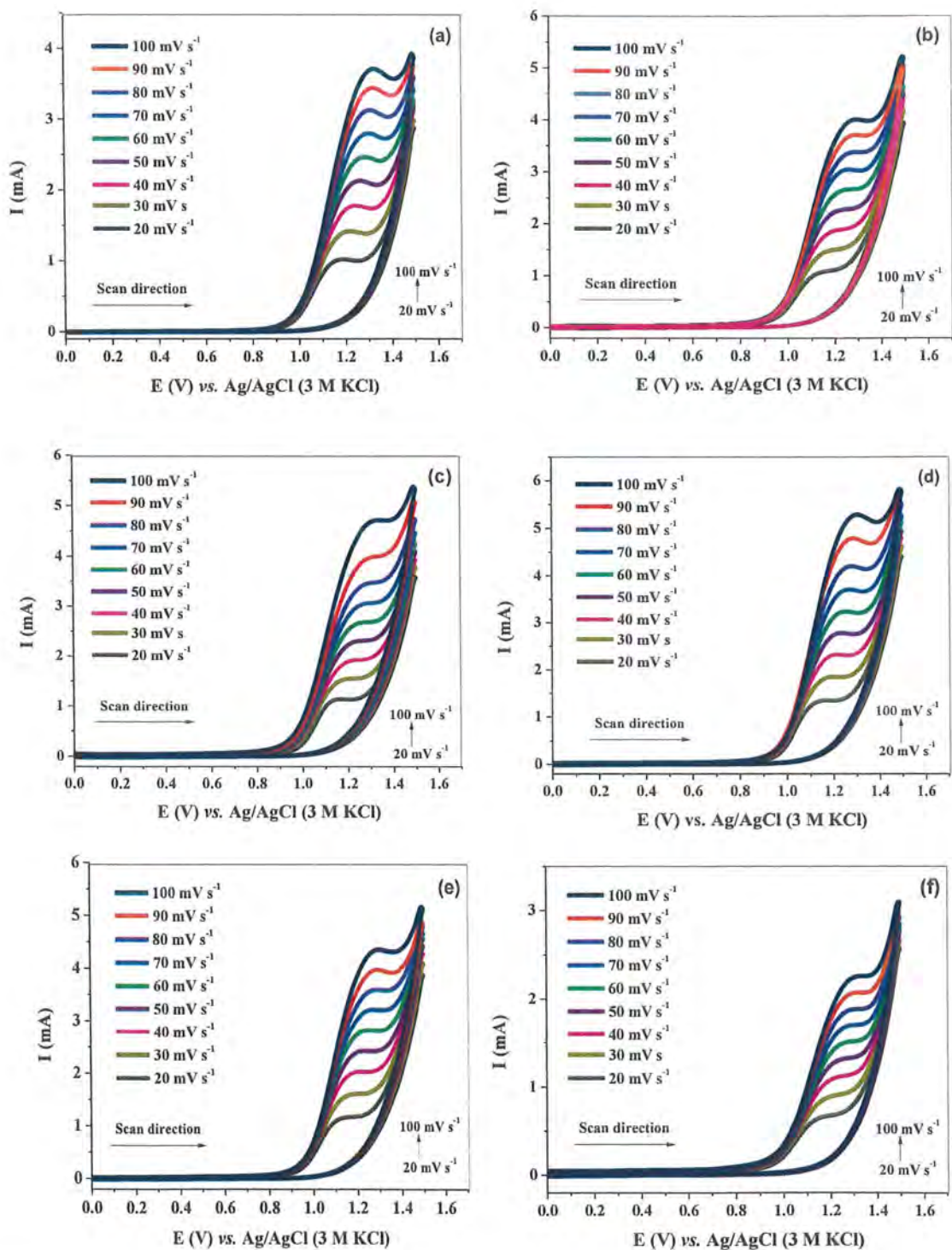


Figure 3.20. CV scans for OER at different scan rates observed for (a) AlFe-1/GC, (b) AlFe-2/GC, (c) AlFe-3/GC, (d) AlFe-4/GC, (e) AlFe-5/GC, and (f) AlFe-10/GC electrodes.

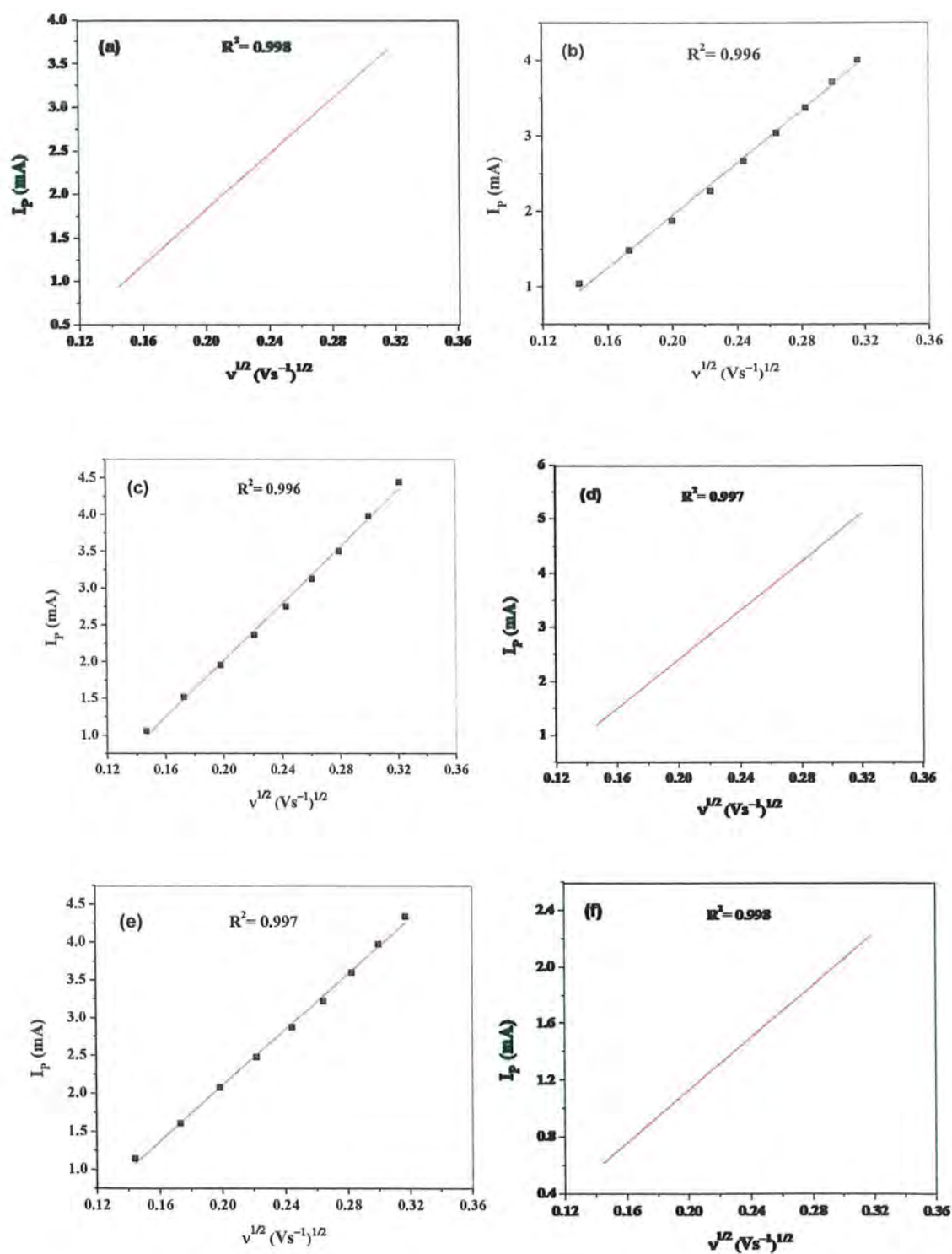


Figure 3.21. Linear functional plots for the determination of diffusion coefficients for OER at (a) AlFe-1/GC, (b) AlFe-2/GC, (c) AlFe-3/GC, (d) AlFe-4/GC, (e) AlFe-5/GC, and (f) AlFe-10/GC electrodes.

Mass transport coefficient represents the rate of mass transport towards the electrode and that includes the flux of ions and reaction intermediates, or products formed during the redox process. The mass transport coefficient is calculated by using the formula [76, 77].

$$m_T = [D_o (RT/Fv)]^{1/2} \quad (3.4)$$

Where D_o is the diffusion coefficient in cm^2s^{-1} , R is the general gas constant ($8.31 \text{ JK}^{-1}\text{mol}^{-1}$), T donates the temperature in K , F represents the Faraday's constant (96485C) and v is scan rate (Vs^{-1}). The kinetics of the redox reaction is linked to the mass transport coefficient value (m_t). If $k_o \gg m_t$ it indicates that the reaction is electrochemically reversible and if $k_o \ll m_t$ then the reaction will be irreversible. The diffusion coefficient (D_o) and mass transport coefficient values are presented in Table 3.8, which shows the criterion for irreversibility persists and $k_o \ll m_t$ is valid in the present study [76].

3.3.1.4 Kinetics of OER process and estimation of heterogeneous rate constants

The heterogeneous rate constant k_o value provides thorough details about the kinetics of the reaction [78]. Therefore, the kinetics of water oxidation reaction in terms of heterogeneous rate constant was studied by the subsequent addition of methanol from 0.25 M to 2M in 1 M KOH solution at a scan rate of 100 mV s^{-1} . The effect of the addition of methanol concentrations on OER at $\text{Al}_2\text{O}_3/\text{GC}$ is presented in Figure 3.22.

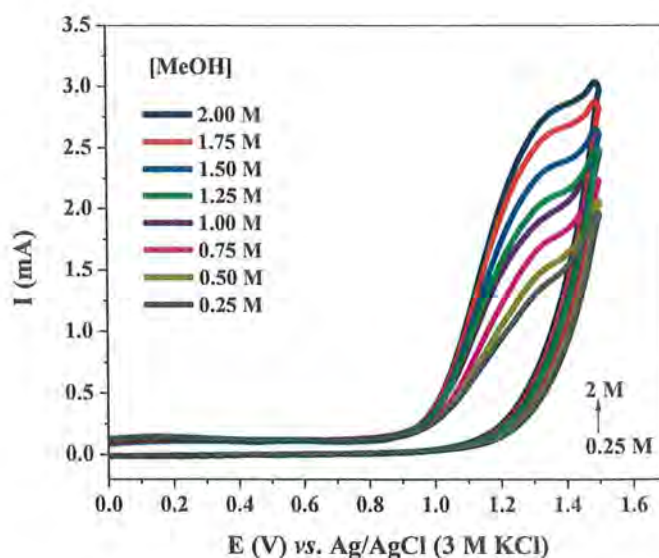


Figure 3.22. CV profiles for the OER process were observed at $\text{Al}_2\text{O}_3/\text{GC}$ in different methanol concentrations.

The increase in the concentration of methanol corresponds to the generation of MeO^-K^+ species due to the greater availability of hydroxyl ions which facilitates the rate of OER. The heterogeneous rate constant for the synthesized electrocatalyst was calculated by using the Reinmuth equation, which is given below [76]:

$$I_p = 0.227 n F k_o C \quad (3.5)$$

In the given equation, n represents the no. of electrons involved, F shows the Faraday's constant, I_p is anodic peak current, A donates the area of the working electrode, and C is the concentration of analyte. The heterogeneous rate constant can be assessed from the linear plot of peak current vs. different concentration of methanol. A linear plot for $\text{Al}_2\text{O}_3/\text{GC}$ electrode was given in Figure 3.23.

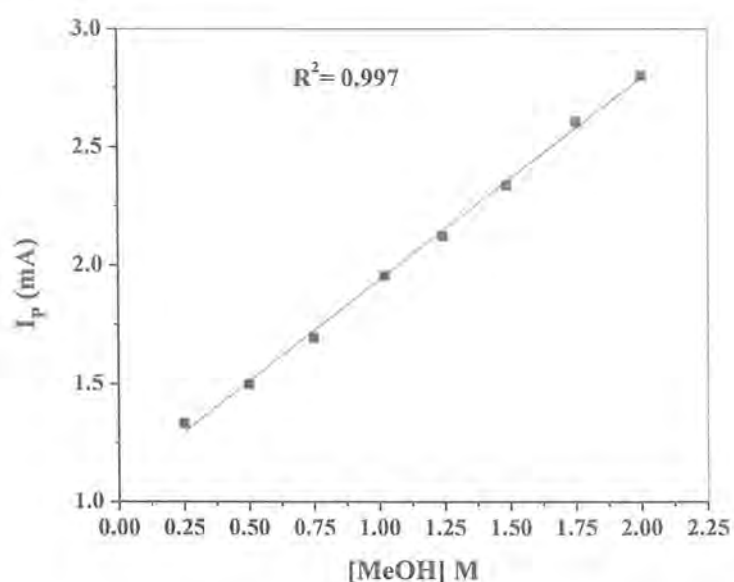


Figure 3.23. Linear functional plot for the determination of the heterogeneous rate constant of OER at $\text{Al}_2\text{O}_3/\text{GCE}$.

The effect of methanol concentration on all other modified electrodes is presented in Figure 3.24, and their corresponding linear functional plots are given in Figure 3.25.

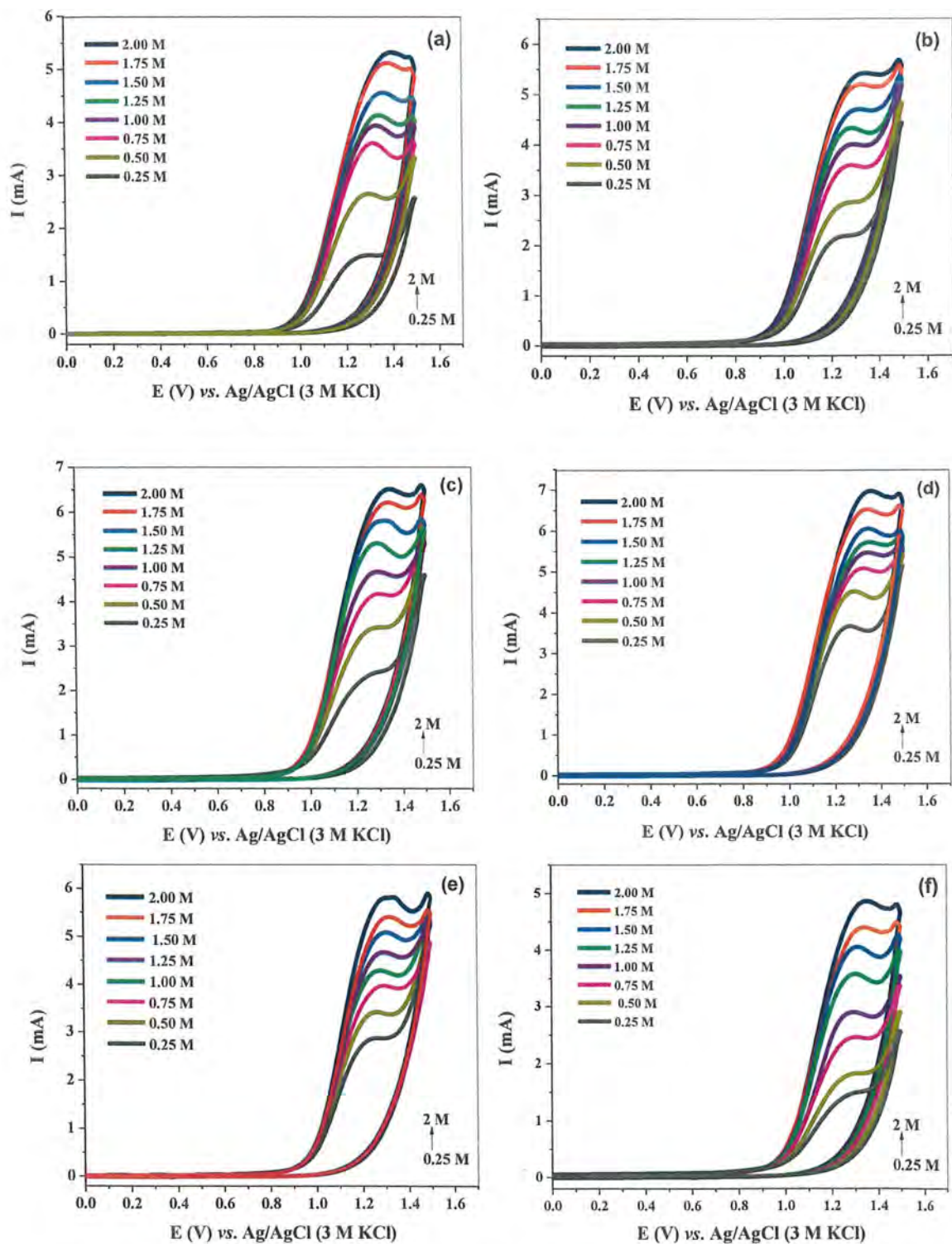


Figure 3.24. CV scans for OER in different methanol concentration for (a) AlFe-1/GC, (b) AlFe-2/GC, (c) AlFe-3/GC, (d) AlFe-4/GC, (e) AlFe-5/GC, and (f) AlFe-10/GC electrodes.

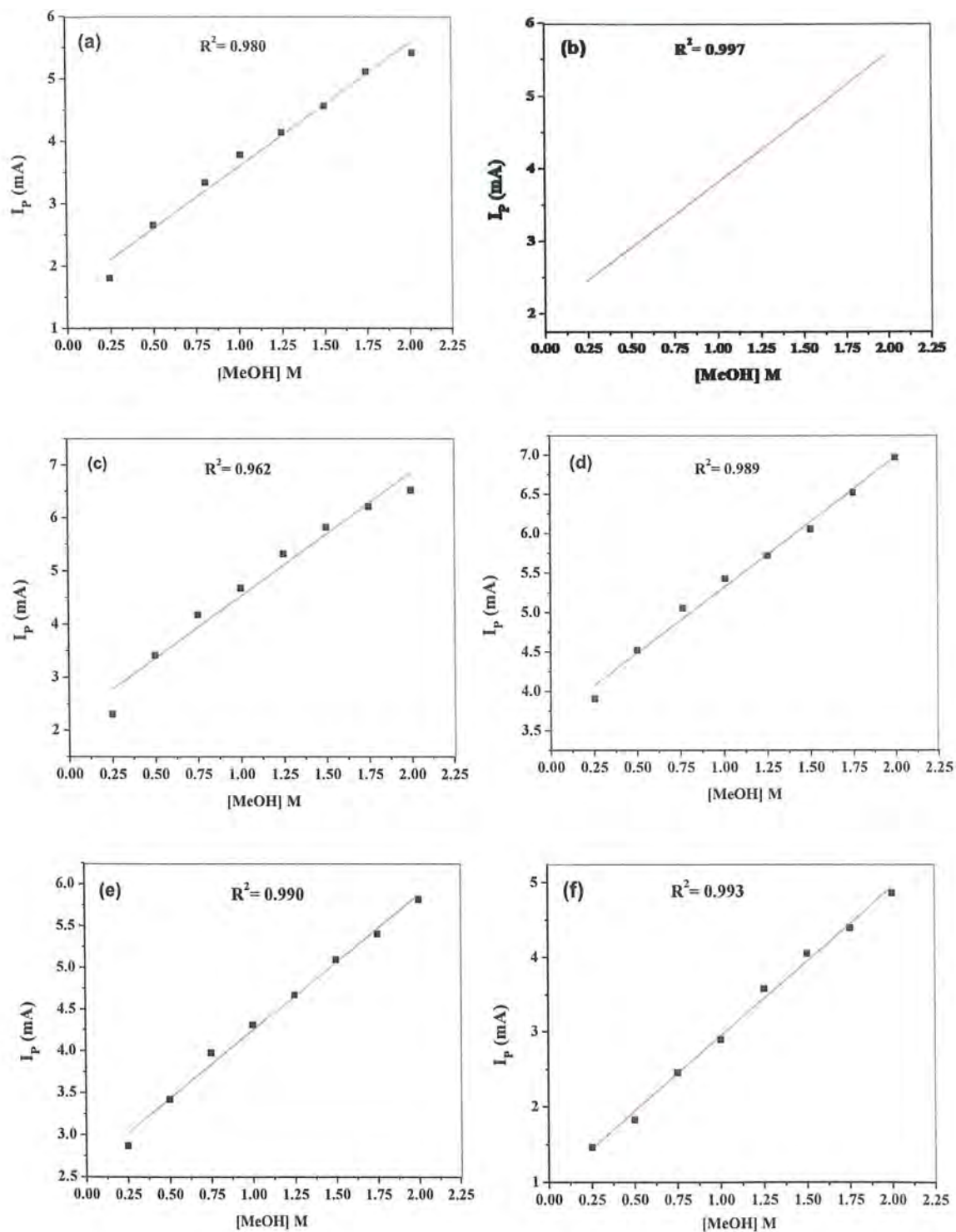


Figure 3.25. Linear functional plots for the determination of heterogeneous rate constants for OER at (a) AlFe-1/GC, (b) AlFe-2/GC, (c) AlFe-3/GC, (d) AlFe-4/GC, (e) AlFe-5/GC, and (f) AlFe-10/GC electrodes.

The estimated k_o values for all electrodes are presented in Table 3.7 and varied between 2.6 to 7.0 cm s^{-1} . The AlFe-4 catalyst exhibited the highest heterogeneous rate constant for OER catalysis among the samples. The irreversibility of the oxygen evolution reaction was deduced from the relationship $m_t > k_o$ [76].

Table 3.7. Estimated kinetics parameters for water oxidation of all synthesized samples.

Electrocatalysts	D_o $10^{-8}(\text{cm}^2\text{s}^{-1})$	m_t $10^{-4}(\text{cms}^{-1})$	k_o $10^{-3}(\text{cms}^{-1})$
Al_2O_3	0.9	2.0	2.6
AlFe-1	6.3	5.0	5.1
AlFe-2	7.3	5.3	5.3
AlFe-3	9.0	6.0	6.3
AlFe-4	11.4	6.7	7.0
AlFe-5	8.7	5.8	5.7
AlFe-10	2.4	3.0	4.3

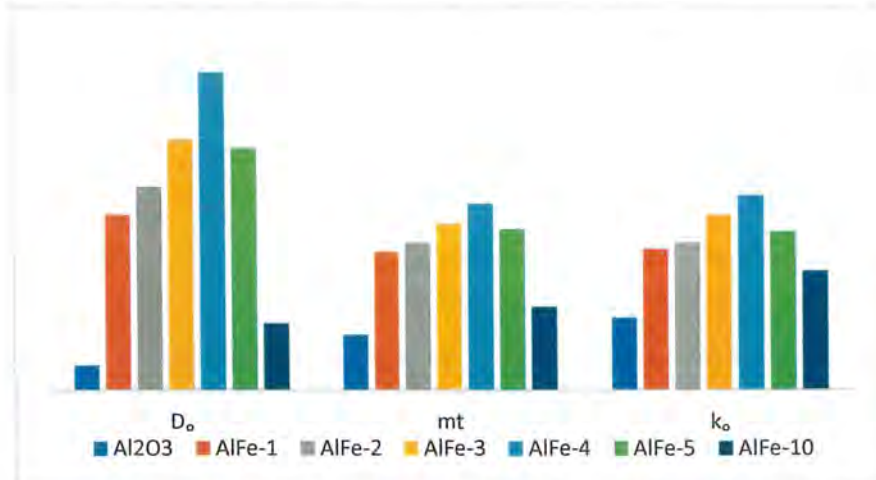


Figure 3.26. Bar chart for the comparison of different kinetic parameters of the OER process at all modified electrodes.

3.3.2 Double layer capacitance and ECSA

Double layer capacitance is the measure of catalytic activity of catalyst that can be checked by the double layer form at electrode-electrolyte interface. To determine the double layer

capacitance C_{dl} , the cyclic voltammetry performed in non-Faradic region at different scan rates (20 – 120 mV s^{-1}). Cyclic voltammograms for $\text{Al}_2\text{O}_3/\text{GCE}$ in the non-Faradic region is presented in Figure 3.27 (a). Double layer capacitance was calculated using a linear functional plot between scan rate vs difference of current densities ($\Delta I = I_a - I_c$) for Al_2O_3 presented in Figure 3.27 (b).

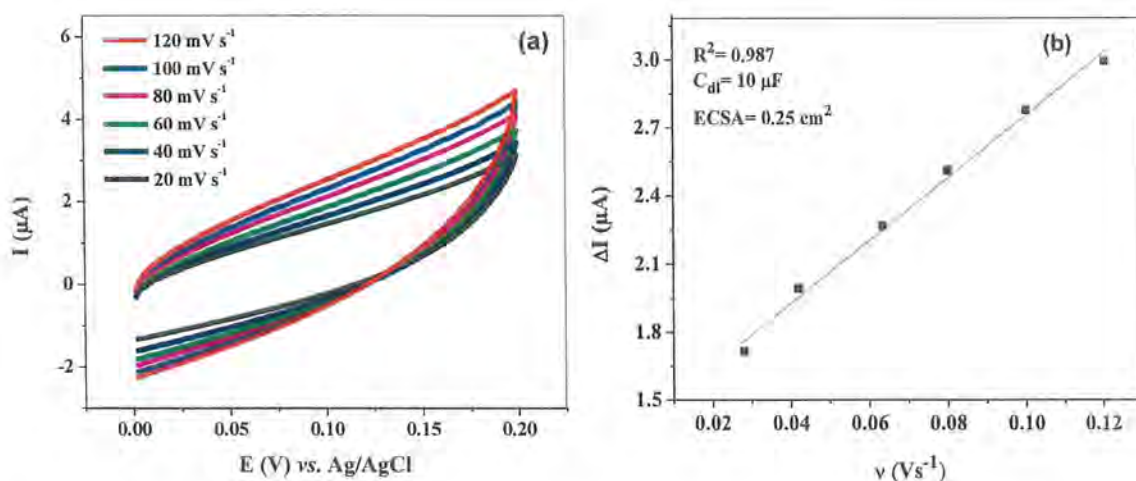


Figure 3.27. (a) CV responses of $\text{Al}_2\text{O}_3/\text{GC}$ in non-Faradic region, (b) Plot of difference of current vs scan rate for the calculation of C_{dl} value for Al_2O_3

Electrochemically active surface area (ECSA) is determined from C_{dl} using the following equation.

$$\text{ECSA} = C_{dl} / C_{sp} \quad (3.6)$$

Where C_{dl} is the double layer capacitance and C_{sp} is the general specific capacitance for metal oxide electrodes in alkaline solution (0.040 mFcm^{-2}). Greater active surface area corresponds to enhanced electrocatalytic activity. The roughness factor is another key parameter to check the catalytic activity. It is obtained by dividing the ECSA by the geometric area of the electrode [70]. Cyclic voltammograms in non-Faradic region were performed for all other modified electrodes presented in Figure 3.28, and their corresponding linear plots are presented in Figure 3.29.

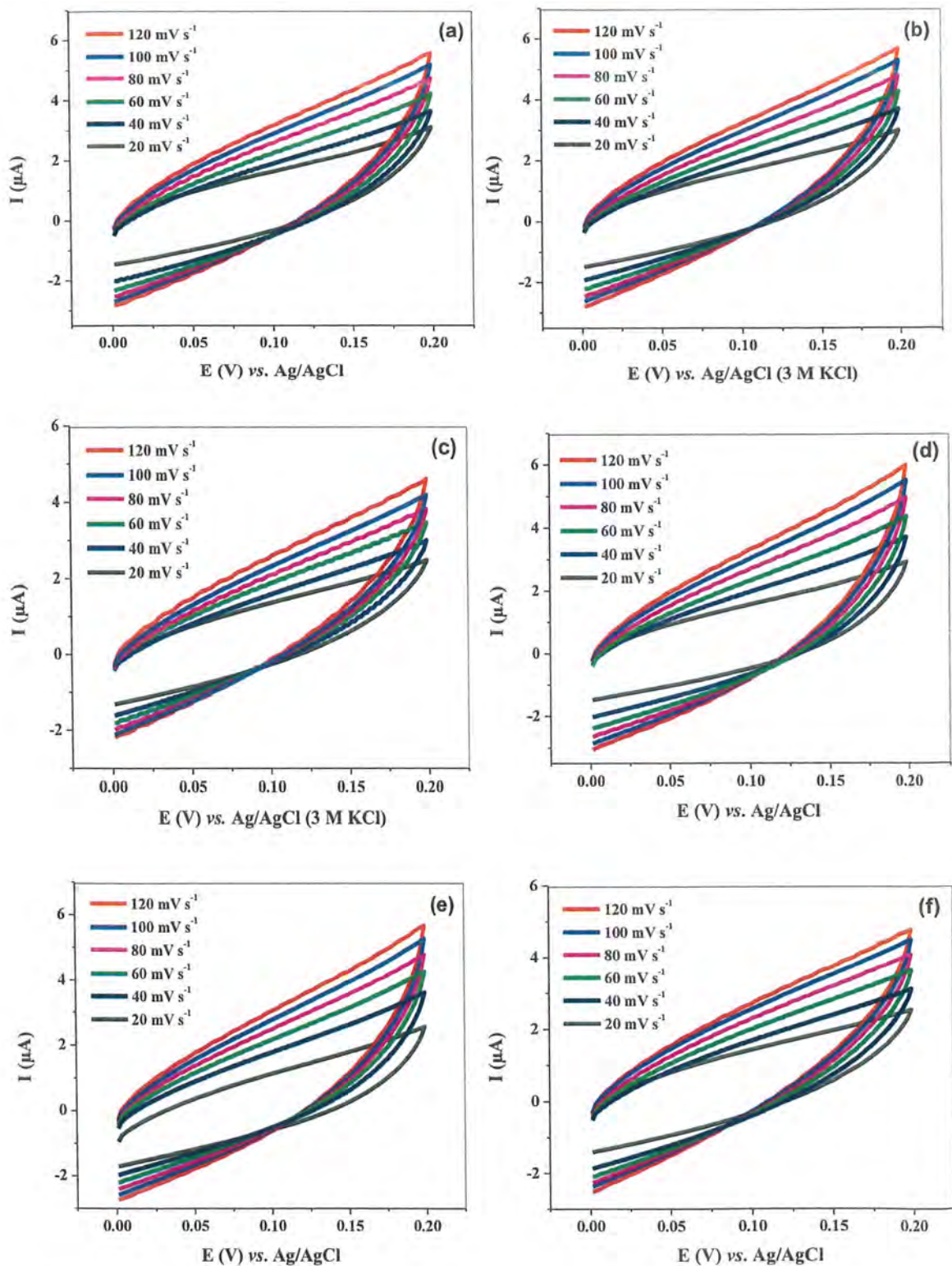


Figure 3.28. CV responses in non-Faradic region at different scan rates for (a) AlFe-1, (b) AlFe-2, (c) AlFe-3, (d) AlFe-4, (e) AlFe-5, and (f) AlFe-10.

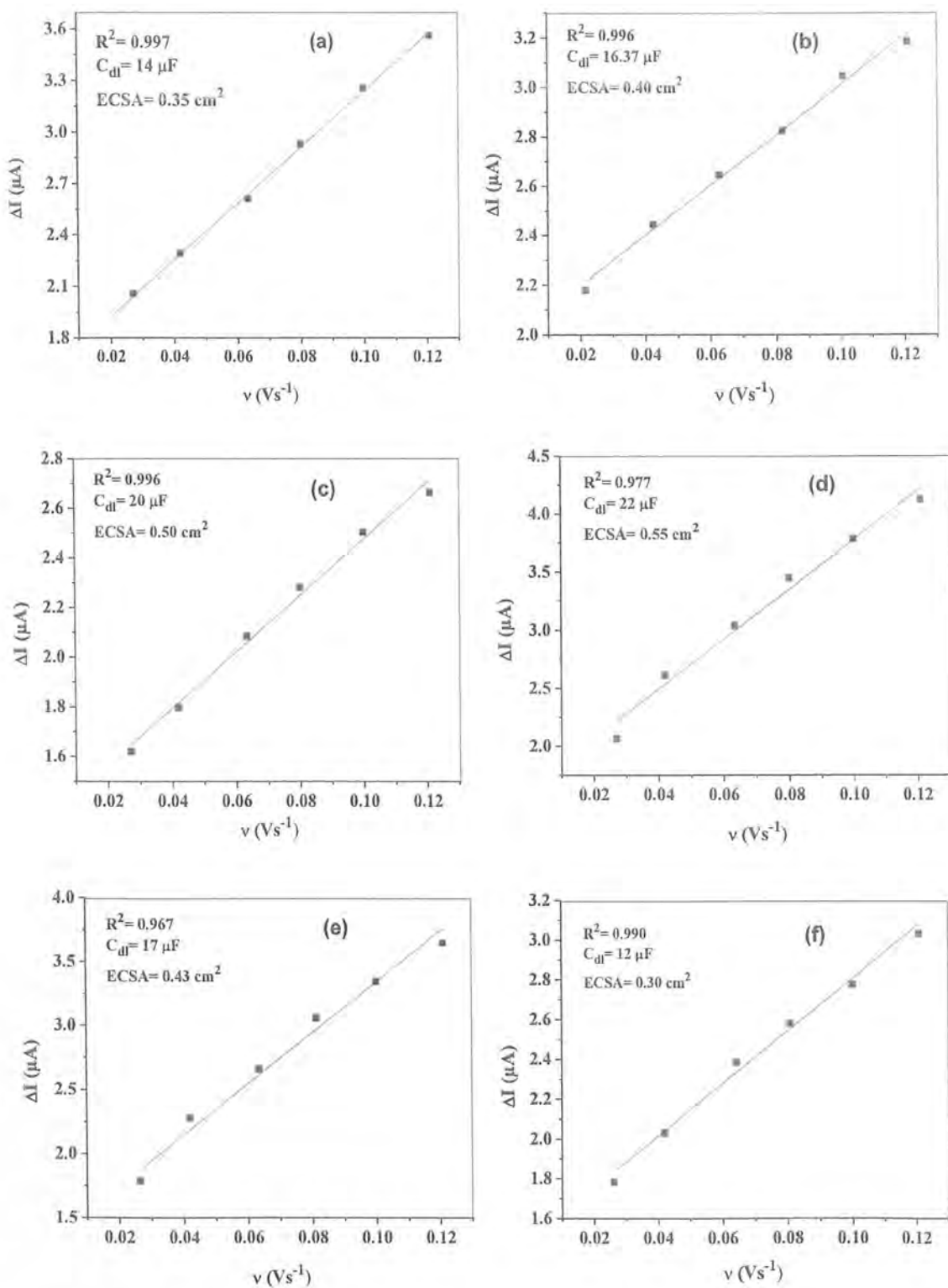


Figure 3.29. Linear functional plots for the calculation of C_{dl} for (a) AlFe-1, (b) AlFe-2, (c) AlFe-3, (d) AlFe-4, (e) AlFe-5, and (f) AlFe-10.

Table 3.8. OER parameters (C_{dl} , ECSA, and RF) for all compositions.

Electrocatalyst	C_{dl} (μF)	ECSA (cm^2)	RF
Al_2O_3	10	0.25	3.58
AlFe-1	14	0.35	5.00
AlFe-2	16	0.41	5.85
AlFe-3	20	0.50	7.14
AlFe-4	22	0.55	7.86
AlFe-5	17	0.43	6.08
AlFe-10	12	0.30	4.29

3.3.3 Tafel slopes

Tafel slope is the basic parameter for gaining insights into the mechanism and kinetics of redox reaction taking place electrochemically. By calculating the Tafel slope, it is easy to determine the overpotential that is required for current responses in OER and the catalytic efficiency of synthesized materials [79]. Tafel equation is given as [75]:

$$\eta = a + b \log (J/J_0) \quad (3.7)$$

Here b represents the Tafel slope in $mVdec^{-1}$, J is the current density in Acm^{-2} , and J_0 shows the exchange current density in Acm^{-2} . Tafel plots for water oxidation reaction observed for all compositions in 1 M KOH and 1 M KOH + 1 M methanol are presented in Figure 3.30 and 3.31, respectively and their associated Tafel slopes are gathered in Table 3.9.

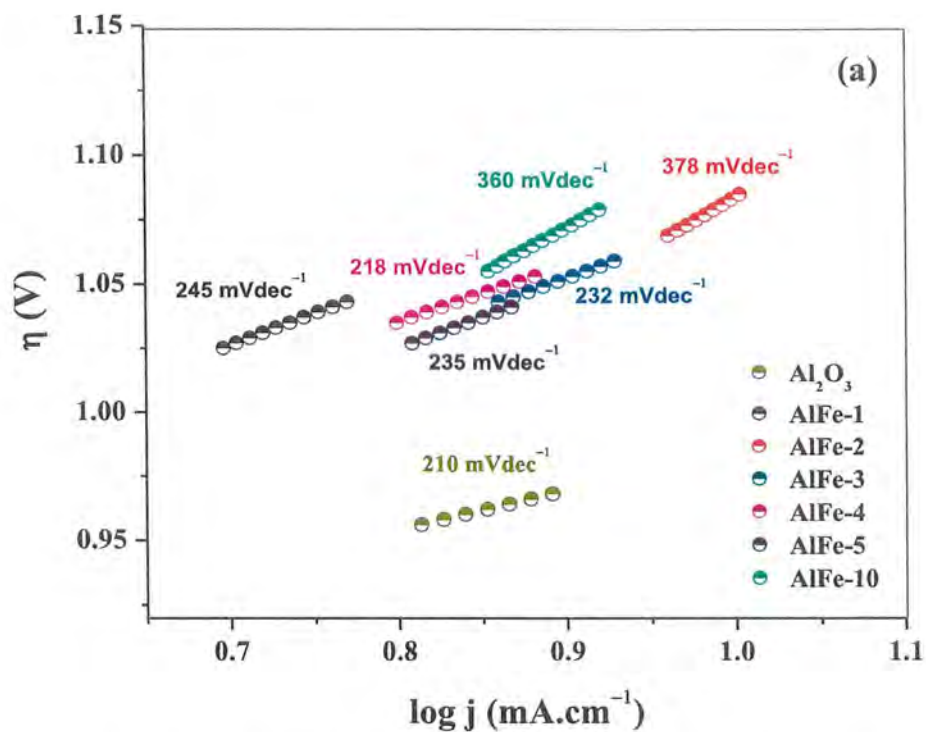


Figure 3.30. Tafel slopes for all compositions in 1 M KOH.

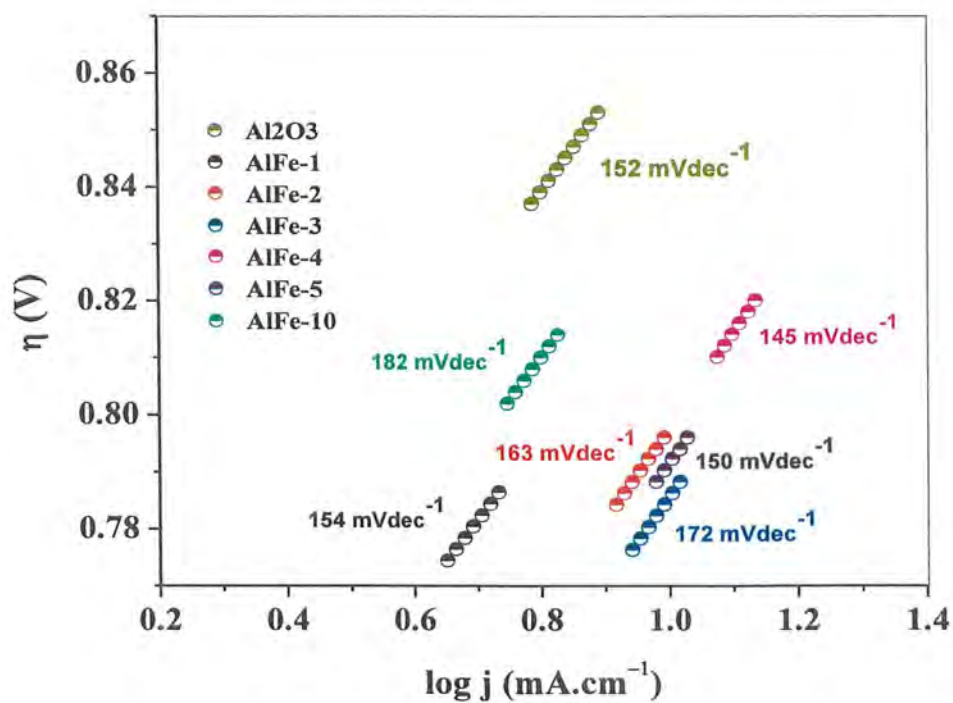


Figure 3.31. Tafel slopes for all compositions in 1 M KOH + 1 M methanol.

The low value of Tafel slopes in 1 M KOH which was further decreased by the addition of methanol, indicates alleviated kinetics overpotential deficits, this could be accredited to the increased bond strength for OH⁻ adsorption on the catalyst, which accelerates the rate of the first electron reaction step and, accordingly, improves electrocatalytic kinetics. On the other hand, the variation in Tafel slopes can reflect the concentration of active sites and their contribution. The increase in both active sites and their contribution may constitute the second reason for the observed reduction Tafel slope.

Table 3.9. Estimated Tafel slopes for all catalysts in 1 M KOH and 1 M KOH + 1 M MeOH.

Electrocatalysts	Tafel slopes, b (mVdec ⁻¹)	
	1 M KOH	1 M KOH + 1 M Methanol
Al ₂ O ₃	210	152
AlFe-1	245	154
AlFe-2	378	163
AlFe-3	232	172
AlFe-4	218	145
AlFe-5	235	150
AlFe-10	360	182

3.3.4 EIS and charge transfer resistance

To better understand the charge transfer kinetics of OER process in 1 M KOH and 1 M KOH + 1 M methanol, electrochemical impedance spectroscopy was performed. Nyquist plot for Al₂O₃/GC in 1 M KOH is presented in Figure 3.32. This Nyquist plot exhibit two distinct regions: (i) A semicircle observed in the high- frequency range, which corresponds to the process, where electron-transfer is limited. The diameter of this semicircle is equivalent to the electron transfer resistance (R_{ct}), a pivotal parameter that relates to the kinetics of the redox probe at the electrode interface; (ii) An inclined section observed at lower frequencies that corresponds to the diffusion process. This part defines the Warburg

resistance (R_w), which is associated with the semi-infinite diffusion of redox species towards the modified electrode. In the Nyquist plot, ohmic electrolyte resistance or solution resistance (R_s) is also ascribed as a resistance offered by the charge transfer process. To quantify the results of EIS, a simulation of obtained data was obtained using an equivalent circuit model. To enhance the fitting accuracy of the EIS data, a constant phase element (CPE) was integrated, replacing the real capacitor. CPE element comprises of two sub-elements: α and Q . Q represents the capacitive behavior in the absence of frequency dispersion and α is the exponent ($1 \geq \alpha \geq 0$); for an ideal capacitor $\alpha = 1$ [80].

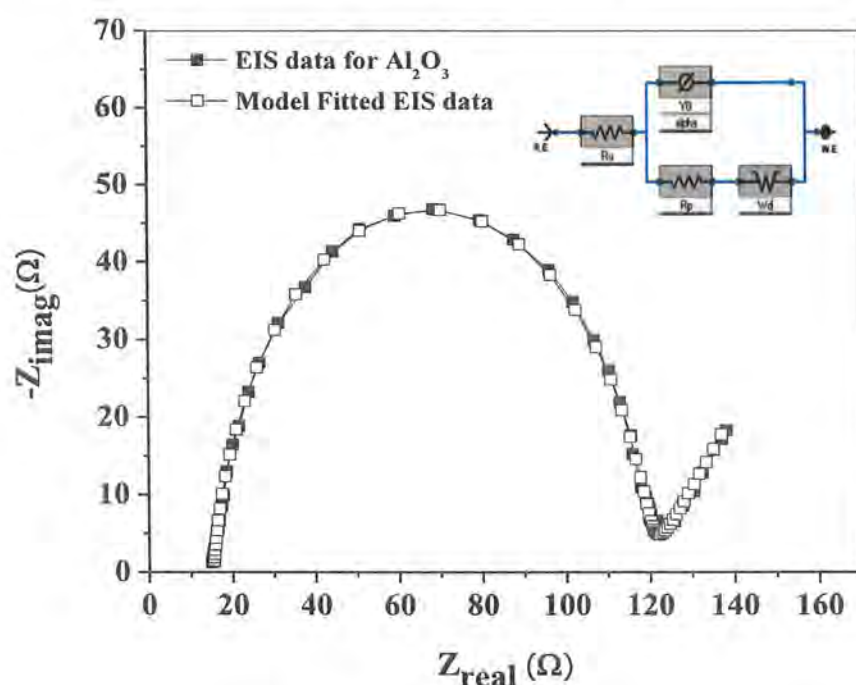


Figure 3.32. The model fitted EIS spectra of $\text{Al}_2\text{O}_3/\text{GC}$ for water oxidation in 1 M KOH, along its equivalent circuit model used for simulation of EIS data.

Nyquist plots for $\text{Al}_2\text{O}_3/\text{GC}$ in 1 M KOH + 1 M methanol is presented in Figure 3.33, along its equivalent circuit model that is used for simulating the data. The determined EIS parameters are presented in Table 3.10. The Nyquist plot represents a complete semicircle at high frequency region, indicating the charge transfer process, while an incomplete semicircle appears in low-frequency region which is related to adsorption processes.

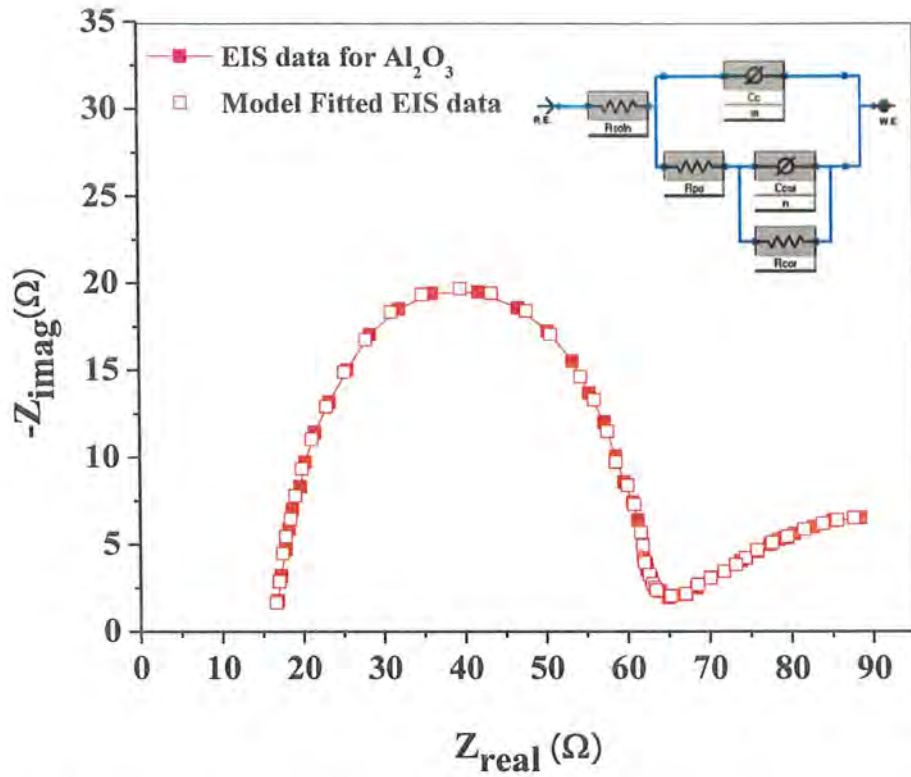


Figure 3.33. The model fitted EIS spectra of $\text{Al}_2\text{O}_3/\text{GC}$ for water oxidation in 1 M KOH + 1 M MeOH, along its equivalent circuit model used for simulation of EIS data.

The comparison of Nyquist plots in 1 M KOH and 1 M KOH + 1 M methanol for all impregnated compositions $\text{Fe}_2\text{O}_3@/\text{Al}_2\text{O}_3$ are presented in Figure 3.34. The data evaluated from fitting of EIS spectra are presented in Table 3.8.

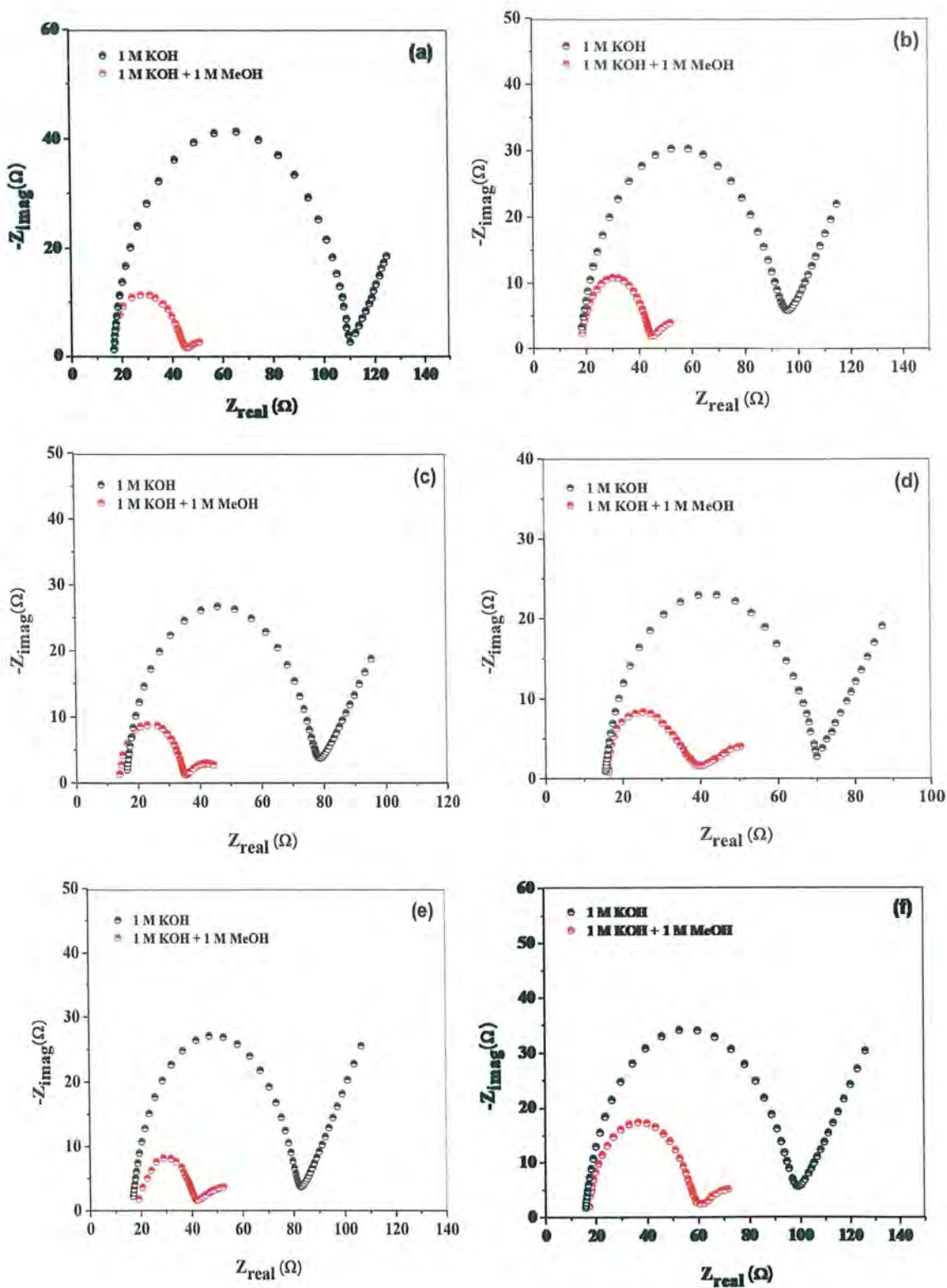


Figure 3.34. Comparison of Nyquist plots in 1 M KOH and 1 M KOH + 1 M methanol for OER at (a) AlFe-1, (b) AlFe-2, (c) AlFe-3, (d) AlFe-4, (e) AlFe-5, and (f) AlFe-10.

Table 3.10. EIS parameters extracted from simulated EIS data.

EC Parameters		Al ₂ O ₃	AlFe-1	AlFe-2	AlFe-3	AlFe-4	AlFe-5	AlFe-10
1 M KOH	R _s (Ω)	15.38	18.39	17.58	16.08	15.41	16.50	15.44
	R _{CT} (Ω)	104	92.04	75.55	60.62	53.12	64.58	80.59
	CPE (μF)	2.61	1.50	2.41	2.35	3.16	3.06	3.62
	A	0.930	0.921	0.857	0.915	0.905	0.884	0.892
	R _w (mΩ)	25.34	15.39	10.27	18.96	21.05	22.04	16.54
1 M KOH + 1 M Methanol	R _s (Ω)	18.51	15.32	17.82	13.64	16.80	18.20	19.34
	R _{CT1} (Ω)	46.36	30.34	25.43	20.73	19.70	21.92	40.00
	CPE ₁ (μF)	1.60	1.09	2.65	1.14	1.61	3.09	1.95
	α ₁	0.904	0.836	0.909	0.915	0.938	0.803	0.893
	R _{CT2} (Ω)	31.70	24.13	25.74	19.75	15.77	27.70	39.62
	CPE ₂ (mF)	32.02	24.72	25.09	22.94	23.01	29.87	33.81
	α ₂	0.419	0.377	0.417	0.459	0.315	0.329	0.295

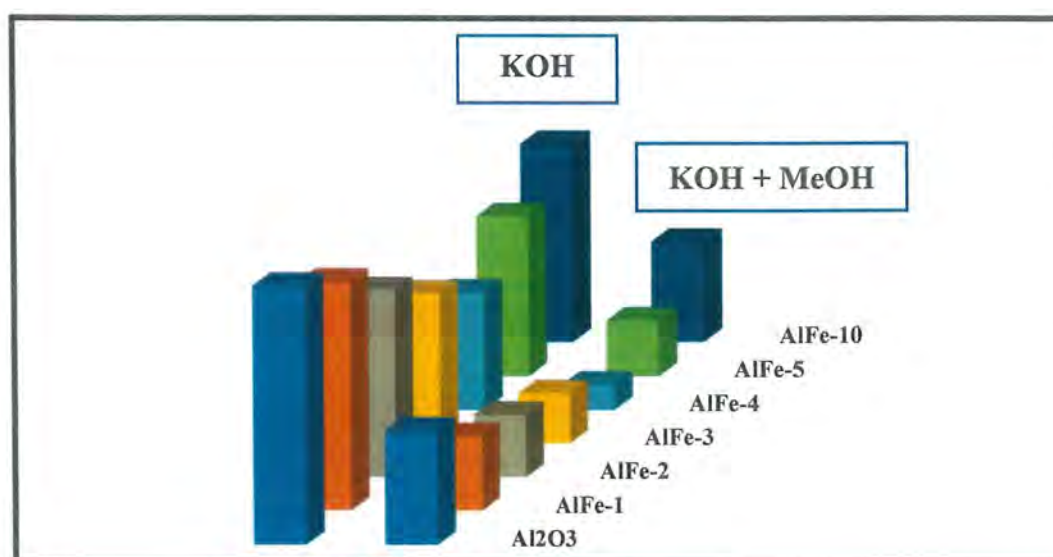


Figure 3.35. Comparison of R_{ct} values in 1 M KOH and 1 M KOH + 1 M MeOH for all compositions.

3.3.5 Chronoamperometry

The technique is used to determine the stability of synthesized catalyst using the chronoamperometry technique, also known as time-dependent technique. In this technique, the square wave potential given to the working electrode [81]. The chronoamperometry scan for AlFe-4/GC in 1 M KOH and 1 M KOH + 1 M Methanol at the overpotential value is presented in Figure 3.36.

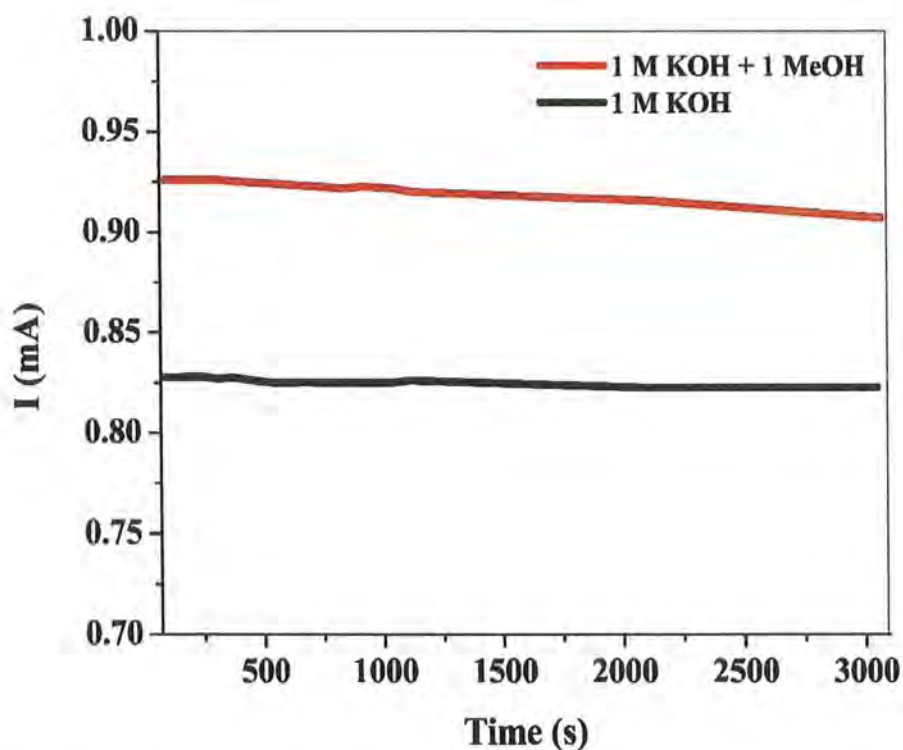


Fig. 3.36. Chronoamperometric stability test performed for AlFe-4/GC electrode in 1 M KOH and 1 M KOH + 1 M MeOH.

LSV was performed for AlFe-4 in both systems before and after chronoamperometry test and presented in Figure 3.37. A slight increase was observed in current density after the chronoamperometric scan.

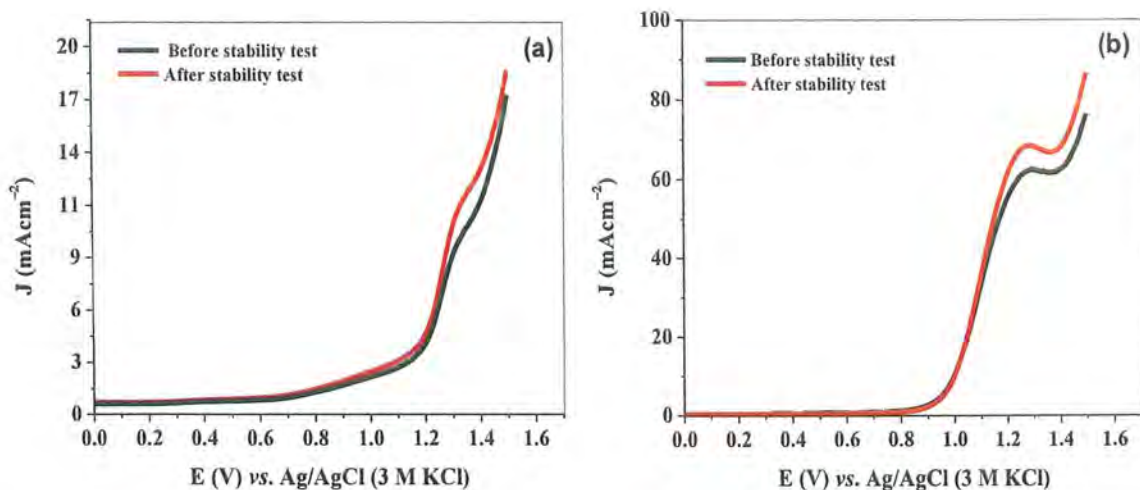


Figure 3.37. LSV Curves before and after chronoamperometric test for AlFe-4/GC in (a) 1 M KOH and (b) $1 \text{ M KOH} + 1 \text{ M MeOH}$.

A chronoamperometric test was carried out for all prepared electrodes in 1 M KOH and $1 \text{ M KOH} + 1 \text{ M MeOH}$ systems for 3600 s and results are presented in Figure 3.38 and 3.39, respectively.

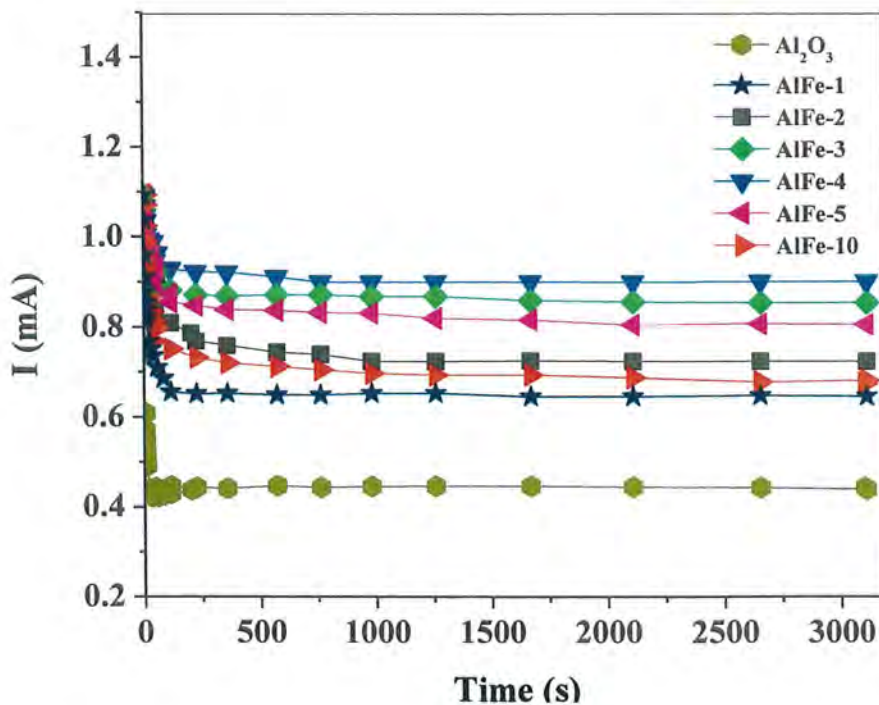


Figure 3.38. Chronoamperometry performed for all compositions in 1 M KOH .

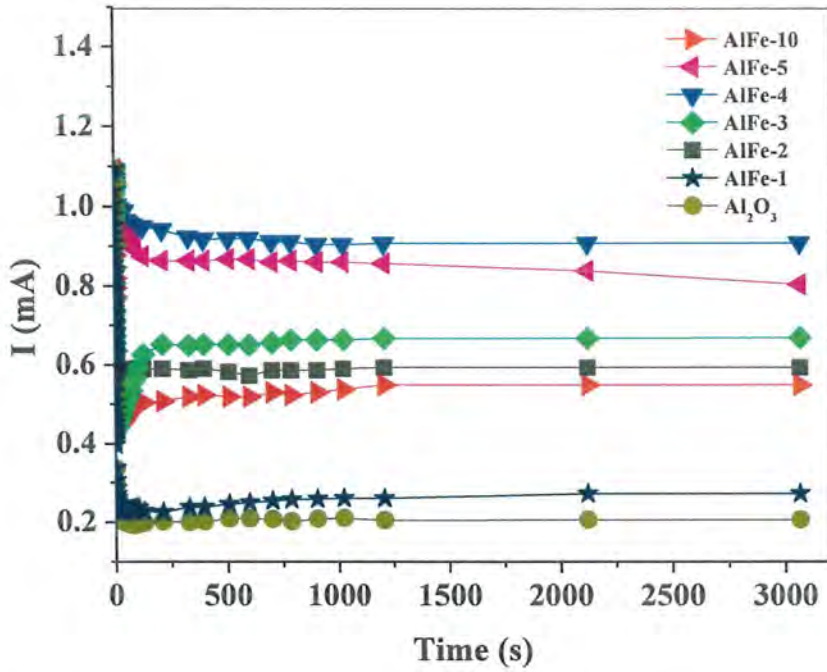


Figure 3.39. Chronoamperometry performed for all compositions in 1 M KOH + 1 M MeOH.

All modified electrodes showed good stability in chronoamperometric tests for 3600 seconds with no fluctuation in current density throughout the chronoamperometric scans in both the KOH and KOH + MeOH media. This observation points to the fact that the envisioned catalysts are better probes for OER process in the alkaline medium.

Conclusions

Pure alumina and different compositions of 1, 2, 3, 4, 5, and 10%Fe₂O₃@Al₂O₃ were successfully synthesized *via* facile precipitation and impregnation method, respectively.

All the synthesized materials were then characterized by using XRD, FTIR, SEM, and EDX for surface and structural analysis. XRD analysis inferred the average crystallize of catalysts in the range of 11 to 32 nm. FT-IR analysis confirmed the metal oxygen bond formation. SEM micrographs revealed the spherical morphology and stoichiometric amounts from EDX analysis showed good correspondence to theoretical amounts added.

Electrochemical analysis was carried out for pure alumina and synthesized alumina supported iron oxide nano crystalline materials by using cyclic voltammetry (CV) and conductive response for all the materials was examined by using electrochemical impedance spectroscopy (EIS). Increasing the loading of iron oxide from 1% to 4% resulted in an observed increase in the active surface area, and notably, the 4%Fe₂O₃@Al₂O₃ displayed favorable redox properties with the highest active surface area of 0.06 cm².

The water oxidation reaction in alkaline media was also investigated for all the synthesized materials. All materials showed electroactivity towards OER in KOH and methanol added KOH. The 4-5 order upsurge of peak current densities upon the addition of methanol in KOH was observed, rendering that methanol could be utilized as a facilitating agent for augmenting the OER activity in an alkaline environment. In reference to performance towards OER, various EC performance parameters were addressed to compare the OER activities of the envisioned platform. AlFe-4 (4%Fe₂O₃@Al₂O₃) displayed better activity as compared to other compositions with the lowest onset potential (1.61 V), lowest overpotential (0.54 V), and highest current density of 74.28 mA cm⁻² at 100 mVs⁻¹.

The process exhibited diffusion control, and the 4%Fe₂O₃@Al₂O₃ composition displayed the maximum diffusion coefficient value of 11.4×10^{-8} cm² s⁻¹. The 4%Fe₂O₃@Al₂O₃ also showed the highest heterogeneous rate constant value, 7.0×10^{-4} cms⁻¹. The comparison of diffusion coefficient and heterogeneous rate constant values

shows the irreversible trend in water oxidation for all the synthesized electrocatalytic materials. 4%Fe₂O₃@Al₂O₃ composition posed better electrocatalytic performance with the highest peak current, lowest onset potential, and overpotential values as compared to other compositions with favorable kinetic parameters. Based on EC results, Fe₂O₃@Al₂O₃ can be proposed as potential catalyst for electrochemical water splitting.

References

1. Low, J., Yu, J., Jaroniec, M., Wageh, S. and Al-Ghamdi, A.A., Heterojunction photocatalysts. *Adv. Mater.* 2017. **29**(20): 1601694.
2. Zhang, J., Yan, S. and Qu, H., Recent progress in magnesium hydride modified through catalysis and nanoconfinement. *Int. J. Hydrogen Energy*, 2018. **43**(3): 1545-1565.
3. Whitesides, G.M., Nanoscience, nanotechnology, and chemistry. *Small*, 2005. **1**(2): 172-179.
4. Adlakha-Hutcheon, G., Khaydarov, R., Korenstein, R., Varma, R., Vaseashta, A., Stamm, H. and Abdel-Mottaleb, M., Nanomaterials, nanotechnology: applications, consumer products, and benefits. 2009: 195-207. Springer Netherlands.
5. Joudeh, N. and Linke, D., Nanoparticle classification, physicochemical properties, characterization, and applications: a comprehensive review for biologists. *J. Nanobiotechnol.* 2022. **20**(1): 262.
6. Vollath, D., Nanoparticles-nanocomposites nanomaterials: an introduction for beginners. 2013: John Wiley & Sons.
7. Polshettiwar, V. and Varma, R.S., Green chemistry by nano-catalysis. *Green Chem.* 2010. **12**(5): 743-754.
8. García-Álvarez, J., Advances in Homogeneous Catalysis. *Molecules*, 2020. **2020**: 1493.
9. Li, X., Yang, X., Huang, Y., Zhang, T. and Liu, B., Supported noble-metal single atoms for heterogeneous catalysis. *Adv. Mater.* 2019. **31**(50): 1902031.
10. Liao, P.Q., Shen, J.Q. and Zhang, J.P., Metal-organic frameworks for electrocatalysis. *Coord. Chem. Rev.* 2018. **373**: p. 22-48.
11. Jha, N., Reddy, A.L.M., Shaijumon, M.M., Rajalakshmi, N. and Ramaprabhu, S., Pt-Ru/multi-walled carbon nanotubes as electrocatalysts for direct methanol fuel cell. *Int. J. Hydrog. Energy*, 2008. **33**(1): 427-433.
12. Courty, P. and Marcilly, C., A scientific approach to the preparation of bulk mixed oxide catalysts., in *Studies in Surface Science and Catalysis*, 1983. **16**: 485-519, Elsevier.

13. Stern, K.H., High-temperature properties and decomposition of inorganic salts part 3, nitrates and nitrites. *J. Phys. Chem. Ref. Data*, 1972. **1**(3): 747-772.
14. Du, X., Wang, Y., Su, X. and Li, J., Influences of pH value on the microstructure and phase transformation of aluminum hydroxide. *Powder Technol.* 2009. **192**(1): 40-46.
15. Shen, L., Hu, C., Sakka, Y. and Huang, Q., Study of phase transformation behavior of alumina through precipitation method. *J. Phys. D: Appl. Phys.* 2012. **45**(21): 215302.
16. Pinna, F., Supported metal catalysts preparation. *Catal. Today*, 1998. **41**(1-3): 129-137.
17. Lekhal, A., Glasser, B.J. and Khinast, J.G., Impact of drying on the catalyst profile in supported impregnation catalysts. *Chem. Eng. Sci.* 2001. **56**(15): 4473-4487.
18. Munnik, P., De Jongh, P.E. and De Jong, K.P., Recent developments in the synthesis of supported catalysts. *Chem. Rev.* 2015. **115**(14): 6687-6718.
19. Sharma, S. and Pollet, B.G., Support materials for PEMFC and DMFC electrocatalysts—A review. *J. Power Sources*, 2012. **208**: 96-119.
20. Digne, M., Sautet, P., Raybaud, P., Toulhoat, H. and Artacho, E., Structure and stability of aluminum hydroxides: a theoretical study. *J. Phys. Chem. B*, 2002. **106**(20): 5155-5162.
21. Paglia, G., et al., Boehmite derived γ -alumina system. I. Structural evolution with temperature, with the identification and structural determination of a new transition phase, γ -alumina. *Chem. Mater.* 2004. **16**(2): 220-236.
22. McHale, J.M., Auroux, A., Perrotta, A.J. and Navrotsky, A., Surface energies and thermodynamic phase stability in nanocrystalline aluminas. *Science*, 1997. **277**(5327): 788-791.
23. Samain, L., Jaworski, A., Edén, M., Ladd, D.M., Seo, D.K., Garcia-Garcia, F.J. and Häussermann, U., Structural analysis of highly porous γ -Al₂O₃. *J. of Solid State Chem.* 2014. **217**: 1-8.
24. Levin, I. and Brandon, D., Metastable alumina polymorphs: crystal structures and transition sequences. *J. Am. Ceram. Soc.* 1998. **81**(8): 1995-2012.

25. Fernandez-Garcia, M., Martinez-Arias, A., Hanson, J.C. and Rodriguez, J.A., Nanostructured oxides in chemistry: characterization and properties. *Chem. Rev.* 2004. **104**(9): 4063-4104.
26. Cozzi, L., and Gould, T., World Energy Outlook 2015. *Int. Energy Agency*, 2015.
27. Tee, S.Y., Win, K.Y., Teo, W.S., Koh, L.D., Liu, S., Teng, C.P. and Han, M.Y., Recent progress in energy-driven water splitting. *Adv. Sci.* 2017. **4**(5): 1600337.
28. Gong, M., Wang, D.Y., Chen, C.C., Hwang, B.J. and Dai, H., A mini review on nickel-based electrocatalysts for alkaline hydrogen evolution reaction. *Nano Res.* 2016. **9**: 28-46.
29. Yu, L., Yang, J.F., Guan, B.Y., Lu, Y. and Lou, X.W., Hierarchical hollow nano prisms based on ultrathin Ni-Fe layered double hydroxide nanosheets with enhanced electrocatalytic activity towards oxygen evolution. *Angew. Chem.* 2018. **130**(1): 178-182.
30. Liu, J., et al., 2021 Roadmap: electrocatalysts for green catalytic processes. *J. Phys. Mater.* 2021. **4**(2): 022004.
31. Li, X., Hao, X., Abudula, A. and Guan, G., Nanostructured catalysts for electrochemical water splitting: current state and prospects. *J. Mater. Chem. A.* 2016. **4**(31): 11973-12000.
32. Song, F., Bai, L., Moysiadou, A., Lee, S., Hu, C., Liardet, L. and Hu, X., Transition metal oxides as electrocatalysts for the oxygen evolution reaction in alkaline solutions: an application-inspired renaissance. *J. Am. Chem. Soc.* 2018. **140**(25): 7748-7759.
33. Liang, Q., Brocks, G. and Bieberle-Hütter, A., Oxygen evolution reaction (OER) mechanism under alkaline and acidic conditions. *J. Phys. Energy*, 2021. **3**(2): 026001.
34. Rossmeisl, J., Qu, Z.W., Zhu, H., Kroes, G. J. and Nørskov, J.K., Electrolysis of water on oxide surfaces. *J. Electroanal. Chem.* 2007. **607**(1-2): 83-89.
35. Brouzgou, A., Oxygen evolution reaction. *Methods Electroanal. Adv. Mater. Allied Appl.* 2020: 149-169.
36. Aijaz, A., Masa, J., Rosler, C., Xia, W., Weide, P., Fischer, R.A., Schuhmann, W. and Muhler, M., Metal-organic framework derived carbon nanotube grafted

- cobalt/carbon polyhedra grown on nickel foam: An efficient 3D electrode for full water splitting. *ChemElectroChem*. 2017. 4(1): 188-193.
37. Xue, B.W., Zhang, C.H., Wang, Y.Z., Xie, W.W., Li, N.W. and Yu, L., Recent progress of Ni-Fe layered double hydroxide and beyond towards electrochemical water splitting. *Nanoscale Adv.* 2020. 2(12): 5555-5566.
 38. Wang, J., Cui, W., Liu, Q., Xing, Z., Asiri, A.M. and Sun, X., Recent progress in cobalt-based heterogeneous catalysts for electrochemical water splitting. *Adv. Mater.* 2016. 28(2): 215-230.
 39. Jin, Z., et al., Nanoporous Al-Ni-Co-Ir-Mo high-entropy alloy for record-high water splitting activity in acidic environments. *Small*, 2019. 15(47): 1904180.
 40. Peng, X., Pi, C., Zhang, X., Li, S., Huo, K. and Chu, P.K., Recent progress of transition metal nitrides for efficient electrocatalytic water splitting. *Sustain. Energy Fuels*, 2019. 3(2): 366-381.
 41. Weidman, M.C., Esposito, D.V., Hsu, Y.C. and Chen, J.G., Comparison of electrochemical stability of transition metal carbides (WC, W₂C, Mo₂C) over a wide pH range. *J. Power Sources*, 2012. 202: 11-17.
 42. Wang, D., Song, Y., Zhang, H., Yan, X. and Guo, J., Recent advances in transition metal borides for electrocatalytic oxygen evolution reaction. *J. Electroanal. Chem.* 2020. 861: 113953.
 43. Burke, M.S., Zou, S., Enman, L.J., Kellon, J.E., Gabor, C.A., Pledger, E. and Boettcher, S. W., Revised oxygen evolution reaction activity trends for first-row transition-metal (oxy) hydroxides in alkaline media. *J. Phys. Chem. Lett.* 2015. 6(18): 3737-3742.
 44. Bunaciu, A.A., Udriștioiu, E.G. and Aboul-Enein, H.Y., X-ray diffraction: instrumentation and applications. *Crit. Rev. Anal. Chem.* 2015. 45(4): 289-299.
 45. Hughes, T.J., Plug formation and dissociation of mixed gas hydrates and methane semi-clathrate hydrate stability. 2008.
 46. Lincke, G., A review of thirty years of research on quinacridones. X-ray crystallography and crystal engineering. *Dyes Pigm.* 2000. 44(2): 101-122.

47. Fatimah, S., Ragadhita, R., Al Husaeni, D.F. and Nandiyanto, A.B.D., How to calculate crystallite size from x-ray diffraction (XRD) using Scherrer method. *ASEAN J. Sci. Eng.* 2022. **2**(1): 65-76.
48. Gaffney, J.S., Marley N.A. and Jones D.E., Fourier transform infrared (FTIR) spectroscopy. *Character. Mater.* 2002: 1-33.
49. Patrizi, B., Siciliani de Cumis, M., Viciani, S. and D'Amato, F., Dioxin and related compound detection: Perspectives for optical monitoring. *Int. J. Mol. Sci.* 2019. **20**(11): 2671.
50. McMullan, D., SEM—past, present and future. *J. Microsc.* 1989. **155**(3): 373-392.
51. Siek, M.M., Electrochemical preparation of Ag-and Au-based plasmonic platforms. 2016, Dissertation, Institute of Physical Chemistry Polish Academy of Sciences, Poland.
52. Zhou, W. and Wang, Z.L., Scanning microscopy for nanotechnology: techniques and applications. 2007: Springer science & business media.
53. Yurdakal, S., Garlisi, C., Özcan, L., Bellardita, M. and Palmisano, G., (Photo) catalyst characterization techniques: adsorption isotherms and BET, SEM, FTIR, UV-Vis, photoluminescence, and electrochemical characterizations, in Heterogeneous photocatalysis. *Heterogeneous Photocatal.* 2019: 87-152.
54. Boyes, W., Instrumentation reference book, 4th ed., 2009: Butterworth-Heinemann.
55. Kim, T., Choi, W., Shin, H.C., Choi, J.Y., Kim, J.M., Park, M.S. and Yoon, W.S., Applications of voltammetry in lithium-ion battery research. *J. Electrochem. Sci. Technol.* 2020. **11**(1): 14-25.
56. Wijeratne, K., Conducting Polymer Electrodes for Thermogalvanic Cells. Vol. 1971. 2019, Dissertation, Linköping University Electronic Press, Sweden.
57. Lv, Y., Zhang, X., Zhang, P., Wang, H., Ma, Q. and Tao, X., Comparison between voltammetric detection methods for abalone-flavoring liquid. *Open Life Sci.* 2021. **16**(1): 354-361.
58. Gray, L.G. and Appleman, B.R., EIS: electrochemical impedance spectroscopy. *J. Prot. Coat. Linings*, 2003. **20**(2): 66-74.
59. Scholz, F., Books on fundamental electrochemistry and electroanalytical techniques, in electroanalytical methods. 2010, Springer: 343-345.

60. Choi, W., Shin, H.C., Kim, J.M., Choi, J.Y. and Yoon, W.S., Modeling, and applications of electrochemical impedance spectroscopy (EIS) for lithium-ion batteries. *J. Electrochem. Sci. Technol.* 2020, **11**(1): 1-13.
61. Bard, A.J. and L.R. Faulkner, Fundamentals and applications. Electrochemical methods, 2nd ed., 1980: 45-90.
62. Alkire, R.C., Kolb, D.M., Lipkowski, J. and Ross, P.N., Chemically modified electrodes. *John Wiley & Sons*, 2nd ed., 2009: 45-160.
63. Canales, C., Gidi, L. and Ramirez, G., Electrochemical activity of modified glassy carbon electrodes with covalent bonds towards molecular oxygen reduction. *Int. J. Electrochem. Sci.* 2015. **10**(2): 1684-1695.
64. Elgrishi, N., Rountree, K.J., McCarthy, B.D., Rountree, E. S., Eisenhart, T. T. and Dempsey, J.L., A practical beginner's guide to cyclic voltammetry. *J. Chem. Educ.* 2018. **95**(2): 197-206.
65. Mujtaba, A., & Janjua, N.K., Electrochemical sensing platform based on CuO@CeO₂ hybrid oxides. *J. Electroanal. Chem.* 2016. **763**: 125-133.
66. Li, G.F., Yang, D. and Abel Chuang, P.Y., Defining Nafion ionomer roles for enhancing alkaline oxygen evolution electrocatalysis. *ACS Catal.* 2018. **8**(12): 11688-11698.
67. Li, G.F., Divinagracia, M., Labata, M.F., Ocon, J.D. and Abel Chuang, P.Y., Electrolyte-dependent oxygen evolution reactions in alkaline media: electrical double layer and interfacial interactions. *ACS Appl. Mater. Interfaces*, 2019. **11**(37): 33748-33758.
68. Monshi, A., Foroughi, M.R. and Monshi, M.R., Modified Scherrer equation to estimate more accurately nano-crystallite size using XRD. *World J. Nano Sci. Eng.* 2012. **2**(3): 154-160.
69. Wang, S., Li, X., Wang, S., Li, Y. and Zhai, Y., Synthesis of γ -alumina via precipitation in ethanol. *Mater. Lett.* 2008. **62**(20): 3552-3554.
70. Jung, S., McCrory, C.C., Ferrer, I.M., Peters, J.C. and Jaramillo, T.F., Benchmarking nanoparticulate metal oxide electrocatalysts for the alkaline water oxidation reaction. *J. Mater. Chem. A*, 2016. **4**(8): 3068-3076.

71. Barsoukov, E. and Macdonald, J.R., Impedance spectroscopy: theory, experiment, and applications. *John Wiley & Sons*, 1st ed., 2018, 27-500.
72. Gu, H.Y., Yu, A.M. and Chen, H.Y., Direct electron transfer and characterization of hemoglobin immobilized on a Au colloid–cysteamine-modified gold electrode. *J. Electroanal. Chem.* 2001. **516**(1-2): 119-126.
73. Sharifi, E., Salimi, A. and Shams, E., Electrocatalytic activity of nickel oxide nanoparticles as mediatorless system for NADH and ethanol sensing at physiological pH solution. *Biosens. Bioelectron.* 2013. **45**: 260-266.
74. Shinde, P.S., Choi, S.H., Kim, Y., Ryu, J. and Jang, J.S., Onset potential behavior in α -Fe₂O₃ photoanodes: the influence of surface and diffusion Sn doping on the surface states. *Phys. Chem. Chem. Phys.* 2016. **18**(4): 2495-2509.
75. Tahir, M., Pan, L., Idrees, F., Zhang, X., Wang, L., Zou, J.J. and Wang, Z.L., Electrocatalytic oxygen evolution reaction for energy conversion and storage: a comprehensive review. *Nano Energy*, 2017. **37**: 136-157.
76. Bard, A. and L. Faulkner, Fundamentals and applications. *Electrochemical Methods*, 2nd ed., 2001: 580-632.
77. Eliaz, N. and Gileadi, E., Physical electrochemistry: fundamentals, techniques, and applications. 2019: John Wiley & Sons, Germany.
78. Butt, T.M., et al., B-site doping in lanthanum create nanomaterials for water electrocatalysis. *J. Electrochem. Soc.* 2020. **167**(2): 026503.
79. Butt, T.M., Ullah, A. and Janjua, N.K.J., Electrokinetic analysis of water oxidation on alumina supported silver oxide nanopowders. *J. Electroanal. Chem.* 2022. **907**: 116053.
80. Alobaid, A., Wang, C. and Adomaitis, R.A., Mechanism and Kinetics of HER and OER on NiFe LDH Films in an Alkaline Electrolyte. *J. Electrochem. Soc.* 2018. **165**(15): J3395-J3404.
81. Soon, J.M. and Loh, K.P., Electrochemical double-layer capacitance of MoS₂ nanowall films. *Electrochem. Solid-State Lett.* 2007. **10**(11): A250.

Appendix I

The optimal composition, AlFe-4 was further applied as a sensing platform for Cd^{2+} ions. Square wave stripping voltammetry (SWSV) was performed to study the heavy metal ions sensing. AlFe-4 catalyst was used to perform stripping voltammetry for the detection of 1 and 10 ppb Cd ions at different deposition time from 30 to 120 seconds in acetate buffer. Hence, 120 s was selected as optimized time for the highest current value of the analyte.

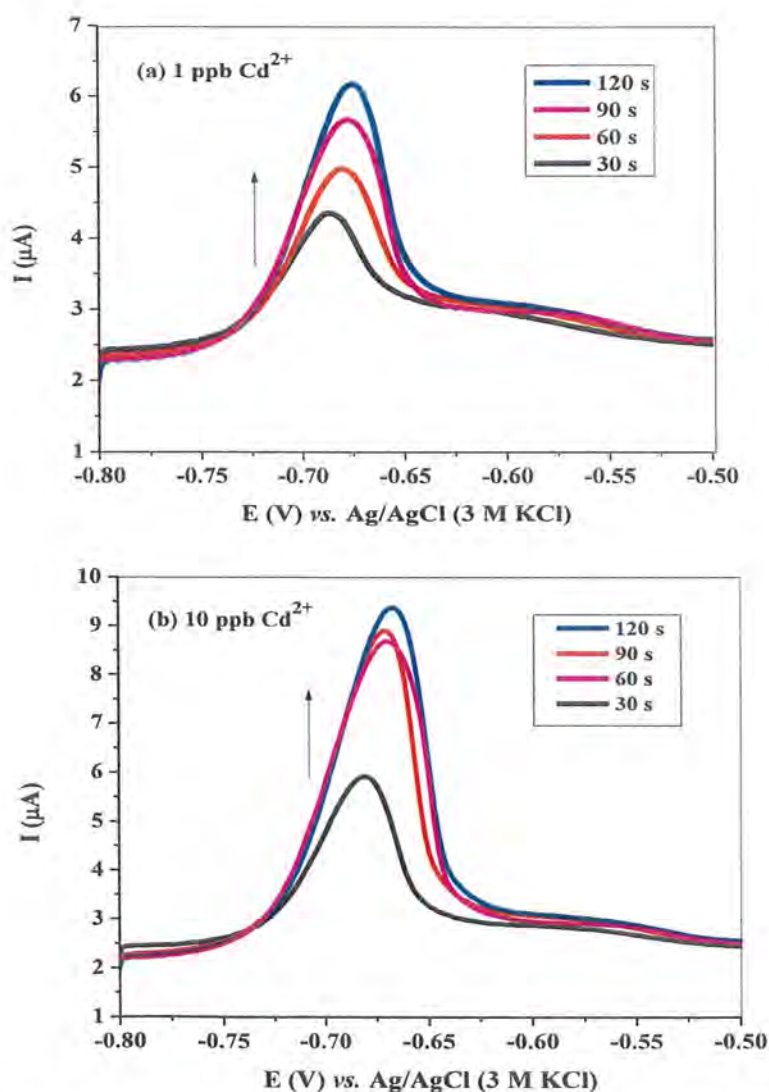


Figure A1. Stripping voltammograms for AlFe-4 in 4.5 pH acetate buffer with change in initial deposition time from 30 to 120 s for (a) 1 ppb Cd^{2+} solution and (b) 10 ppb Cd^{2+} solution.